AN ANALYSIS OF WHISTLER-MODE RADIATION

FROM THE SPACELAB-2 ELECTRON BEAM

by

William Michael Farrell

An Abstract

Of a thesis submitted in partial fulfillment
of the requirements for the Doctor of
Philosophy degree in Physics
in the Graduate College of
The University of Iowa

July 1987

Thesis supervisor: Professor Donald A. Gurnett

ABSTRACT

During the Spacelab-2 mission, the University of Iowa's Plasma

Diagnostics Package (PDP) was released from the space shuttle to

investigate plasma effects in the near-shuttle environment. At times

during this freeflight when the PDP was magnetically connected to the

shuttle, an electron gun in the shuttle cargo bay ejected a nearly

field-aligned 1 keV - 50 mA electron beam. During these beam ejec-

tions, the plasma wave instrument onboard the Plasma Diagnostics

Package detected intense whistler-mode radiation from the beam. This

thesis presents a detailed study of a whistler mode emission detected

during one period when the beam was ejected continuously for about 7

minutes. The electric field polarization of the detected whistler

mode signal is consistent with propagation near the resonance cone.

Calculations indicate that the beam radiated approximately 1.6 mW in

the whistler mode as the beam traversed the 200 meters from the

shuttle to the PDP. The emissivity also decreased by about a factor

of 10 over this same distance. The measured wave powers are 10^7

greater than wave powers expected from incoherent Cerenkov radiation,

verifying that the radiation is generated by a coherent process.

One coherent wave generation mechanisms considered in this study

is the whistler-mode instability in the beam; however, it has been

concluded that this instability cannot sufficiently amplify the

radiation to the measured power levels since the path length for wave growth in the beam is much smaller than the estimated whistler-mode wavelength.

Another wave generation process considered is coherent Cerenkov radiation from electron bunches formed in the beam by an electrostatic beam-plasma instability. A one-dimensional simulation of the SL-2 electron beam verifies the existence of these electron bunches, and the calculated coherent power radiated from this modeled beam is near the power levels measured from the SL-2 electron beam in the whistler mode. Including coherent Cerenkov radiation effects in the calculation of the power increases their values by nearly 90 dB's above incoherent power levels. Consequently, this mechanism can account for the whistler-mode radiation detected by the PDP during its encounter with the 1 keV - 50 mA electron beam.

Abstract approved: _____

Thesis supervisor

_____

Title and department

_____

Date

AN ANALYSIS OF WHISTLER-MODE RADIATION

FROM THE SPACELAB-2 ELECTRON BEAM

by

William Michael Farrell

A thesis submitted in partial fulfillment
of the requirements for the Doctor of
Philosophy degree in Physics
in the Graduate College of
The University of Iowa

July 1987

Thesis supervisor: Professor Donald A. Gurnett

ACKNOWLEDGEMENTS

I would like to thank Dr. Donald A. Gurnett for his ideas, patience and support throughout all phases of this project. I would also like to thank Dr. Christoph K. Goertz, Terry Whelan and Shinobu Machida for their timely ideas concerning the simulation and radiated power calculations. I would also like to thank John Steinberg for the useful discussions. Terry Averkamp deserves thanks for his valuable input on PDP data analysis and John Birkbeck deserves thanks for a fine drafting job. I would also like to thank Kathy Kurth for the time and effort spent typing this thesis.

ABSTRACT

During the Spacelab-2 mission, the University of Iowa's Plasma
Diagnostics Package (PDP) was released from the space shuttle to
investigate plasma effects in the near-shuttle environment. At times
during this freeflight when the PDP was magnetically connected to the
shuttle, an electron gun in the shuttle cargo bay ejected a nearly
field-aligned 1 keV - 50 mA electron beam. During these beam ejec-
tions, the plasma wave instrument onboard the Plasma Diagnostics
Package detected intense whistler-mode radiation from the beam. This
thesis presents a detailed study of a whistler mode emission detected
during one period when the beam was ejected continuously for about 7
minutes. The electric field polarization of the detected whistler
mode signal is consistent with propagation near the resonance cone.
Calculations indicate that the beam radiated approximately 1.6 mW in
the whistler mode as the beam traversed the 200 meters from the
shuttle to the PDP. The emissivity also decreased by about a factor
of 10 over this same distance. The measured wave powers are 10^7
greater than wave powers expected from incoherent Cerenkov radiation,
verifying that the radiation is generated by a coherent process.

One coherent wave generation mechanisms considered in this study
is the whistler-mode instability in the beam; however, it has been
concluded that this instability cannot sufficiently amplify the

radiation to the measured power levels since the path length for wave growth in the beam is much smaller than the estimated whistler-mode wavelength.

Another wave generation process considered is coherent Cerenkov radiation from electron bunches formed in the beam by an electrostatic beam-plasma instability. A one-dimensional simulation of the SL-2 electron beam verifies the existence of these electron bunches, and the calculated coherent power radiated from this modeled beam is near the power levels measured from the SL-2 electron beam in the whistler mode. Including coherent Cerenkov radiation effects in the calculation of the power increases their values by nearly 90 dB's above incoherent power levels. Consequently, this mechanism can account for the whistler-mode radiation detected by the PDP during its encounter with the 1 keV - 50 mA electron beam.

TABLE OF CONTENTS

LIST OF TABLES

LIST OF FIGURES

CHAPTER I

GENERAL INTRODUCTION

The results of a study of a whistler-mode emission detected from an artificial electron beam during the space shuttle's Spacelab-2 (SL-2) mission are presented in this thesis. The study includes a measurement of the total radiated power from the beam in the whistler-mode and a comparison of this power to the power predicted by various whistler-mode radiation mechanisms.

The Spacelab-2 flight, which was launched on July 29, 1985, included an electron gun called the Fast Pulsed Electron Generator (FPEG) from Stanford University, and a spacecraft called the Plasma Diagnostics Package (PDP) from the University of Iowa. During a 6-hour period on August 1, 1985, the PDP was released from the shuttle to investigate plasma effects in the vicinity of the shuttle. During the PDP free flight, the shuttle was maneuvered so that the PDP passed near magnetic field lines connected to the shuttle. Four such magnetic conjunctions were achieved. During one of these magnetic conjunctions a 1 keV − 50 mA electron beam was continuously ejected from the shuttle so that radiation effects could be monitored as the PDP passed near the magnetic field line carrying the beam. Figure 1 shows a frequency vs. time spectrogram from the PDP plasma wave instrument during this electron beam event. The funnel-shaped signal extending from the electron cyclotron frequency, f_c, down to approximately 30

kHz is whistler-mode radiation from the electron beam. This whistler-mode radiation was first described by Gurnett et al. [1986] and is the subject of this thesis.

The observation of this beam-generated whistler-mode signal is not unusual; in fact, whistler-mode radiation is frequently detected from both artificial and natural electron beams in the ionosphere. The following briefly describes some of these electron beams and the corresponding radiation detected.

The first artificial electron beam experiment was performed in the ionosphere in 1969. An electron accelerator was flown on an Aerobee 350 rocket and injected a 9.5 keV/490 mA pulsed electron beam into the ionospheric medium [Hess et al., 1971]. Although ground-based radio receivers did not detect any beam-generating emissions, the beam did propagate ~ 200 km into the lower ionosphere where it was observed optically. This experiment demonstrated that artificial electron beams could propagate great distances without being destroyed by beam-generated instabilities.

During the seventies and eighties, an investigative group at the University of Minnesota performed a number of electron beam experiments in the ionosphere with two stated purposes: first, to study the electron beam, including its emitted radiation and its effect on the beam-ejecting spacecraft; and second, to use the beam as a diagnostic tool to further understand processes occurring in the magnetosphere and ionosphere [Winckler, 1980]. Specifically, their electron Echo experiments were designed to inject an electron beam on closed field lines

into the conjugate hemisphere and analyze the returning electrons (electron "echoes") to identify any physical processes involved. To study the plasma and radio waves emitted from these beams, a radio receiver, typically located in the rocket nose cone, was separated from the main payload. During beam injections these receivers detected waves in the whistler mode, at the upper hybrid/plasma frequencies and at electron cyclotron harmonics (ECH) [Cartwright and Kellogg, 1974; Kellogg et al., 1976; Monson et al., 1976; Winckler, 1980]. Recently, the scientific objectives of the latest Echo experiment, Echo 7, were presented and again include an extensive electron beam investigation [Winckler et al., 1986].

Observations of beam-generated emissions were also made during the joint Franco-Soviet Artificial Radiation and Aurora between Kerguelen and the Soviet Union (ARAKS) experiments in 1975 (Lavergnat et al., 1980). Like the Echo experiments, a diagnostics package was carried in the nose cone of the rocket and separated from the main payload. During electron beam injections, radio receivers flown on this package detected waves in the whistler mode, near the local plasma frequency, and near the fourth harmonic of the electron cyclotron frequency (an ECH emission) [Lavergnat et al., 1980; Dechambre et al., 1980a, Dechambre et al., 1980b].

Electron beams have also been used to probe structures occurring in the auroral region. Such an example is the "E∥B" experiment that was launched into an auroral arc. During the flight, an electron beam was injected along geomagnetic field lines to locate the regions of

parallel electric field that generated the arc. It was believed that part of the injected electron beam would reflect from these regions; however, few reliable signatures of the returning electrons were detected during the experiment [Wilhelm et al., 1980]. A second flight under the same investigation, the NVB-06 flight, was launched in December of 1979. During pulsed electron beam injections, Kellogg et al. [1986] again reported observing waves in the whistler mode, at the upper hybrid frequency, and at the fundamental and first harmonic of the electron cyclotron frequency. The relative intensity and frequency spectra of the waves were also observed to vary with the beam energy and current, and may have been associated with beam plasma discharge (BPD) effects (see Bernstein et al. [1979]).

A unique facility used for beam-plasma research is the Johnson Space Center (JSC) plasma chamber. This cylindrical chamber has a height of 27.4 m and a diameter of 16.8 m, and is large enough to allow space-like experiments to be performed in a laboratory environment. Such experiments performed on injected electron beams include measurements of the emitted radiation and a study of BPD effects [Shawhan, 1982]. For a review of the results from these experiments, see Grandel [1982].

Electron beam injection experiments in the ionosphere have also been performed on the space shuttle. Since the electron beams and corresponding diagnostics packages (particularly the PDP) could be maneuvered into favorable positions, wave and particle measurements unobtainable from rocket experiments were made in and around the beam

environment. The first electron beam experiment performed on the shuttle was in March of 1982 as part of the STS-3 mission. On this flight, the PDP was maneuvered using the shuttle's Remote Manipulator Arm (RMS) while the FPEG, located in the shuttle cargo bay, produced an electron beam. During beam injections, strong emissions near the local plasma frequency and possibly in the whistler mode were detected by the PDP radio receivers [Shawhan et al., 1984]. In December of 1983, the shuttle carried the PICPAB (Phenomenon Induced by Charged Particle Beams) and SEPAC (Space Experiments with Particle Accelerators) investigations into the ionosphere as part of the Spacelab-1 mission. During electron beam injections, the PICPAB radio receivers detected emissions in the whistler mode, at the plasma frequency and at the fourth harmonic of the cyclotron frequency [Beghin et al., 1984] while the SEPAC radio receivers detected an intense VLF signal between 0.7 and 10 kHz that varied in intensity depending on the beam pitch angle [Neubert et al., 1986]. As mentioned previously, in July/ August of 1985, the shuttle again carried the PDP and FPEG into the ionosphere as part of the Spacelab-2 mission. The PDP was released to fly around the shuttle and during magnetic conjunction with the shuttle the FPEG was fired. Besides detecting the whistler-mode radiation, emissions near the local plasma frequency and intense electrostatic emissions below 30 kHz were detected by the PDP during beam injections [Gurnett et al., 1986]. During pulsed electron beam events electromagnetic waves at the fundamental and harmonics of the pulsing frequency were also observed [Reeves et al., 1986; Bush et al., 1986].

From the discussion above, it seems evident that whistler-mode radiation is commonly detected from artificial electron beams. This radiation is also produced naturally in the auroral zone in association with the field-aligned electron beams that are responsible for the aurora [Gurnett, 1966] and is usually called auroral hiss. Both upward and downward propagating auroral hiss has been observed [Mosier and Gurnett, 1969]. The downward propagating auroral hiss is associated with downward moving electron beams with characteristic energies of a few hundred eV [Gurnett, 1966; Hartz, 1969; Gurnett and Frank, 1972; Laaspere and Hoffman, 1976]. The upward propagating auroral hiss often has a V-shaped spectrum called a "saucer" [Smith, 1969; Mosier and Gurnett, 1969; James, 1976] or a "funnel" [Gurnett et al., 1983]. Upward propagating auroral hiss has been observed in association with upward moving field-aligned electron beams [Lin et al., 1984]. The characteristic frequency-time shape of the "saucer" or "funnel" is a propagation effect that occurs for whistler-mode waves propagating near the resonance cone.

Although whistler-mode waves and electron beams are closely related, the exact wave-particle interaction generating the waves is unknown. It is hoped that the study of the whistler-mode radiation from the SL-2 electron beam will aid in the understanding of the processes that create these other artificial and natural beam-generated whistler-mode emissions.

The specific outline of this thesis is as follows. In Chapter II measurements of the polarization and power of the whistler-mode

radiation from the SL-2 electron beam are presented. In Chapter III, the measured power is compared and contrasted to the calculated power predicted from possible incoherent and coherent wave generation mechanisms. By the end of Chapter III, it will be evident that coherent Cerenkov radiation from electron bunches in the beam is the only mechanism able to account for the measured power in the whistler mode. Chapters IV and V involve the detailed modeling of the electron bunches responsible for the coherent Cerenkov radiation. Specifically, an expression for the radiated power from an electron beam is derived in Chapter IV and the Appendix. In Chapter V, the results of a computer simulation of the SL-2 electron beam are presented, which includes the modeling of the electron beam distribution. Electron bunches in the simulated beam resulting from a beam-plasma instability are clearly evident. The radiated power from this simulated beam will then be calculated using the derived power expressions and will be compared to the measured power from the SL-2 electron beam in the whistler-mode.

CHAPTER II

POLARIZATION AND POWER OF THE WHISTLER-MODE

RADIATION FROM THE SL-2 ELECTRON BEAM

In this section, measurements of the electric field polarization
and radiated power of the whistler-mode emission from the 1 keV − 50 mA
SL-2 electron beam are presented. As will be shown, both measured
quantities are important in determining the wave generation mechanism
of the whistler-mode emission.

A. Electric Field Polarization

The whistler mode has a polarization that depends on the wave
frequency, f, the wave normal angle, θ, the cyclotron frequency, f_c,
and the plasma frequency, f_p. Using cold plasma theory [Stix, 1962],
the electric-field and index of refraction vectors can be calculated as
a function of these parameters. The variation of the index of refrac-
tion as a function of θ is often presented as an index of refraction
surface $\overline{n}(\theta)$, which defines the locus of points the index of refraction
vectors make as a function of the wave normal angle for constant f, f_p
and f_c. Figure 2 shows a typical index of refraction surface for the
whistler mode. At a limiting wave normal angle, known as the resonance
cone angle, θ_{Res}, the index of refraction goes to infinity. This angle
is defined by $\tan^2\theta_{Res} = -P/S$, where $P = 1 - f_p^2/f^2$ and $S = 1 - f_p^2/(f^2 - f_c^2)$. As the wave normal approaches the resonance cone,

the electric field $\overline{E}$ becomes linearly polarized with $\overline{E}$ parallel to $\overline{n}$. In this limit the electric field is quasi-electrostatic and the group velocity, $\overline{v}_g$, is perpendicular to $\overline{E}$ and $\overline{n}$ (see Figure 2).

In a previous paper [Gurnett et al., 1986], the funnel-shaped frequency versus time pattern of the radiation from the SL-2 electron beam was explained as a frequency dependent propagation effect for whistler-mode emissions propagating near the resonance cone. As the wave frequency increases, the resonance cone angle, θ_{Res}, decreases and the ray path direction, $\overline{v}_g$, becomes increasingly oblique to the magnetic field, approaching 90° as the frequency approaches the electron cyclotron frequency. As the PDP approaches the beam, emissions near the gyrofrequency are detected first, since their ray paths are almost perpendicular to the beam. Lower and lower frequencies are then detected as the distance between the PDP and beam decreases. This frequency dependent wave propagation effect causes the funnel-shaped emission pattern observed in Figure 1 and provides strong evidence that the radiation is propagating near the resonance cone.

In order to provide further confirmation that the radiation from the SL-2 electron beam is propagating near the resonance cone, an additional test was performed. This test compares model electric-field directions in the PDP spin plane to their actual directions as measured by the PDP plasma wave instrument. To perform this test a computer program was developed that calculates the angle, ϕ, between the projection of a model electric field onto the spin plane and a fixed reference direction. The fixed reference direction selected was

the spin plane projection of the spacecraft-sun vector. To compute ϕ, the group velocity was assumed to be directed from a point on the beam toward the PDP with the electric field vector, $\overline{E}$, at an angle θ_{Res} relative to the beam. This field geometry is the expected configuration for an upward propagating whistler-mode wave near the resonance cone. Figure 3 shows the corresponding geometry of $\overline{E}$, $\overline{v}_g$ and $\overline{k}$.

The electric-field directions in the spin plane calculated using the model described above are compared to the measured electric-field directions found from spin modulation maximums in the receiver data. The spin modulation maximums occur when the PDP electric antennas are aligned with the measured electric field in the spin plane, thus allowing a direct determination of this measured electric field direction. Figure 4 shows the results of this comparison at four frequencies: 562, 311, 178, and 100 kHz. This figure shows the phase angle, ϕ, between the projected electric field and the sun vector as a function of time. The dots represent the modeled electric-field directions computed assuming a resonance cone propagation scheme while the X's represent the measured electric-field directions. The close agreement between the computed and measured electric field directions provides strong confirmation that the waves are propagating near the resonance cone and in the beam direction (i.e., $\overline{k}\cdot\overline{v}_b > 0$), as indicated in Figure 3.

B. Emitted Power

In this section the total power radiated from the beam in the whistler mode is estimated. By comparing the radiated power to the

total power in the beam, the efficiency of the wave-beam interaction can be determined and compared with various generation mechanisms.

The power emitted from the beam in the whistler mode is obtained by integrating the Poynting flux over a surface surrounding the beam. An inherent difficulty with this calculation is the determination of the phase and magnitude of the electric and magnetic fields in the Poynting flux expression, $\overline{S} = \overline{E} x \overline{H}$. Since three axis measurements are not available and since phase measurements were not made, the Poynting vector cannot be determined directly. The situation is further complicated by the fact that the emission is propagating near the resonance cone and is quasi-electrostatic. Consequently, the ratio of the electromagnetic to electrostatic components of the wave electric field is a sensitive function of the wave normal angle. Therefore, to compute the wave normal angle it is assumed that the radiation is produced by the Landau resonance, i.e., $\frac{\omega}{k_\parallel} = \frac{c}{n_\parallel} = v_b$. Since the beam velocity is known, this assumption gives a well-defined value for the wave normal direction. The fact that the radiation is propagating in the same direction as the beam ($\overline{k} \cdot \overline{v}_b > 0$) provides a strong indication that the Landau resonance is involved. For example, the s = -1 cyclotron resonance produces radiation propagating in the opposite direction of the beam and is therefore completely ruled out, since the radiation is observed to be propagating in the direction of the beam. Also, as will be discussed later, the Landau resonance gives the best agreement with the measured electric to magnetic field ratios.

To compute the Poynting vector, $\overline{S}$, the electrostatic and electro-magnetic component of the whistler-mode electric field must be deter-mined. Since the PDP did not measure the relative phase between $\overline{E}$ and $\overline{H}$, these important components of $\overline{E}$ cannot be directly calculated. However, by using the assumption that the waves are generated via a Landau resonance, $\overline{n}$ and $\overline{E}$ can be calculated exactly using cold plasma theory. Consider, first, the whistler-mode wave electric field. Since the emission is propagating near the resonance cone, $\overline{E}$ lies almost entirely in the plane defined by $\overline{n}$ and the geomagnetic field (see Figure 3). The electrostatic and electromagnetic components of $\overline{E}$ are then given by $E_0 \cos \Delta\theta$ and $E_0 \sin \Delta\theta$, respectively, where $\Delta\theta$ is the angle between $\overline{E}$ and $\overline{n}$, and E_0 is amplitude of the total electric field. The angle $\Delta\theta$ is determined by the Landau resonance condition and cold plasma theory. The Landau resonance condition specifies the component of n parallel to the geomagnetic field, i.e.,

$$n_\| = n \cos \theta = c/v_b \quad .$$

$$(2-1)$$

where c is the speed of light. For a 1 keV electron beam moving par-allel to the magnetic field $n_\|$ is approximately 15.9. A program was written that solves Equation (1-20) of Stix [1962] for the magnitude and directions of $\overline{n}$ and $\overline{E}$. Using this program, $\overline{n}$ and $\Delta\theta$ at a parti-cular wave frequency can be calculated by constraining values of $\overline{n}(\theta)$ using (2-1). Since $\Delta\theta$ is now determined, the electrostatic and electromagnetic components of $\overline{E}$ can be calculated. The calculated $\Delta\theta$ values are very small, typically ranging from .06° to 1.1° from 31.1

kHz to 562 kHz, indicating that the wave is nearly electrostatic. It is easy to show that the magnitude of the Poynting vector is given by

$$|\overline{S}| = \frac{n \ E_o^2}{2} \left(\frac{\varepsilon_o}{\mu_o}\right)^{1/2} (A^2 + B^2)^{1/2} \quad , \qquad (2\text{-}2)$$

where $A = 1 - \cos^2\Delta\theta$ and $B = \sin \Delta\theta \cos \Delta\theta$. In the derivation of Equation 2 Faraday's Law was used to eliminate the magnetic field in the $\overline{E} \times \overline{H}$ term. Note, also, that as θ approaches the resonance cone angle, $\overline{n}$ and $\overline{E}$ become parallel and $|\overline{S}|$ goes to zero. This behavior near θ_{Res} is similar to an expression derived by Mosier and Gurnett [1971] in their paper addressing Poynting flux measurements of VLF hiss emissions.

Figure 5 shows, pictorially, the PDP trajectory during the 1 keV – 50 mA electron beam event. As can be seen, near the magnetic conjunction, the PDP trajectory was nearly perpendicular to the beam, and, at closest approach, passed within about 3 meters of the beam at a distance of about 200 meters along the field line from the shuttle. To compute the total radiated power, the Poynting flux is integrated over an imaginary surface perpendicular to the beam that includes the PDP trajectory. Assuming that the sampled intensities along this trajectory are constant around an annular ring of the area, $dA = 2\pi RdR$, centered on the beam, the radiated power from the beam segment can be obtained by evaluating the integral $P = \int S_{\parallel} 2\pi RdR$, where $S_{\parallel}$ is the field-aligned component of the Poynting vector and R is the

perpendicular distance from the beam to the PDP. Note that the evaluation of this integral will yield two values for the radiated power: one value from the inbound pass where the limits of integration extend from $R = \infty$ to $R \cong 0$ and one value from the outbound pass where the limits of integration now extend from $R \cong 0$ to $R = -\infty$. Figure 6 shows the average power spectral density from these two passes as a function of wave frequency. The error bars in the figure represent the standard deviations of the power values. Note that the power spectral density, dP/df, is on the order of 10^{-9} W/Hz in the frequency range extending from 30 kHz to 1 MHz. Adding $\frac{dP}{df}$ over the 30 kHz to 1 MHz frequency range, the total emitted power in the 200-meter beam segment from the shuttle to the PDP is found to be $P = 1.6$ mW. If the power were emitted uniformly along the beam, the radiated power per unit length, $dP/d\ell$, would be approximately 1.6 mW/200 m = 8×10^{-6} W/m. Since the total power of the beam was 50 W, the beam converted approximately 1.6 mW/50 W = 3.2×10^{-5} of its power to whistler-mode radiation in the first 200 meters. As a rough indication of the radiation efficiency, if the beam continued to radiate at this level and this radiation was the only beam energy dissipation mechanism, the beam would only propagate about 6000 km before converting all of the beam energy to radiation.

The linear emissivity of the whistler-mode radiation, $dP/dfd\ell$, from different locations along the beam can also be calculated. To calculate the linear emissivity, a knowledge of a signal's exact source location from the beam is required; however, by using the ray

path, the source of the signal at a particular point along the PDP
trajectory can be located. The power radiated from an infinitesimal
beam radiation source, $d\ell$, is $P = \int S_\perp 2\pi R d\ell$, where $S_\perp$ is the perpen-
dicular component of the Poynting vector measured at the perpendicular
distance R from the beam and corresponds to the Poynting flux emitted
from a cylinder of radius, R, and length, $d\ell$, surrounding the beam.
The linear emissivity from this source, $dP/df d\ell$, is then obtained by
using the differential form of the power integral. The calculated
linear emissivity of the whistler-mode waves is shown in Figure 7.
Note that the emissivity drops by a factor of ten from 100 to 200
meters along the beam. This decrease in emissivity indicates that the
efficiency of whistler-mode generation decreases with increasing
distance along the beam and that the generation mechanism is capable
of dynamic changes in tens of meters. If the emissivity continues to
drop at the rate observed between 100 to 200 meters, the radiation
would be undetectable by the PDP at source distances more than about 1
km from the shuttle. This result may explain why DE-1, which was mag-
netically connected to the shuttle during a gun firing on the STS-3
mission, did not see beam-generated whistler-mode radiation in the
vicinity of the streaming electrons [Inan et al., 1984]. From the SL-
2 measurements, it appears that strong whistler-mode emissions are
probably generated only in close proximity to the source of the beam.

As mentioned earlier, the electric and magnetic field measure-
ments also provide direct evidence that the whistler-mode waves were
generated via a Landau resonance process. This evidence comes from a

comparison of computed and measured cB/E ratios. Assuming a specific resonance condition and using the solution of Equation (1-20) of Stix [1962], a unique value for $\bar{n}$ and $\Delta\theta$ can be computed. Faraday's law can then be used to obtain the relationship

$$\bar{n} \times \bar{E} = c\bar{B} \tag{2-3}$$

where $\bar{E}$ is the electric component and $\bar{B}$ is the magnetic component of the whistler-mode waves. For the assumed field geometry, Equation 3 can be rewritten as

$$n \, E_0 \sin \Delta\theta = cB_0 \quad ,$$

or

$$\frac{cB_0}{E_0} = n \sin \Delta\theta \quad . \tag{2-4}$$

Using Equation (2-4), $n \sin \Delta\theta$ is computed for various resonance conditions and compared with the measured cB/E ratio. The spectrum analyzer used with the PDP search coil can only provide measurements up to 178 kHz; therefore, the magnetic to electric field ratio can only be obtained in the 56 kHz, 100 kHz, and 178 kHz frequency channels. Also, the measured values of B at high frequencies using the search coil are highly uncertain, due to inaccuracies in the calibration of the instrument. The preflight calibration was performed by placing a calibration

coil in the search coil and surrounding the system in a μ-metal can. A problem arises at high frequencies (>10 kHz), where frequency dependent capacitances and inductances affect the current and the expected value of $\overline{B}$ from the calibration coils. Unfortunately, post-flight calibrations under more ideal condition (specifically, without the μ-metal can) have failed to reproduce the preflight calibrations. This suggests that the high frequency gain of the search coil may have shifted during the flight. Our current best estimates are that B (and cB/E) are accurate only to within a factor of 2 - 4 at high frequencies. The range of measured cB/E values lies between 1.3 and 15.3. Assuming a Landau resonance, n sin Δθ is computed to be .54, .52, and .54 for 56 kHz, 100 kHz, and 178 kHz, respectively. Note that these values lie just outside the range of measured cB/E values, and fall in the range when considering the factor of 2 - 4 uncertainty in the calibrations. For an s = +1 cyclotron resonance, however, n sin Δθ is computed to be between .05 to .08 for 56 kHz, 100 kHz, and 178 kHz. These values are about a factor of 20 smaller than the lowest measured cB/E value. Similar computed values are obtained for the s = -1 cyclotron resonance. These comparisons show that the measured cB/E ratio is closest to those expected for a Landau resonance.

CHAPTER III

POSSIBLE WHISTLER-MODE WAVE GENERATION MECHANISMS

From the power measurements alone it is not clear whether the beam-generated whistler-mode radiation detected by the PDP during the SL-2 mission results from a coherent or incoherent generation process. A coherent mechanism involves large numbers of particles acting together to generate the emitted waves. The total power from a coherent source goes as N^2, where N is the number of particles in coherence. Common coherent sources are plasma instabilities, lasers and radio antennas. Incoherent mechanisms involve particles that are radiating independently. The power from the individual radiators must be added to get the total power emitted; thus the total power is proportional to N, the number of radiators. A common incoherent source is an incandescent light bulb. In this chapter possible incoherent and coherent mechanisms for generating whistler-mode radiation are described.

A. Incoherent Generation Mechanisms

One possible incoherent mechanism involves incoherent Cerenkov radiation from beam electrons. Cerenkov radiation is generated by charged particles moving with speeds greater than the phase speed of the wave in the medium. The whistler-mode waves from the SL-2 electron beam are propagating near the resonance cone with large indices of refraction, typically $n \sim 30$ to 500. The phase speed of the wave is therefore much

less than the speed of a 1 keV electron. Since the beam electrons are moving faster than the phase speed of the whistler mode, Cerenkov radiation should be produced.

The measured whistler-mode power from the beam is next compared to the calculated power from Cerenkov radiation, assuming that the beam electrons are incoherent radiators. This calculation is similar to those performed by Jorgenson [1968] and Taylor and Shawhan [1973], who both calculated the power from this process and compared it to the radiated powers from VLF hiss. Mansfield [1967] derived an equation that gives the power spectral density radiated from a single electron moving through an ambient ionized gas with a speed greater than the wave phase speed. For an incoherent mechanism, the total power radiated from the beam is the power radiated from each electron $(\frac{dP}{df})_e$, added up over all the electrons in a given beam volume, N_v: $(\frac{dP}{df})_{total} = N_v(\frac{dP}{df})_e$. Using Mansfield's formula, the radiated power from each beam electron can be calculated and is shown in Figure 8. In obtaining this result, it is assumed that the radiation is produced via a Landau resonance. It is also assumed, for this calculation, that the pitch angle of the electrons is 10°. The actual pitch angles varied from 0° to 20°; however, the results are relatively insensitive to pitch angles in this range. From Figure 8 it can be seen that the most intense radiation occurs between the electron cyclotron frequency and the lower hybrid frequency, f_{LHR}. Outside this range the power drops by a factor of 10^4. Note that this frequency range corresponds rather well to the frequency range of the radiation observed by the

PDP. Multiplying the power from each electron by the number of electrons in the first 200 meter segment of the beam (3×10^{12} particles) yields $(\frac{dP}{df})_{total} \sim 10^{-16}$ W/Hz in the frequency range from f_c to f_{LHR}. These power spectral densities are much lower than the measured power spectral densities, by about a factor of 10^7 (compare with Figure 6, where $dP/df \sim 10^{-9}$ W/Hz). Therefore, an incoherent process cannot account for the measured wave powers. Some coherent wave process must be involved. In Taylor and Shawhan's [1973] analyses of the generation of VLF hiss emissions by auroral electron beams, the calculated powers for the incoherent Cerenkov process were found to be a factor of 10^2 – 10^3 lower than those measured, again indicating a coherent process.

B. Coherent Generation Mechanisms

As concluded in the previous section, some coherent process must be involved in the whistler-mode wave generation from the SL-2 electron beam. Coherent processes can be divided into two classes: direct and indirect. Direct mechanisms involve the direct conversion of energy from an unstable particle distribution to electromagnetic radiation; whereas indirect mechanisms involve the intermediate generation of one or more electrostatic modes which are coupled to the escaping electromagnetic radiation. This section will discuss possible direct and indirect mechanisms that may explain the whistler-mode radiation.

Since an unstable electron distribution is present in the beam the escaping electromagnetic radiation may result from direct conversion of the beam energy to electromagnetic radiation. Such a mechanism

has been proposed by Maggs [1976] for the generation of auroral hiss. In his model, incoherent Cerenkov radiation produced by an auroral electron beam is directly amplified via a whistler-mode plasma instability within the beam. It seems reasonable that this wave generation mechanism could be applied to the whistler-mode waves emitted from the SL-2 electron beam; however, a problem arises in doing so. Unlike auroral beams, the path length for wave growth in the SL-2 beam is very short, only two to three electron cyclotron radii (6 to 9 meters). Using the Landau resonance condition and the fact that the emission is propagating near the resonance cone, the wavelength of the whistler-mode radiation is given by

$$\lambda \equiv \frac{V_b}{f} \cos \theta_{Res} \quad , \tag{3-1}$$

which, for the nominal parameters has a value of about 20 meters. This wavelength is greater than the path length, which completely invalidates any mechanism involving exponential growth. Even if that were not the case, for typical whistler-mode group velocities of 10^7 m/sec, the amount of time the wave spends in the beam is so short, only about 10^{-6} sec, that unreasonably high growth rates ($\gamma > \omega_c \equiv 10^6$ sec^{-1}) would be required to generate the radiation. No whistler-mode instability is known that can produce such large growth rates from realistic electron distribution functions. These same conclusions were also reached by Jones and Kellogg [1973] in their paper

addressing the growth rates of whistler-mode radiation from artificially-created electron beams.

Mechanisms involving the intermediate generation of electrostatic waves in the beam are now considered. Any density perturbation or bunch created by an electrostatic wave in the beam is capable of emitting coherent Cerenkov radiation. The radiated power from a bunch will have a frequency spectrum similar to that of a single radiating electron; however, the wave power will be much greater since the emitted power goes as N^2, where N is the number of electrons in a bunch. Coherent Cerenkov radiation from a bunched beam has been considered previously by Bell [1968].

Beam-plasma instabilities are known to be capable of creating intense electrostatic waves and density perturbations in the beam. An estimate of the number of coherently bunched electrons required to account for the observed whistler-mode radiation is presented. A first-order expression for the total power emitted from the electron bunches in the beam is $(\frac{dP}{df})_{TOT} = (\frac{dP}{df})_e (\Delta N)^2 \alpha$, where $(\frac{dP}{df})_e$ is the power radiated by each electron, ΔN is the typical number of electrons in a bunch, and α is the number of bunches in the 200-meter segment of the beam. Consequently,

$$\Delta N = \left(\frac{(\frac{dP}{df})_{TOT}}{(\frac{dP}{df})_e \alpha}\right)^{1/2} \quad . \tag{3-2}$$

Beam-plasma instabilities are known to create an electrostatic wave near the local electron plasma frequency (3 MHz). Such an emission is, in fact, observed near 3 MHz [see Gurnett et al., 1986]. The corresponding wavelength of this emission is $V_b/f_p \approx 7$ meters, which is assumed to be the approximate length of each bunch. This wavelength can then be used to calculate α, the number of bunches in the first 200 meters of the beam. This number is $\alpha \approx 29$. The radiated power from the 200-meter beam segment, $(\frac{dP}{df})_{total}$, is about 10^{-9} W/Hz. From Mansfield, $(\frac{dP}{df})_e$ is about 10^{-29} W/Hz. Using (3-2), it is calculated that each bunch must contain about $\Delta N = 2 \times 10^9$ electrons in order to account for the observed radiated power.

An estimate can now be made of the required electric field strength of the electrostatic wave in the beam that forms the bunches. Assuming that the beam diameter is about 2 cyclotron radii, the electron number density in the bunch can be estimated using the formula:

$$\Delta n = \frac{\Delta N}{\pi r_c^2 \Delta L} \tag{3-3}$$

where ΔL is the bunch length and r_c is the cyclotron radius (2 to 3 meters). The required number density is found to be about $\Delta n = 1 \times 10^7$ electrons/m^3. Again assuming a beam diameter of 2 r_c, the average beam density is $n_0 = 1 \times 10^9$ electron/m^3. Note that the fractional density perturbation in the beam $\Delta n/n_0$ is only about 0.01. Consequently, a relatively small density perturbation can account for the

measured whistler-mode power. Poisson's equation can be used to determine the magnitude of the self-consistent electric field needed to generate this density perturbation

$$\frac{\Delta E}{\Delta L} = \frac{e \Delta n}{\varepsilon_o} \qquad .$$

(3-4)

From Equation (3-4), an electric field on the order of 1-2 V/m is needed to create the required coherence in the beam electrons.

Although the PDP did not fly directly through the beam during free flight, when the PDP was on the Remote Manipulator Arm, it did provide electric field measurements in the beam. During these times, an intense field-aligned electric-field signal near f_{pe} was measured with amplitudes greater than 0.3 V/m, sufficiently large to saturate the receiver. This value is within a factor of 10 of the required amplitudes needed for radiative coherence of the beam electrons. The good agreement between the calculated and measured electrostatic field strengths strongly suggests that electron bunches generated by a beam-plasma instability can account for the observed whistler-mode power.

In the analysis above, it is assumed that the electron beam has fully expanded to a diameter of $2 r_c$ after being injected. This assumption, however, may not actually be valid near the generator since the beam is still expanding after being ejected from the small generator oriface. As will be shown in Chapter V, this expansion can effect beam structure and should be considered in a detailed power calculation.

In the rest of this thesis, a detailed model of the coherent Cerenkov radiation mechanism described above is presented. A computer simulation of the beam is performed, and the radiated power from this beam is calculated and compared to the measured power from the SL-2 beam in the whistler mode.

CHAPTER IV

EMITTED POWER VIA CERENKOV RADIATION PROCESSES

In this chapter an expression will be derived for the power emitted from an electron beam in a plasma by the Cerenkov radiation process. This expression can be used with known electron beam distributions to compute the radiated power from a beam, and can be applied to the SL-2 electron beam to determine its radiated power.

The derivation is similar to that of Mansfield's [1967], who derived an expression for the radiated power from a single test particle in a plasma medium. His approach was to use the Fourier transforms of the source current and electric field to obtain the radiated power; a method that differed from Liemohn [1965], who derived a similar power expression using the solution of the Hamiltonian of the test particle's radiation field. Mansfield [1967] claimed that there was 'excellent quantitative and qualitative agreement' between his expression and Liemohn's.

Either of these expressions for single particle radiation can be used to calculate the incoherently-radiated power from an electron beam. In performing this calculation it is assumed that each electron in the beam radiates independently from all others. The radiated power from each individual electron in a given volume of the beam is then added to obtain the total radiated power.

In the previous section, a calculation of the incoherently-radiated power from the SL-2 electron beam was performed. It was found that this radiation mechanism could not account for the measured whistler-mode wave power, and concluded that coherent effects among the beam electrons must be included in the calculation.

Harker and Banks [1983] derived an expression for the power radiated from a pulsed electron beam in a plasma which included the coherent effects between the radiating electrons in the beam. They, like Mansfield, used the Fourier transforms of the pulsed current source and electric field to obtain the radiated power. In their derivation, it was assumed that all beam electrons travelled with the same velocity, $\bar{v}$, in pulses of length, ℓ, with a distance, d, separating each pulse. Compared to the incoherently-radiated power from a beam, the inclusion of coherent effects between radiating beam-electrons in a pulse leads to much higher radiated powers; however, the derived expression for radiated power did not include effects from bunches that occur due to instabilities in the beam.

In this section, a general expression will be derived for the radiated power from an electron beam that includes the coherent radiation from particle bunches. The derived expression allows one to calculate the radiated power from N field-aligned particles with arbitrary velocity and position. If a distribution of beam particles is known, the velocity and position of these particles can be used to compute the radiated power.

A. Derivations

There will be two expressions derived in this section: first, the power radiated from a single test particle in a plasma medium will be obtained. Except for a simplification, this derivation will follow the identical steps as Mansfield [1967]. Second, this derivation will be generalized to include the radiated power from N particles of arbitrary velocity and position.

In deriving these expressions, it is assumed that all particles are moving parallel to a static magnetic field in a plasma. This choice of particle trajectory will simplify the integrations involved in the derivations. It will be shown that these field-aligned particle trajectories only allow the $s = 0$ Landau resonance interaction between beam particles and waves. This is not a problem, however, since it is believed that the detected whistler-mode signal from the SL-2 electron beam was generated by the Landau interaction. It should be noted that the SL-2 electron beam was not actually field aligned, but varied in pitch angle from $0°$ to $20°$; however, this variation causes only a 6% change in the beam electron's parallel velocity and, as mentioned previously, is not enough variation to significantly alter the radiated power from a 1 keV beam electron. Cyclotron motion of the electrons can, however, alter the radiative coherence of the beam. As will be shown, coherent effects between beam electrons is a function of their relative position. If a beam has a relatively large pitch angle, the beam electrons will deviate from their field-aligned trajectories which alter their relative position and

coherence; however, the SL-2 beam had, at most, a pitch angle of 20°
and during most of the encounter was nearly field aligned. Conse-
quently, the calculated power assuming a field-aligned beam trajectory
should not be significantly different from that of the real SL-2 beam
with small variations in pitch angle.

Some further assumptions will be made in deriving the two power
expressions in this section. These assumptions are identical to those
made by Mansfield [1967] and they are:

(1) That the plasma medium is represented by a homogeneous,
cold, collisionless plasma in a static magnetic field, $\overline{B}_o$.

(2) That the presence of the test particle(s) may be neglected
in the description of the medium.

(3) That the radiated waves from the test particle(s) do not
significantly alter the medium and have magnetic fields much weaker
than $\overline{B}_o$.

(4) That the magnetic permability is equal to the free space
value.

1. Radiated Power From a Single Test Charge In A Plasma Medium

An expression is now be derived for the radiated power from a
single test charge in a plasma medium. The steps taken in this
derivation are identical to Mansfield's [1967], except for the
simplification of making the particle trajectories field aligned.

The first step is to write Ampere's and Faraday's Laws for the
Fourier transforms of $\overline{E}(\overline{r},t)$ and $\overline{H}(\overline{r},t)$:

$$\overline{k} \times \overline{H}(\overline{k},\omega) = -\omega \, \varepsilon_o \overset{\leftrightarrow}{K} \cdot \overline{E}(\overline{k},\omega) + i \, \overline{J}_q(\overline{k},\omega) \qquad (4\text{-}1)$$

$$\overline{k} \times \overline{E}(\overline{k},\omega) = \omega \, \mu \, \overline{H}(\overline{k},\omega) \qquad (4\text{-}2)$$

where $\overline{J}_q(\overline{k},\omega)$ is the Fourier transform of the external source current and $\overset{\leftrightarrow}{K}$ is the dielectric tensor for the plasma medium. Substituting $\overline{H}(\overline{k},\omega)$ from (4-2) into (4-1) yields the homogeneous equation:

$$\overline{n} \times \overline{n} \times \overline{E}(\overline{k},\omega) + \overset{\leftrightarrow}{K} \cdot \overline{E}(\overline{k},\omega) = \frac{i \, \overline{J}_q(\overline{k},\omega)}{\omega \, \varepsilon_o} \qquad (4\text{-}3)$$

where $\overline{n} = \dfrac{\overline{k}c}{\omega}$ is the index of refraction. This equation can be reexpressed as

$$\overset{\leftrightarrow}{T} \cdot \overline{E}(\overline{k},\omega) = \frac{i \, \overline{J}_q(\overline{k},\omega)}{\omega \, \varepsilon_o} \qquad . \qquad (4\text{-}4)$$

A static magnetic field, $\overline{B}_o$, is present in the plasma medium and is assumed to lie along the $\hat{z}$-axis. Radiation from a field-aligned test particle will be azimuthally symmetric; however, for simplicity, it is assumed that $\hat{k}$ is entirely in the y-z plane at an angle θ relative to the $\hat{z}$-axis. This coordinate system can be rotated to analyze radiation from any specific azimuth angle, thus these assumptions can be made without any loss of generality. With these assumptions, $\overset{\leftrightarrow}{T}$ can be expressed as:

$$\ddot{T} = \begin{bmatrix} \bar{\varepsilon}_1 - n^2 & i\,\varepsilon_2 & 0 \\ -i\,\varepsilon_2 & \varepsilon_1 - n^2\cos^2\theta & n^2\sin\theta\cos\theta \\ 0 & n^2\sin\theta\cos\theta & \varepsilon_3 - n^2\sin^2\theta \end{bmatrix} \qquad (4\text{-}5)$$

where

$$\varepsilon_1 = 1 + \frac{f_{pe}^2}{f_{ce}^2 - f^2} + \frac{1836\,f_{pe}^2}{f_{ce}^2 - (1836f)^2} \quad,$$

$$\varepsilon_2 = \frac{f_{pe}^2\,f_{ce}}{f(f^2 - f_{ce}^2)} + \frac{f_{pe}^2\,f_{ce}}{f[f_{ce}^2 - (1836f)^2]} \quad,$$

$$\varepsilon_3 = 1 - \frac{f_{pe}^2}{f^2} - \frac{f_{pe}^2}{1836f^2} \quad;$$

and f, f_{ce} and f_{pe} are the wave frequency, local cyclotron frequency and local plasma frequency, respectively.

The electric field, $\bar{E}(\bar{r},t)$, is obtained by taking the inverse Fourier transform of $\bar{E}(\bar{k},\omega)$:

$$\bar{E}(\bar{r},t) = \frac{1}{\varepsilon_o} \iint \ddot{T}^{-1} \cdot \bar{J}_q(\bar{k},\omega) e^{i(\omega t - \bar{k}\cdot\bar{r})} d\bar{k}\,\frac{d\omega}{\omega} \quad. \qquad (4\text{-}6)$$

For a single test particle in the medium, the source current is expressed as:

$$\overline{J}_q(\overline{r},t) = q\,\overline{V}_q\,\delta(\overline{r} - \overline{r}_q(t)) \tag{4-7}$$

where for field-aligned trajectories, $\overline{V}_q$ is

$$\overline{V}_q = V_o\hat{z} \tag{4-8}$$

and

$$\overline{r}_q = (r_o + V_o t)\hat{z} \qquad . \tag{4-9}$$

The variable r_o is defined as the particle's initial position. The Fourier transform of the source current is:

$$\overline{J}_q(\overline{k},\omega) = \frac{1}{(2\pi)^4}\iint \overline{J}_q(\overline{r},t)e^{i(\overline{k}\cdot\overline{r}-\omega t)}d\overline{r}dt = \frac{\hat{z}qV_o}{(2\pi)^4}\int e^{i(\overline{k}\cdot\overline{r}_q-\omega t)}dt \qquad . \tag{4-10}$$

As mentioned previously, $\hat{k}$ is assumed to lie in the y-z plane, at an angle θ relative to the $\hat{z}$-axis, which allows $\overline{k}$ to be expressed as:

$$\overline{k} = \hat{y}\,k\,\sin\theta + \hat{z}\,k\,\cos\theta \tag{4-11}$$

and

$$\overline{k}\cdot\overline{r}_q = \frac{n\omega\,\cos\theta}{c}\,r_o + n\omega\,\cos\theta\,\beta t \tag{4-12}$$

where $\beta = \dfrac{V_o}{c}$ and $\dfrac{n\omega}{c}$ has been substituted for k. The transform of the source current is then:

$$\overline{J}_q(\overline{k},\omega) = \frac{\hat{z}\, q\, V_o}{(2\pi)^4}\, e^{\frac{in\omega}{c}\cos\theta\, r_o} \int_{-\infty}^{\infty} e^{i(n\omega\cos\theta\,\beta-\omega)t} dt$$

$$(4\text{-}13)$$

$$= \frac{\hat{z}\, q\, V_o}{(2\pi)^3}\, e^{\frac{in\omega}{c}\cos\theta\, r_o}\, \delta(n\omega\cos\theta\,\beta-\omega) \quad .$$

where $\int_{-\infty}^{\infty} e^{i(n\omega\cos\theta\,\beta-\omega)t} dt = 2\pi\delta(n\omega\cos\theta\,\beta-\omega)$ is used to obtain (4-13). Substituting (4-13) into Equation (4-6) yields:

$$\overline{E}(\overline{r},t) = \frac{qiV_o}{(2\pi)^3\epsilon_o} \iint (\ddot{\overline{T}}^{-1}\cdot\hat{z})\, e^{\frac{in\omega\cos\theta}{c}\, r_o}\, \delta(n\omega\cos\theta\,\beta-\omega)$$

$$(4\text{-}14)$$

$$e^{i(\omega t - \overline{k}\cdot\overline{r})}\, d\overline{k}\, \frac{d\omega}{\omega}$$

for the electric field.

The radiated power from this test particle is

$$P(t) = q\, \overline{E}(\overline{r}_q,t)\cdot\overline{V}_q(t)$$

$$(4\text{-}15)$$

$$= \frac{q^2 iV_o^2}{(2\pi)^3\epsilon_o} \iint (\hat{z}\cdot\ddot{\overline{T}}^{-1}\cdot\hat{z}) e^{\frac{in\omega}{c}\cos\theta\, r_o}\, e^{i(\omega t - \overline{k}\cdot\overline{r}_q)}\, \delta(n\omega\cos\theta\,\beta-\omega)\partial\overline{k}\, \frac{d\omega}{\omega}.$$

Substituting (4-12) for $\overline{k} \cdot \overline{r}_q$ in the exponential term of (4-15) yields:

$$P(t) = \frac{q^2 i v_o^2}{(2\pi)^3 \varepsilon_o} \iint (\hat{z} \cdot \ddot{\overline{T}}^{-1} \cdot \hat{z}) \delta(n\omega \cos \theta \beta - \omega) e^{i(\omega - n\omega \cos \theta \beta)t} d\overline{k} \frac{d\omega}{\omega} .$$

(4-16)

Note that the dependence of the power on r_o, the initial position of the particle, cancels out of the expression. The element $d\overline{k}$ can be reexpressed as

$$d\overline{k} = n^2 \frac{\omega^3}{c^3} dn \sin \theta \, d\theta \, d\phi \quad .$$

Since there is no ϕ dependence in (4-16), the integration over ϕ yields a 2π. The integration over θ is more complicated since $\cos \theta$ is in both the delta function and exponential. An integral of the form

$$I = \int f(x) \, \delta(Ax+B)dx = \frac{f(x_o)}{|A|}$$

now has to be evaluated. For (2-16), $A = |n\omega\beta|$, $B = \omega$, and $x_o = \frac{1}{n\beta}$. Note, in the integration, that a nonzero value is obtained only if

$$\cos \theta_o = \frac{1}{n\beta}$$

(4-17)

is satisfied. This is the Landau resonance condition. The expression
for radiated power now becomes:

$$P(t) = \frac{-q^2 i V_o^2}{(2\pi)^2 \varepsilon_o c^3 \beta} \iint (\hat{z} \cdot \overset{\leftrightarrow}{T}^{-1} \cdot \hat{z}) |n| |\omega| dn d\omega \quad .$$
(4-18)

From Mansfield [1967], it is found that

$$(\hat{z} \cdot \overset{\leftrightarrow}{T}^{-1} \cdot \hat{z}) = \frac{\varepsilon_1^2 - \varepsilon_2^2 - \varepsilon_1 n^2 + (n^4 - \varepsilon_1 n^2)\cos^2\theta_o}{\varepsilon_1 (n^2 - n_1^2)(n^2 - n_2^2)}$$
(4-19)

where θ_o is the angle that satisfies the Landau resonance condition and
$n_{1,2}^2 = [-B \pm (B^2 - 4C\varepsilon_1)^{1/2}]/2\varepsilon_1$. The quantity $B = (\frac{c}{V_o})^2(\varepsilon_3 - \varepsilon_1) + \varepsilon_2^2 - \varepsilon_1^2 - \varepsilon_1\varepsilon_3$ and $C = (\frac{c}{V_o})^2(\varepsilon_1^2 - \varepsilon_2^2 - \varepsilon_1\varepsilon_3) + \varepsilon_3(\varepsilon_1^2 - \varepsilon_2^2)$ where ε_1, ε_2 and
ε_3 are those previously defined. If the numerator of (4-19) is defined
as $T_{33}(n)$, the power expression can now be written as:

$$P(t) = \frac{-q^2 i V_o^2}{(2\pi)^2 \beta \varepsilon_o c^3 \varepsilon_1} \int \left[\int_0^\infty \frac{T_{33}(n) |n| dn}{(n^2 - n_1^2)(n^2 - n_2^2)} \right] |\omega| d\omega \quad .$$
(4-20)

Since the real part of the power is needed, the imaginary part of the
quantity in brackets in (4-20) has to be calculated. To obtain this
imaginary part, the Plemelj formula was used with the result that

$$\int_0^\infty \frac{T_{33}(n) \, |n| \, dn}{(n^2 - n_1^2)(n^2 - n_2^2)} = \frac{\pi i}{2(n_2^2 - n_1^2)} [T_{33}(n_2) - T_{33}(n_1)]$$

$$= \frac{\pi i}{2(n_2^2 - n_1^2)} \sum_{k=1}^{2} (-1)^k T_{33}(n_k)$$

(4-21)

Equation (4-20) now becomes

$$P(t) = \int_{-\infty}^{\infty} \frac{q^2 \, |\omega| \, d\omega}{8\pi \epsilon_o \epsilon_1 (n_2^2 - n_1^2)} \left(\frac{V_o}{c^2}\right) \sum_{k=1}^{2} (-1)^k T_{33}(n_k) \quad .$$

(4-22)

This expression for the radiated power can be compared to Equation 32 of Mansfield [1967]. Assuming that the particle's perpendicular velocity is zero and that wave generation is via the $s = 0$ Landau resonance, then out of the six terms in brackets in Mansfield's Equation 32, only one remains. In the limit that the particle's perpendicular velocity goes to zero, the Bessel function, $J_o(L)$, in Mansfield's Equation 32 goes to one. Consequently, Equation (4-22) is identical to Mansfield's Equation 32 when considering the radiated power from a field-aligned test particle.

2. Radiated Power From N Particles in a Plasma Medium

An expression for the radiated power from N field-aligned test particles is now derived. This derivation is similar to the single particle case derived previously; however, coherence effects between these N radiators will be included.

The source current for the N test particles can be written as:

$$\overline{J}_q(\overline{r}, t) = \sum_{i=1}^{N} q \, \overline{V}_i(t) \delta(\overline{r} - \overline{r}_i(t)) \tag{4-23}$$

with

$$\overline{V}_i(t) = V_{io}\hat{z} \tag{4-24}$$

and

$$\overline{r}_i(t) = (r_{io} + V_{io}t)\hat{z} \tag{4-25}$$

being the velocity and position of the ith particle. Like the single particle case, each of the N particles are field-aligned and are initially located at point r_{io} along the $\hat{z}$-axis. Using (4-12), $\overline{k} \cdot \overline{r}_i$ can be expressed as

$$\overline{k} \cdot \overline{r}_i = \frac{n\omega}{c} \cos \theta \, r_{io} + n\omega \cos \theta \, \beta_i t \tag{4-26}$$

where $\frac{n\omega}{c}$ has been substituted for k and $\beta_i = \frac{V_{io}}{c}$. The Fourier transform of the source current is

$$\overline{J}_q(\overline{k},\omega) = \frac{1}{(2\pi)^4} \iint \overline{J}_q(\overline{r},t) e^{i(\overline{k}\cdot\overline{r}-\omega t)} d\overline{r}dt$$

$$= \sum_{i=1}^{N} \frac{q\, V_{io}\hat{z}}{(2\pi)^4} \int e^{i(\overline{k}\cdot\overline{r}_i-\omega t)} dt \qquad . \qquad (4-27)$$

Substituting (4-26) into (4-27) and using the identity
$\int_{-\infty}^{\infty} e^{i(n\omega \cos\theta\, \beta_i-\omega)t} dt = 2\pi\delta(n\omega \cos\theta\, \beta_i-\omega)$ yields:

$$\overline{J}_q(\overline{k},\omega) = \sum_{i=1}^{N} \frac{q\, V_{io}\hat{z}}{(2\pi)^3} e^{\frac{in\omega}{c}\cos\theta\, r_{io}} \delta(n\omega \cos\theta\, \beta_i-\omega) \qquad . \qquad (4-28)$$

The electric field can now be solved by substituting (4-28) into (4-6):

$$\overline{E}(\overline{r},t) = \sum_{i=1}^{N} \frac{q\, i\, V_{io}}{(2\pi)^3\varepsilon_o} \iint (\overset{..}{T}{}^{-1}\cdot\hat{z})\, e^{\frac{in\omega}{c}\cos\theta\, r_{io}}\, \delta(n\omega \cos\theta\, \beta_i-\omega)$$

$$(4-29)$$

$$e^{i(\omega t-\overline{k}\cdot\overline{r})} d\overline{k}\, \frac{d\omega}{\omega} \qquad .$$

The radiated power from these particles is

$$P(t) = q \sum_{j=1}^{N} \overline{E}(\overline{r}_j, t) \cdot \overline{V}_j(t)$$

$$= \sum_{j=1}^{N} \sum_{i=1}^{N} \frac{q^2 i \, V_{io} V_{jo}}{(2\pi)^3 \epsilon_o} \iint (\hat{z} \cdot \ddot{T}^{-1} \cdot \hat{z}) \, e^{\frac{in\omega}{c} \cos \theta \, r_{io}} \delta(n\omega \cos \theta \, \beta_i - \omega)$$

$$(4\text{-}30)$$

$$e^{i(\omega t - \overline{k} \cdot \overline{r}_j)} d\overline{k} \, \frac{d\omega}{\omega} \qquad .$$

The element $d\overline{k}$ can be written as:

$$d\overline{k} = n^2 \frac{\omega^3}{c^3} \, dn \, \sin \theta \, d\theta \, d\phi$$

and

$$\overline{k} \cdot \overline{r}_j = \frac{n\omega}{c} \cos \theta \, r_{jo} + n\omega \cos \theta \, \beta_j t$$

where $\beta_j = \frac{V_{jo}}{c}$. The radiated power, after performing the integration over ϕ, then becomes:

$$P(t) = \sum_{j=1}^{N} \sum_{i=1}^{N} \frac{q^2 i V_{io} V_{jo}}{(2\pi)^2 \epsilon_o c^3} \iint (\hat{z} \cdot \ddot{T}^{-1} \cdot \hat{z}) e^{\frac{in\omega}{c} \cos \theta (r_{io} - r_{jo})}$$

$$(4\text{-}31)$$

$$e^{i(\omega - n\omega \cos \theta \, B_j)t} \delta(n\omega \cos \theta \, \beta_i - \omega) n^2 \omega^2 \, dn \, \sin \theta d\theta d\omega \qquad .$$

Like the single particle case, the evaluation of the integral

$$I = \int f(x) \, \delta(Ax+B) = \frac{f(x_0)}{|A|}$$

is needed to complete the integration over θ. For (4-31), $A = |n\omega \beta_i|$, $B = \omega$ and $x_0 = \frac{1}{n \beta_i}$. This integration is nonzero only for

$$\cos \theta_{oi} = \frac{1}{n \beta_i} \tag{4-32}$$

which is the Landau resonance condition for the ith particle. Equation (4-31) can now be expressed as:

$$P(t) = - \sum_{j=1}^{N} \sum_{i=1}^{N} \frac{q^2 i V_{io} V_{jo}}{(2\pi)^2 \epsilon_o c^3 \beta_i} \iint (\hat{z} \cdot \overset{\leftrightarrow}{T}^{-1} \cdot \hat{z}) e^{\frac{in\omega}{c} \cos \theta_{io} (r_{io} - r_{jo})}$$

$$\tag{4-33}$$

$$e^{i\omega(1 - \frac{\beta_j}{\beta_i})t} \, |n| \, |\omega| \, dn \, d\omega \quad .$$

The quantity $(\hat{z} \cdot \overset{\leftrightarrow}{T}^{-1} \cdot \hat{z})$ is, again,

$$(\hat{z} \cdot \overset{\leftrightarrow}{T}^{-1} \cdot \hat{z}) = \frac{T_{33}(n)}{\epsilon_1 (n_1^2 - n^2)(n_2^2 - n^2)} \tag{4-34}$$

where $T_{33}(n)$ is the numerator of (4-19) and $n_{1,2} = n_{1,2}(\beta_i)$. Equation (4-33) is reexpressed as

$$P(t) = -\sum_{j=1}^{N}\sum_{i=1}^{N}\frac{q^2 i\, V_{io}V_{jo}}{(2\pi)^2\varepsilon_o c^3\beta_i\varepsilon_1}\int[\int_o^\infty\frac{T_{33}(n)|n|e^{inA}dn}{(n^2-n_1^2)(n^2-n_2^2)}]e^{i\omega(1-\frac{\beta_j}{\beta_i})t}|\omega|d\omega$$

(4-35)

where $A = \frac{\omega}{c}\cos\theta_{io}(r_{io}-r_{jo})$. Since the real part of the power is desired, the imaginary part of the quantity in brackets must be calculated. In this evaluation, only the real part of the exponential, e^{inA}, is considered since only the relative phase of the electron radiators is needed. Using the Plemelj formula, the imaginary part of the integral is

$$\int_o^\infty\frac{T_{33}(n)|n|e^{inA}dn}{(n^2-n_1^2)(n^2-n_2^2)} = \frac{\pi i}{2(n_2^2-n_1^2)}\sum_{k=1}^{2}(-1)^k T_{33}(n_k)e^{in_kA}\ .$$

(4-36)

Substituting (4-36) for the bracketed expression in (4-35) yields the expression for the radiated power from N particles:

$$P(t) = \int_{-\infty}^{\infty}\sum_{j=1}^{N}\sum_{i=1}^{N}\frac{q^2|\omega|d\omega}{8\pi\varepsilon_o\varepsilon_1}\frac{1}{(n_2^2(\beta_i)-n_1^2(\beta_i)}(\frac{V_{jo}}{c^2})e^{i\omega(1-\frac{\beta_j}{\beta_i})t}$$

(4-37)

$$\times\sum_{k=1}^{2}(-1)^k T_{33}(n_k(\beta_i))e^{i\frac{n_k(\beta_i)\omega}{c}}\cos\theta_{io}(r_{io}-r_{jo})\ .$$

The radiated power is reexpressed as

$$P(t) = \int_{-\infty}^{\infty} \sum_{i=1}^{N} \frac{q^2 |\omega| d\omega}{8\pi \, \varepsilon_o \varepsilon_1} \left(\frac{1}{n_2^2(\beta_i) - n_1^2(\beta_i)}\right) \left(\frac{V_{io}}{c^2}\right) \sum_{k=1}^{2} (-1)^k T_{33}(n_k(\beta_i))$$

$$+ \int_{-\infty}^{\infty} \sum_{i=1}^{N} \sum_{j \neq i}^{N} \frac{q^2 |\omega| d\omega}{8\pi \, \varepsilon_o \varepsilon_1} \left(\frac{1}{n_2^2(\beta_i) - n_1^2(\beta_i)}\right) \left(\frac{V_{jo}}{c^2}\right)$$

(4-38)

$$\cdot \, e^{i\omega(1 - \frac{\beta_j}{\beta_i})t} \sum_{k=1}^{2} (-1)^k T_{33}(n_k(\beta_i))$$

$$e^{i\frac{n_k(\beta_i)}{c}\omega} \cos \theta_{io}(r_{io} - r_{jo}) \qquad .$$

In this expression, the first-term represents the incoherently radiated power from the N test particles while the second-term represents the additional power from coherent effects between the N particles. Note these coherent effects depend on a particle's velocity and position relative to all other particles.

The time-averaged power is defined as

$$\overline{P} = \frac{1}{2T} \int_{-T}^{T} P(t)dt \qquad .$$

Averaging (4-37) over time yields the expression:

$$\overline{P} = \int_{-\infty}^{\infty} \sum_{j=1}^{N} \sum_{i=1}^{N} \frac{q^2 |\omega| d\omega}{8\pi \, \varepsilon_o \varepsilon_1} \frac{1}{n_2^2(\beta_i) - n_1^2(\beta_i)} \left(\frac{V_{jo}}{c^2}\right)$$

(4-39)

$$\frac{\sin x}{x} \sum_{k=1}^{2} (-1)^k T_{33}(n_k(\beta_i)) \, e^{i\frac{n_k(\beta_i)}{c}\omega} \cos \theta_{io}(r_{io} - r_{jo})$$

where $x = \omega T (1 - \beta_j/\beta_i)$. Note that if $\beta_i = \beta_j$ ($V_{io} = V_{jo}$), then $\sin x/x \rightarrow 1$ and the radiation coming from particles i and j can be coherent, depending only on the particle's relative position. If a distribution of particles exist with $\beta_i \neq \beta_j$ then the power averaged over very long periods will be nearly equal to the incoherently radiated power from the particles. This result is obtained because $\underset{T\rightarrow\infty}{LIM} \frac{\sin x}{x} = 0$ for $\beta_i \neq \beta_j$, allowing only the terms that describe the incoherently radiated power to remain in (4-39). Note, from (4-39), that if all particles were moving at the same velocity and each had the same initial position, the exponential terms would be unity and the radiated power would be $P = N^2 P_1$, where P_1 is te radiated power from a single test charge.

As an example, the radiated power from two test particles will be written from (4-39):

$$\overline{dP} = \frac{q^2 |\omega| d\omega}{8\pi\varepsilon_o \varepsilon_1} \left[\frac{1}{(n_2^2(\beta_1) - n_1^2(\beta_1))} \frac{V_{1o}}{c^2} \sum_{k=1}^{2} (-1)^k T_{33}(n_k(\beta_1)) \right.$$

$$+ \frac{1}{(n_2^2(\beta_2)-n_1^2(\beta_2))} \frac{V_{2o}}{c} \sum_{k=1}^{2} (-1)^k T_{33}(n_k(\beta_2))$$

$$+ \frac{1}{(n_2^2(\beta_2)-n_1^2(\beta_2))} \frac{V_{1o}}{c} \frac{\sin x_1}{x_1} \sum_{k=1}^{2} (-1)^k T_{33}(n_k(\beta_2))$$

$$\times\ e^{\dfrac{in_k(\beta_2)\omega}{c}} \cos\theta_{2o}(r_{2o}-r_{1o}) \tag{4-40}$$

$$+\ \frac{1}{(n_2^2(\beta_1)-n_1^2(\beta_1))}\ \frac{V_{2o}}{c^2}\ \frac{\sin x_2}{x_2}\ \sum_{k=1}^{2}(-1)^k T_{33}(n_k(\beta_1))$$

$$\left. \times\ e^{\dfrac{in_k(\beta_2)\omega}{c}} \cos\theta_{1o}(r_{1o}-r_{2o}) \right]$$

where $x_1 = \omega T (1 - \beta_1/\beta_2)$ and $x_2 = \omega T (1 - \beta_2/\beta_1)$. The first two terms in the brackets represent the radiated power from single test charge #1 and single test charge #2. These two terms, together, represent the incoherent radiation from the two particles. The last two terms in the brackets represent the effects of coherence on the radiated power from these two test particles. Again, if the particles are moving at the same velocity and have the same initial position, the radiated power is

$$P = 4P_1$$

where P_1 is the radiated power from a single test particle.

Although it is not completely obvious in the analysis, expression (4-37) does indeed describe a Cerenkov radiation process. This fact is easily demonstrated using the Cerenkov (Landau) resonance condition:

$$n_\| = n \cos \theta = \frac{c}{V_b} \qquad . \qquad\qquad (4\text{-}41)$$

Recall that if this condition is not met, the radiated power from the beam is zero (see Equation 4-32). Since the phase velocity of the emitted radiation is $V_{PH} = c/n$, the expression

$$V_b = \frac{V_{PH}}{\cos \theta} > V_{PH} \qquad\qquad (4\text{-}42)$$

can be written using (4-41). Consequently, a necessary condition to obtain radiation from the beam is that $V_b > V_{PH}$, which describes a Cerenkov process.

B. Practical Applications

Expressions (4-37) and (4-39) calculates the radiated power by determining the coherence effect amongst the individual beam electron radiators. This calculation represents a microscopic approach to determining the radiated power. A general macroscopic approach has also been derived and is presented in the Appendix. In this approach, the radiated power from a beam with current density $J_z(z,t)$ is calculated. The macroscopic approach has a distinct advantage over the microscopic approach since any real calculation of the radiated power can be computed easier when considering the macroscopic variable $J_z(z,t)$. Using the microscopic approach, the position and velocity of all N particles as a function of time must be considered. Keeping track of all these

variables on a computer requires large amounts of CPU time. Using the macroscopic approach, however, only requires a calculation of the macroscopic variable $J_z(z,t)$, which on a computer is far easier to calculate. Consequently, for any practical power calculation, Equation (A-10) will be used.

The microscopic approach derived in this section is still an important original work since it is the theoretical basis on which the macroscopic approach is derived. This approach also considers explicitly the concept of radiative coherence between the beam particles; a concept that is only implicitly dealt with in the macroscopic approach.

Calculating the radiated power using either approach requires a knowledge of the beam phase-space configuration. Considering the SL-2 electron beam, the phase-space configuration must be modeled from a particle simulation, since beam particle distributions were not obtained experimentally. There are two reasons for not measuring these distributions directly: first, when the PDP was in free flight, it did not fly through the beam [W. R. Paterson, personal communication, 1986]. When it was on the RMS, it was maneuvered into the beam; however, the instrument that obtains these distributions, the Low Energy Proton Electron Differential Energy Analyzer (Lepedea) instrument, was turned off, since it was feared that a direct hit of the beam on the instrument would alter its sensitivity [W. R. Paterson, personal communication, 1986]. In either case, direct measurements of the electron beam distributions were not obtainable. Second, even if the Lepedea instrument had been turned on and in a favorable position to

measure the beam distribution, the instrument's temporal resolution (1.6 seconds) is not fine enough to directly measure instability-related electron bunching which occurs on the order of $1/\omega_{pe} \sim 10^{-7}$ seconds.

In the next section, the results of a one-dimensional electrostatic particle simulation of the SL-2 electron beam will be reviewed. The velocities and positions of the beam electrons obtained from modeled phase-space distributions will be used to calculate $J_z(z,t)$, and, using (A-10), the Cerenkov radiated power from the beam will be calculated. This calculated power will then be compared to the measured whistler-mode power obtained during the PDP/beam encounter.

CHAPTER V

A ONE-DIMENSIONAL ELECTROSTATIC SIMULATION

OF THE SL-2 ELECTRON BEAM

In order to complete a calculation of the radiated power from the SL-2 electron beam, a knowledge of the electron beam phase-space distribution is required. As mentioned in the previous section, no direct measurement of these distributions were made by the Lepedea instrument on the PDP; thus, the distributions must be modeled. In this section, the results of a particle simulation of the SL-2 electron beam is presented that includes modeled phase-space configurations of the beam that can be used to calculate the radiated power.

To obtain the required beam distribution, a one-dimensional electrostatic model of an electron beam propagating through an ambient plasma is simulated on a computer. Generally, these models use simulation particles that are many times the mass and charge of an electron, and modeling the plasma using these particles is valid only when many of these particles are contained in a Debye cube (Debye length for a one-dimensional system). In this simulation, the ambient plasma consists of electrons represented by simulation particles of negative charge and immobile ions represented by a net positive background charge. The simulation is designed so that initially there is no net charge in the system. The simulation particles representing the

ambient electrons can move freely in this one-dimensional system;
however, they are confined to the system by re-injection boundaries.
Ambient electrons leaving the system at these boundaries are re-
injected with a Gaussian-weighted velocity between zero and the elec-
tron thermal speed. The electron beam is represented by simulation
particles of negative charge that are injected into the system at the z
= 0 boundary with velocities greater than the ambient electron thermal
speed. In this one-dimensional simulation, a cold electron beam is
always injected into the system. In order to keep the net charge in
the system equal to zero, a positive charge equal in magnitude to the
amount of negative beam charge in the system is placed at the z = 0
boundary. This boundary charge imitates the spacecraft charging effect
observed on the beam-ejecting shuttle [Williamson et al., 1985].

In a one-dimensional simulation, only a particle's velocity and
position in one dimension is considered. The total length of the
simulation system is divided up into "grids" of a Debye length, λ_D, in
size. The charge density in each grid, ρ_n, is calculated and the
numerical solution to Poisson's equation, $E_{n+1} = E_n + 1/2(\rho_{n+1} + \rho_n)$,
is used to calculate the electric field in the n+1 grid. The simula-
tion particles are then allowed to move in the system under the
influence of this electric field for a period of time $\Delta t \leq \lambda_D/V_B$, where
V_B is the simulation beam speed. If $\Delta t > \lambda_D/V_B$, the simulated beam
particles are moving more than one grid in Δt and will skip grids.
Since the ambient particles in the skipped grids will not interact with
the beam particle, the modeled system no longer represents reality.

After the simulation particles have evolved, a new charge density and electric field is calculated for each grid and the particles are again allowed to move under the influence of the new electric field. This iterative process continues until the beam-plasma interactions reach a steady-state where then the simulation is terminated.

It is assumed that the particle's position and velocity in the one-dimensional simulated electron beam and plasma is along a static magnetic field line. This alignment allows the simulated particle trajectories to be unaffected by this field. Since the SL-2 electron beam was nearly field aligned during injection, this modeling of the electron beam should yield particle distributions that, for the most part, represent the true physical situation.

Generally, near field-aligned electron beams in test chambers and on shuttle flights tend to expand from twice the radius of the electron generator opening to about two electron cyclotron radii in the radial direction, if the generator opening is less than a gyroradius. This radial or perpendicular expansion decreases the density of the beam as it propagates away from its source. Figure 9 shows pictorially this expansion of the beam. Initially, the beam leaves the electron generator ($z=0$) with a radius r_0 and a density n_0. However, an effect is present that causes the beam to expand perpendicular to the magnetic field with a perpendicular expansion speed of $V_{\perp exp}$. This expansion may be related to edge effects of the generator opening or to Coulomb repulsion of beam electrons. As the beam propagates along the $\hat{z}$-axis at a speed of V_B, the beam radius is expanding according to

the first-order expression $r = r_o + \frac{V_{\perp exp}}{V_B} z$ with the local density of the beam, $n(z)$, changing proportionally. The beam expansion continues until $r \cong r_c$, where r_c is the cyclotron radius. By equating the current at the generator to that at other points along z ($J_o A_o = J(z)A(z)$), a first-order expression for $n(z)$ is obtained:

$$n(z) = \frac{n_o r_o^2}{(r_o + \frac{V_{\perp exp}}{V_B} z)^2} = \frac{n_o}{(1 + \frac{z}{L})^2} \tag{5-1}$$

where

$$L = (\frac{V_B}{V_{\perp exp}}) r_o \quad . \tag{5-2}$$

The scale length, L, represents the beam length where the beam density decreases to $n_o/4$, and is expressed in units of gun radii.

This perpendicular expansion is modeled in the simulation of the SL-2 electron beam. To include this effect, the density of the beam electrons in the simulation are weighted by the factor $\frac{1}{(1+z/L)}^2$, where L is treated as a free parameter. Consequently, the simulation is able to model the density decreases associated with beam expansion which affect the modeled electric fields and beam distributions.

The parameter, L, also indirectly affects the amount of positive charge at the z=0 boundary during simulated beam injections. As

mentioned previously, the amount of positive charge at the z=0 bound-
ary is equal to the amount of negative beam charge in the system.
This charge is placed there in order to conserve the total charge in
the system, and effectively simulates spacecraft charging known to
occur on beam-ejecting spacecraft. As L decreases, the beam density
and total beam charge in the system decreases which also causes the
amount of positive charge placed at the z=0 boundary to decrease.
Consequently, by varying L, both the modeled beam expansion and
boundary charging are altered.

Including these effects in the modeling of the SL-2 electron
beam makes this one-dimensional simulation rather unique. Usually,
to observe the beam character under varying beam expansion and bound-
ary charge, a two-dimensional or three-dimensional simulation is need-
ed; however, by weighting the beam particles properly, this simple
one-dimensional simulation copies processes occurring in these more
advanced simulations. As an example, results from a two-dimensional
simulation performed by Pritchett and Winglee [1986] are compared to
the results from this one-dimensional simulation under similar simu-
lated plasma conditions. Pritchett and Winglee's simulation is very
advanced. In their two-dimensional simulation system, a simulated
spacecraft immersed in a simulated plasma is able to eject a simulated
electron beam. Diagnostic software is included that analyzes the
electric fields and return currents that develop around the beam and
spacecraft. Unlike the one-dimensional simulation, both electron and
ion motion parallel and perpendicular to the static magnetic field are

modeled. Electric fields and currents are also allowed to develop both inside and outside the region where the beam propagates. It would seem that such an advanced simulation would have very different results for the electron beam distributions as compared to this study's one-dimensional simulation; however, this is not the case. Figure 10(a) and (b) shows the V_z versus z phase-space configuration of the beam electrons from Pritchett and Winglee's two-dimensional simulation. For this particular simulation, the ratio of the beam to ambient electron densities, n_b/n_A, is 1/16 and the ratio of the beam to ambient thermal velocities, V_b/V_{TE}, is 10. These figures show the phase-space distribution of the beam after the simulation has run for 32 and 64 plasma periods. Note, in both cases, that particle trapping is evident by the looping structures in phase space. In Figure 10(b), particle heating is occurring between 0-.5 V_B and the front edge of the beam has a filament structure associated with it. Figure 11(a,b) shows the V_z versus z phase-space configuration of the beam electrons from this study's one-dimensional simulation run with similar beam-plasma parameters as Pritchett and Winglee's. For this run, the expansion scale length parameter, L, is 100. Note that the phase-space configuration of the beam has trapping, heating and filament structures very similar to those of Pritchett and Winglee's, and indicates that similar physical processes are being modeled in both simulations.

The beam phase-space configurations from the one-dimensional simulation are dependent on the expansion scale length parameter, L.

Figure 12(a) and (b) show the beam phase-space configuration from the one-dimensional simulation run with similar beam-plasma parameters as Figures 10 and 11, only now $L = \infty$ (no expansion). The phase-space configurations shown in this figure appear noticeably different, particularly at the leading edge of the beam, compared to those shown in Figures 10 and 11 and indicates that particle trapping dominates at this leading edge. Consequently, beam expansion alters the beam phase-space distributions by reducing wave trapping effects.

The modeling of an electron beam using the one-dimensional code works equally well when simulating an overdense beam ($n_b > n_A$) in an ambient plasma. Figure 13 shows a V_z versus z phase-space configuration from the one-dimensional simulation for an overdense beam with $n_b/n_A = 8$, $V_b/V_{TH} = 15$ and $L = 10$. This configuration can be compared with those obtained by Winglee and Pritchett [1986], who also performed a one-dimensional simulation of an overdense beam ($n_b/n_A = 2$). The beam phase-space distribution obtained from their simulation is shown in Figure 14. Note, in both cases, that a large charge build up of the beam particles is present at the injection boundary, with electron bunches forming near the boundary.

The results of these one-dimensional simulations can be compared to the results obtained from Pritchett and Winglee's two-dimensional simulation of an overdense beam. The V_z versus z beam phase-space configuration from their simulation with $n_b/n_A = 8$ and $V_b/V_{TH} \sim 15$ is shown in Figure 15. Note that a charge build up near the injection boundary is again present, along with bunches of slow moving electrons.

For the modeling of both the underdense and overdense beam injections, this study's one-dimensional simulation is capable of replicating the results obtained from the one-dimensional and two-dimensional simulations performed by Pritchett and Winglee. There is one distinct advantage to the one-dimensional simulation and that is, unlike Pritchett and Winglee's two-dimensional simulation, it can run for very long times; thus, allowing the study of the steady-state nature of the beam. Pritchett and Winglee's simulation has to be terminated as soon as about 1% of the beam particles leave the system in order to maintain charge neutrality based on the simulation boundary conditions; and this usually occurs after 60-100 plasma periods when the beam and plasma are still in a transient state. To determine the steady-state beam character, the simulation should be run for longer times.

A. Results of the Simulation of the SL-2 Electron Beam

The one-dimensional electron beam simulation was performed under similar conditions that prevailed during the SL-2 1 keV-50 mA electron beam injection. The simulated plasma parameters during these runs are displayed in Table 1. The 1 keV-50 mA electron beam was initially injected with a density much greater than the ambient electron density. In order to model this overdense beam in the simulation, an electron beam consisting of simulated electron particles was injected into the simulated plasma with a density fives times greater than the ambient electron density. This beam was injected with a velocity $V_B >$ V_{th}, where V_{th} is the ambient electron thermal velocity. In the

region of the ionosphere where the SL-2 electron beam experiment was performed, $V_b \cong 100 \; V_{th}$. Simulations were performed with this

Table 1. Simulation Parameters

n_b/n_A at $z = 0$	5
V_b/V_{th}	20
z	$1200 \; \lambda_D \; (\sim 60 \text{ meters})$
L	2, 3, 5, 10 Gun Radii
t	$270 \; \omega_{pe}^{-1} \; (\sim 1.3 \times 10^{-5} \text{ sec})$
Total number of ambient particles	24000

velocity ratio; however, it was found that V_b/V_{th} could be as low as 20 without significantly altering the beam velocity distributions. Lowering this ratio, however, allows the beam–plasma interactions to occur over shorter length scales, which increases the effective length of the simulation system. Consequently, the simulations were run with V_b/V_{th} = 20, which then increased the effective beam length being simulated by a factor of five without altering the interactions being modeled.

The length of the simulation system was selected to be 1200 simulation units long, which corresponds to a length of approximately 60 meters. This length was selected since it is much larger than the size of the expected beam density perturbations, and allows the simulation to be run in a couple CPU hours.

The results of four simulations run with different L values (2, 3, 5, 10) will be presented. Based on practical arguments of beam expansion, spacecraft charging and wave activity, the model that is most consistent with the SL-2 electron beam will be selected.

A simulation was performed with the plasma parameters shown in Table 1, with L, the beam expansion parameter, equal to 10. Figure 16 shows the V_z versus z phase-space distribution for the first 60 meters (1200 simulation units) of the beam at t = 270 ω_p^{-1}. Note that the beam is strongly decelerated near the z=0 boundary. Figure 17 shows the electric field versus z for this time. The electric field is measured in dimensionless simulation units, where one of these units corresponds approximately to 6 V/m. Note that a very large positive field is present near the z=0 boundary. This electric field is similar to those obtained by Pritchett and Winglee for an overdense beam and results from the strong charging at the boundary. Figure 18 shows the total number of electrons in the beam versus z, and indicates that randomly-spaced density fluctuations are present in the beam; however, as Figure 16 indicates, their velocities are significantly smaller than the initially injected 1 keV-beam velocity. Note from Figure 16 that there is an accumulation of electrons almost lying directly on the z=0 boundary. Many of these electrons have significant negative velocities ($V \sim -V_b/2$). This return electron current has been described in great detail by Katz et al. [1986] and is a result of the large potential that develops near z=0 due to charging.

Beam expansion is increased and spacecraft charging is decreased for the simulation run with L = 5. Figure 19 shows the V_z versus z phase-space distribution of the injected beam for the first 60 meters at t = 270 ω_p^{-1}. The distribution does not appear significantly different from that obtained from the run with L = 10 (Figure 16); however, more electrons are able to escape the region near the charged boundary. Figure 20 shows the electric field versus z at t = 270 ω_{pe}^{-1}. Note that a strong electric field is again generated near the z=0 boundary; a result from charging effects at the boundary. Figure 21 shows the total electron number versus z, again indicating that randomly-spaced density perturbations are escaping from the region near the charged boundary.

Note for both the L = 5 and 10 simulation runs that after 270 ω_{pe}^{-1}, the bulk of the beam electrons have not propagated 30 meters past the injection boundary. In contrast, if the beam had propagated unperturbed, it would have extended out to 135 meters; thus, space-craft charging is drastically altering the character of the beam in these runs. In reality, it may be that large return currents are flowing back to the shuttle along paths unrelated to the beam; such as along magnetic field lines connected to a conducting surface on the shuttle. Such currents may neutralize the spacecraft charge sub-stantially. If this charge is significantly reduced, the beam phase-space distribution will appear as that shown in Figure 22. This result was obtained from a simulation run with L = 3. Note that the beam can propagate freely from the injection boundary. The initially

cold beam becomes thermalized and bunches of electrons propagate from the z=0 boundary. Note that the beam has a significant number of particles with speeds greater than the initial beam velocity. This is an effect of particle acceleration from an electrostatic wave in the beam. This wave is clearly evident in Figure 23, which displays the electric field versus z. Also note from this figure that the strong charging-related electric field near the z=0 boundary is reduced. Figure 24 shows the total number of beam electrons versus z, and indicates that nearly periodic, highly-localized bunches of electrons are present and, from Figure 22, it is concluded that the collective bunch velocity is near or above the initial beam velocity.

Figure 25 shows the V_z versus z beam phase-space distribution from the simulation run with L = 2 at t = 270 ω_p^{-1}. Note that the beam can again propagate freely from the z=0 boundary. Also, note from this figure, that electron bunches are clearly evident at the top of the elongated looping phase-space structures. Figure 26 displays the electric field versus z at this time. Note that strong electrostatic wave turbulence is present in the beam; however, the relative amplitude of this wave decreases as a function of z. This wave amplitude decrease is an effect of the extreme width-wise beam expansion being simulated. This expansion causes the beam density to strongly decrease as a function of $1/z^2$, which strongly decreases the turbulent electric field according to Poisson's equation. The magnitude of the wave then decreases as the density of the perturbing electrons

decreases. Figure 27 shows the total number of beam electrons versus z. Note that highly localized bunches are evident in the beam.

In Chapter III, calculations were made assuming the bunches had a length, ΔL, of about 7 meters. This bunch length is clearly quite different from those obtained from the simulation. For the runs at L = 2 and 3, the bunches are highly localized ($\Delta L \sim .1-.5$ m), nearly periodic, fast-moving groups of charges, while for L = 5 and 10, only small randomly-spaced density fluctuations exist in the beam. The density character of the beam in both cases differ from that described in Chapter III, since the simulation is modeling nonlinear wave and spacecraft charging effects occurring in the beam. These effects can drastically alter the beam character and were not included in the simple calculations performed in Chapter III.

As mentioned previously, a choice between the four different beam models must be made to determine which correctly models the SL-2 electron beam. The models presented can be classified according to spacecraft charging's influence on beam propagation. For the runs with L = 5 and 10, spacecraft charging is able to drastically alter the injected beam, while for runs with L = 2 and 3, the beam is only slightly influenced by charging effects. In reality, the importance of charging depends on the ability of the shuttle to effectively conduct return currents that neutralize the positive charge created during electron beam ejections.

Williamson et al. [1985] have shown that during SL-2 electron beam injections, the shuttle only charged up to between 0 and 40

volts. Consequently, enough return current was drawn from the iono-
spheric plasma to sufficiently neutralize the positive spacecraft
charge, and this charge neutralization allowed the beam to propagate
freely from the shuttle [Banks et al., 1985]. A beam freely escaping
the near-shuttle region is consistent with the simulations run with L
= 2 and 3, and rules out the L = 5 and 10 simulation runs as possible
models of the SL-2 beam.

Figure 26 displays E_z versus z for the simulation run with L = 2.
As mentioned previously, a self-consistent electrostatic wave is pre-
sent in the beam with an amplitude that decreases with increasing z,
and has a frequency near ω_{pe}. From the figure it appears that the
wave has an amplitude barely above simulation noise level in regions
of the beam where z > 7 meters (150 simulation units). This modeled
wave activity is inconsistent with observations made by the PDP on the
RMS, where strong electrostatic wave turbulence near ω_{pe} was detected
by the PDP radio receivers in regions of the beam where z > 7 meters.
This model of the beam is then ruled out as a realistic model of the
SL-2 electron beam.

From the above arguments, it seems that the simulation run with
L = 3 is the best model of the SL-2 electron beam. There are two
more points to support this conclusion. The first point involves the
energy spectrum of the backscattered beam electrons detected near
magnetic conjunction by the Lepedea instrument. Apparently, these
electrons were not monoenergetic, but were observed at all energies
from 2 eV, the lowest Lepedea channel, to about 1 keV [W. R. Paterson,

personal communication]. If nearly-elastic collisional processes dominated the backscattering, the beam distribution would also have a similar energy spectra, which is consistent with the L = 3 simulation run (see Figure 22). Also, from Figure 23, strong wave activity is present in the beam for this run. These waves have a frequency near ω_{pe} and are similar to those observed by the PDP in the beam. Consequently, the beam model with L = 3 is consistent with the observed beam spectra, wave activity, and spacecraft charging during the 1 keV −50 mA electron beam injection, and is clearly the best beam model.

B.   The Radiated Power From a Model of the SL-2 Electron Beam

The radiated power from the modeled SL-2 electron beam will now be calculated. This power will be compared to the measured whistler-mode power to determine if coherent Cerenkov radiation from a bunched beam is a viable wave generation mechanism.

It has been assumed throughout this analysis, that the magnitude of the electric field of the generated Cerenkov radiation is much smaller than that of the electrostatic wave generated within the beam, $E_{ES} \gg E_{RAD}$. This assumption implies that the radiation electric field did not significantly alter the SL-2 beam electron trajectories, and is consistent with the modeling of the beam where radiation field effects are neglected. This assumption is also consistent with observations made during the SL-2 experiment, where $E_{ES} > .3$ V/m in the beam while $E_{RAD} \sim 10^{-3}$ V/m for the whistler-mode waves.

The radiated power from N particles in a specific length segment of the beam can be calculated using equations (4-37) and (4-39). To

actually compute the power using these expressions, however, requires large amounts of costly computer time. An easier way to calculate the power is to use the expression (A-10):

$$P(t) = \overline{P} = \int\limits_{-\infty}^{\infty} \left(\frac{|\omega|\,d\omega}{8\pi\ \varepsilon_0\varepsilon_1 c^2 V_s}\right)\ \frac{1}{(n_2^2-n_1^2)}\ \sum_{k=1}^{2}(-1)^k\ T_{33}(n_k)$$

$$\times\ [2\pi\ J_z(k_z(n_k,\theta_o))J_z^*(k_z(n_k,\theta_o))]\quad .$$

(A-10)

In this expression, V_s is the velocity of the frame moving with the beam such that the current density, $J_z(z,t)$, is considered time independent. In deriving (A-10), a transformation to this frame was made in order to calculate the radiated power from a specific beam segment. Consequently, $J_z(z,t)$ becomes $J_z(z')$ in this new frame, where $z' = z - V_s t$. In (A-10), $J_z(k_z)$ represents the spatial Fourier transform of $J_z(z')$. Once $J_z(k_z)$ of a specific beam segment is known, the power radiated from that segment is easily calculated. As mentioned in Chapter IV, calculating the power using macroscopic variable $J_z(z,t)$ requires less computer time than calculating the radiated power from each particle. In deriving expression (A-10), it has been assumed that a frame of reference exists where the current density is completely independent of time. In this frame, all beam density perturbations have to propagate at identically the same speed, V_s. The transform of the current density is then properly expressed as (A-4), with the delta function specifying the speed of the density

perturbations. This subtle condition placed on the propagation speed
of the perturbations reduces the generality of equation (A-10) com-
pared to equation (4-37) which expressed the radiated power from N
electrons with arbitrary speeds. Despite this reduction in general-
ity, it will be shown that (A-10) is quite capable of yielding a rea-
sonable estimate of the radiated power from the modeled SL-2 electron
beam with bunches moving at or near V_s. It should be noted that in
the frequency range of consideration, $n_1 \gg n_2$, $n_1 \equiv n$ where n is the
whistler-mode index of refraction obtained from cold plasma theory and
$T_{33}(n_1) \equiv 10^3 T_{33}(n_2)$. Also, based on arguments of the typical den-
sity structure size in the beam, $J_z(k_z(n_1,\theta_0)) > J_z(k_z(n_2,\theta_0))$. Con-
sequently, the k=2 term in the summation of Equation (A-10) is very
small and can be neglected. The radiated power can then be expressed
as

$$P(t) = \overline{P} \equiv \int_{-\infty}^{\infty} \left[\frac{-|\omega|d\omega}{8\pi \ \varepsilon_0 \varepsilon_1 c^2 V_s} \ \frac{1}{(n_2^2-n_1^2)} \right] [2\pi J_z(k_z')J_z^*(k_z')]T_{33}(n_1) \quad (5-3)$$

where $k_z' = \dfrac{n \cos \theta_0 \omega}{c}$. Note that $n_1 > n_2$ which makes the term in
brackets positive in the frequency range considered.

A simulation of the SL-2 electron beam was run with a simulation
length three times longer than those run previously. This simulation
length now extends 3600 grid lengths and represents a model of the
first 180 meters of the SL-2 electron beam. This increased length was

added to improve the resolution of $J_z(k_z)$ in the whistler-mode range
of k_z'. The V_z versus z phase-space configuration for this modeled
beam at $t = 840\ \omega_{pe}^{-1}$ is displayed in Figure 28. Note that this
phase-space configuration is very similar to the phase-space configu-
ration of the 60-meter beam segment displayed in Figure 22. Both con-
figurations have two electron components: a strongly heated component
found in phase-space regions where $V < V_b$ and electron bunches found
in phase-space regions where $V > V_b$. These bunches are particularly
pronounced in the first 75 meters of the beam (from z = 0 to 1500).
Using Equation (5-3), the radiated power will be calculated from a
beam-segment extending 175 meters in length from z = 100 to 3500. The
first five meters of the beam is not included in the calculation since
the beam phase-space configuration near the generator (z = 0 boundary)
is atypical of the rest of the beam. The power radiated from this
175-meter segment is equal to the Poynting flux through a cylindrical
surface of radius R and length L = 175 meters surrounding the beam:

$$P_{175m} = S_\perp\ 2\pi R\ L\ (175m)\ .\tag{5-4}$$

Since the radiated power varies directly with L, the power from a
200-meter beam segment can be approximated by

$$P_{200m} = (200/175)\ P_{175m}\ .\tag{5-5}$$

A quantity that has to be determined in (A-10) is V_s, the velocity where the current density, $J_z(z,t)$, is considered independent of time. This current density consists of two parts, $J_z(z,t) = J_0(z,t) + J_1(z,t)$. The quantity $J_0(z,t)$ represents the current density from the randomized electrons found in regions of phase space where $V_z < V_b$. The current from these electrons is flowing continuously at a nearly constant value thus $J_0(z,t) = J_0(z)$. The quantity $J_1(z,t)$ represents the current density from the density perturbations or bunches in the beam found in regions of phase space where $V_z > V_b$. The current from these perturbations is time dependent, with bunches passing a point $z = z_0$ at a periodicity of approximately $1/\omega_{pe}$. Consequently, the current density can be rewritten as $J_z(z,t) = J_0(z) + J_1(z,t)$. The frame of reference where $J_z(z,t)$ appears stationary is then a frame that is moving with the bunches since $J_1(z,t)$ is the only time-dependent term in the current density. From Figure 28 it is evident that the bunches are propagating at $V \cong 1.5 V_b = 2.8 \times 10^7$ m/s; thus, $V_s = 2.8 \times 10^7$ m/s.

Bunches created by an electrostatic wave in the beam propagate near the phase speed of the wave, $V_{ph} = \omega/k_z$. The frame where $J_z(z,t)$ is considered time independent is then a frame moving with this wave, $V_s = V_{ph}$. To determine the wave phase speed, the Fourier transform of $J_z(z,t)$, in both time and space for the 175-meter beam segment is calculated and plotted as a function of ω and k_z. This plot is displayed in Figure 29. If the perturbations in current density result from beam interaction with an electrostatic wave, then J_z

(k_z, ω) will be most intense near V_{ph}. Note from the figure that J_z (k_z, ω) does indeed peak near $\omega/k = V_{ph} = 2.8 \times 10^7$ m/sec, which is represented by the solid line in the figure. Consequently, if a transformation is made to a frame moving at $V_s = V_{ph} = 2.8 \times 10^7$ ms/s, the current density appears nearly stationary. Note also from the figure that all the bunches are not moving exactly at V_{ph}, but have a spread in velocity in a range $\pm \Delta V$ about V_{ph}. Consequently, in the moving frame, some second-order temporal perturbations in the current density will be present and must be considered in the calculation of the radiated power. As will be shown later, these second-order perturbations will not significantly alter the calculation of the radiated power.

The current density calculated from the 175-meter segment is considered the density in the frame moving at V_s, $J_z(z')$, where $z' = z - V_s t$; and the Fourier transform of this current density, $J_z(k_z)$, will be used in (5-3) to determine the radiated power from this segment. The transform of a 175-meter beam segment will yield discrete values of $J_z(k_z)$ at each $k_z = 2\pi m/175$ meters where m is an integer from 0 to 1750. A plot of $J_z(k_z)$ versus k_z is displayed in Figure 30. The resulting transform appears as a white-noise type k-spectra for $k_z >$ 22; however, for $k_z < 22$, $J_z(k_z)$ appears to increase as k_z decreases. The white-noise type k-spectra found in $k_z > 22$ results from the randomized position and velocity of the simulation electrons used in the computer model. This noise is inherent in the modeled system since simulation electrons many times the mass and charge of real electrons

were used in the model. Although not feasible, if real electrons had been modeled, this noise would be reduced to nearly zero. The average noise level was calculated by summing the $J_z(k_z)$ values between k_z = 28.7 and 62.8 and dividing by the number summed. This level is represented by the dotted line in the figure. The increase in $J_z(k_z)$ found in $k_z < 22$ results from wave-particle interactions within the beam that create localized charged regions or bunches. If bunching had not occurred, the simulated beam electrons would be randomly spaced in both velocity and position and the resulting $J_z(k_z)$ would appear as a white noise type k-spectra at all k_z values.

To solve (5-3), $J_z(k_z)$ evaluated at $k_z' = n \cos \theta_0 \omega/c$ is required. This $k_z'(\omega)$ represents the wave numbers that satisfy the Landau resonance condition and varies from .01 at 31.1 kHz to .25 at 1 MHz. The $J_z(k_z)$ values that correspond to k_z' are presented, graphically, in Figure 30. Note from this figure that six values of $J_z(k_z)$ fall in the range of k_z' for the whistler-mode. Table 2 lists these $J_z(k_z)$ values with the simulation noise level subtracted at their corresponding k_z' and $f(= V_s k_z'/2\pi)$. Using Equation (5-3) and (5-5), the radiated power spectral density, dP/df, from a 200-meter beam segment is evaluated at each of the six frequencies. These values are plotted as a function of wave frequency in Figure 31 (represented by x's) along with the calculated incoherent Cerenkov power spectra (represented by o's) and measured whistler-mode power spectra (represented by .'s) from the 200-meter SL-2 electron beam segment.

Table 2. Values of $J_z(k_z)$

k_z (1/m)	f (kHz)	$J_z(k_z)$ (Noise Level Subtracted)
.0395	176	.092
.0790	352	.035
.1185	529	.192
.1580	705	.067
.1975	881	.123
.2370	1057	.112

Note that the inclusion of coherent effects amongst the beam electrons increases the wave powers by almost 10^9 (90 dB's) above incoherent power levels. Also note that the coherent power level is near the measured whistler-mode powers. It is clear from the figure that coherent Cerenkov radiation from the beam can indeed account for the measured whistler-mode wave power. In fact, the calculated power from the modeled beam overestimates the measured power by about a factor of 10. This disagreement may result from the fact that both the computer simulation of the beam and the power calculations were performed in only one dimension. In this case, motion of the beam electrons per-pendicular to the static magnetic field have been neglected. Such motion, as the electron's gyromotion, can change the radiative coher-ence of the beam electrons by giving them a significant displacement perpendicular to the geomagnetic field. Also, the one-dimensional

simulation of the beam has completely neglected any finite radius effects that occurred in the SL-2 electron beam. These effects can reduce the amplitude of the electrostatic wave in the beam, which correspondingly reduces Δn, the beam density perturbations. The radiated power from the SL-2 electron beam with its finite radius should then be less than the predicted radiated power from the model. Landau damping of the whistler-mode waves in the SL-2 electron beam may also reduce wave powers. This damping occurs because the Cerenkov radiation emitted by the bunches with a phase speed, $V_{ph} < V_s$, is able to interact with the heated component of the beam. This damping is not considered significant, however, since the path length for damping (as well as wave growth) in the SL-2 electron beam is very short. Consequently, the radiation will not interact with the thermalized beam component long enough to be altered significantly.

Note in Figure 31 that the frequency range of the modeled coherently radiated power does not extend below 176 kHz. This low frequency limit results from the discreteness of the $J_z(k_z)$ values used in the calculations. For a 175-meter beam segment, values of $J_z(k_z)$ can only be obtained at specific k_z and f values; namely, at $k_z = 2\pi m/175$ meters and $f = mV_s/175$ meters, where m is an integer extending from 0 to 1750. Consequently, the first nonzero frequency where a $J_z(k_z)$ value exists and the power can be determined is at 176 kHz. Values of power spectral density cannot be obtained below this frequency for a beam of this length. Increasing the beam length will allow the radiated power to be determined at lower frequencies;

however, the computer run time will also be increased, possibly beyond
practical considerations. As an example, a calculation of the
radiated power at 50 kHz would require nine times the CPU time cur-
rently used (from 24 to 216 VAX CPU hours) and a similar calculation
at 31 kHz would require a twenty-five times increase in CPU time (from
24 to 600 VAX CPU hours). Clearly, power calculations at these lower
frequencies are not feasible.

Based on the results of the simulation, the measured whistler-
mode powers calculated in Chapter II and displayed in Figures 6 and 31
should be corrected to account for the radiation emitted by bunch
electrons moving at speeds 1.5 times greater than the initial injec-
tion speed. The original calculation of this power assumed that all
the beam electrons were moving at their initial injection velocity of
1.89×10^7 m/sec which, from the Landau resonance condition, corre-
sponds to a value of $n_{\parallel} = 15.9$. This value of $n_{\parallel}$ was used to
constrain the values of $\bar{n}(\theta)$ obtained from cold plasma theory and
specified the values of n and $\Delta\theta$ used in the magnitude of the Poynting
vector, expression (2-2). From the simulation, however, it is evident
that the radiation is emitted from electron bunches moving at $V_s = 2.8$
$\times 10^7$ m/sec, which corresponds to a value of $n_{\parallel} = 10.7$. As a conse-
quence, the measured power is about 50% greater when considering
radiation from the faster moving bunches. Although this increase is
insignificant compared to the factor of 10 difference between measured
and coherent Cerenkov power values, it still should be mentioned.
Recall that the Landau resonance had to be incorporated into the

measured power calculations since complete information on $\overline{E}$ and $\overline{B}$ of the measured whistler-mode waves was unavailable. The measured power is then considered a model dependent quantity based on values of $n_{\parallel}$.

As mentioned previously, all the bunches in the beam are not propagating at exactly V_s, but instead propagate in a range of velocities, $V_s \pm \Delta V$, where ΔV is the typical velocity spread. Consequently, in the moving frame, the current density is not completely independently of time as assumed in the derivation of (5-3), but has second-order temporal variations that can alter the radiative coherence of the beam. The effect of these temporal variations on the radiated power will now be considered.

Consider a current density that varies as $J_z(z') \, e^{-t^2/t_o^2}$, where t_o represents the typical time of the temporal variations in the current density. The corresponding transform of this current density in space and time is written as

$$\overline{J}_q(\overline{k},\omega) = \frac{\hat{z}}{(2\pi)^3} \sqrt{2\pi} \, J_z(k_z) \left[\frac{t_o}{2\sqrt{\pi}} \, e^{-a^2 t_o^2/4} \right] \qquad (5\text{-}6)$$

where $J_z(k_z)$ is the spatial transform of the current density and $a = k_z V_s - \omega$.

If the electrostatic wave in the beam is monochromatic, the corresponding density perturbations propagate at the phase speed of

this wave. The transform of the current density is then peaked at ω/k_z values where $\omega/k_z = V_{ph} = V_s$, with no spread in ω or k_z. In this case, the current density is properly represented by (A-4). However, as Figure 29 indicates, the transform of the current density has a significant spread about $\omega/k_z = V_{ph} = V_s$. Consequently, this transform is best represented by (5-6), where the delta function in (A-4) is replaced by Gaussian function centered at $\omega/k_z = V_s$. Note as $t_o \to \infty$, the two expressions become identical.

Following a similar analysis as that of the Appendix, the radiated power is found to be

$$P(t) = \frac{i}{(2\pi)^3 \varepsilon_o} \iint \frac{(\hat{z} \cdot \ddot{\bar{T}}^{-1} \cdot \hat{z})\, [2\pi\, J_z(k_z) J_z(k_z)^*]}{\frac{t_o}{2\sqrt{\pi}} e^{\frac{-a^2 t_o^2}{4}}} \; e^{-\left(\frac{t^2}{t_o^2} + iat\right)} d\bar{k}\, \frac{d\omega}{\omega} \qquad (5\text{-}7)$$

The time-averaged radiated power is now calculated. This power is defined to be

$$\bar{P} = \frac{1}{2T} \int_{-T}^{T} P(t)\, dt \qquad (5\text{-}8)$$

where T is the time interval over which the power is averaged. An integral of the form

$$I = \frac{1}{2T} \int_{-T}^{T} e^{-\left(\frac{t^2}{t_o^2} + iat\right)}\, dt \qquad (5\text{-}9)$$

must now be solved. Expression (5-9) can be reexpressed as

$$I = \frac{e^{\frac{-a^2 t_o^2}{4}}}{2T} \int_{-T}^{T} e^{-(\frac{t}{t_o} + \frac{iat_o}{2})^2} dt \qquad . \tag{5-10}$$

The whistler-mode radiation detected by the PDP radio receivers at any instant in time is generated from a beam length segment, ℓ. The typical time an electron spends in ℓ is $\varepsilon = \ell/V_b$. Consequently, (5-10) can be rewritten as

$$I = \frac{e^{\frac{-a^2 t_o^2}{4}}}{\varepsilon} \int_{o}^{\varepsilon} e^{-(\frac{t}{t_o} + \frac{iat_o}{2})^2} dt \qquad . \tag{5-11}$$

Since ℓ is small, $\varepsilon \ll t_o$ and (5-11) is near unity.

The average radiated power is then

$$\overline{P} = \frac{1}{(2\pi)^2 \varepsilon_o c^2} \int (\hat{z} \cdot \overset{\leftrightarrow}{T}^{-1} \cdot \hat{z})[2\pi \, J_z(k_z)J_z^*(k_z)] \frac{t_o}{2\sqrt{\pi}} e^{\frac{-a^2 t_o^2}{4}} n\omega \, dn \, d\omega \, dk_z$$

$$\tag{5-12}$$

where $\overline{dk} = \frac{n^2\omega^3}{c^3} dn \sin \theta \, d\theta \, d\phi = \frac{n\omega^2}{c^2} dn \, dk_z \, d\phi$. Equation (5-12) can be expressed as

$$\frac{dP}{d\omega}\bigg|_{\omega=\omega_o} = \int F(k_z,\omega_o) \frac{t_o}{2\sqrt{\pi}} e^{\frac{-a^2 t_o^2}{4}} dk_z \qquad . \tag{5-13}$$

Table 3. The Change in Radiated Power From Considering a Current Density With a Spread, Δk.

Frequency	$\frac{dP}{d\omega}(\Delta k_z = k_{zo})/\frac{dP}{d\omega}(\Delta k_z \to 0)$
562 kHz	.930
311 kHz	.887
178 kHz	.924
100 kHz	.942
56.7 kHz	.979
31.1 kHz	1.031

CHAPTER VI

THE ELECTRON BEAM AS AN EFFICIENT ANTENNA

In this study, it has been concluded that the whistler-mode emission detection from the SL-2 electron beam is created by coherent Cerenkov radiation from electron bunches in the beam. Consequently, the electron beam is considered an antenna radiating the whistler-mode radiation. As will be shown, by positioning the radiating bunches properly in the beam, the radiation efficiency of this "antenna" can be improved. Consider, first, the bunches formed in the continuous SL-2 electron beam. From Figure 22 it is evident that these bunches have a length, $\ell = .1-.5$ meters and have a spacing, $d \cong 6$ meters, apart from each other. This bunching of the modeled beam is clearly evident in Figure 30 which displays $J_z(k_z)$ versus k_z. In this figure the maximum $J_z(k_z)$ value is near $k_z \cong 2\pi/d \cong 1$ corresponding to the typical bunch spacing. Note that this maximum value lies outside the range of k_z' of the whistler-mode radiation. More power in the whistler-mode would have been obtained from the beam if this maximum $J_z(k_z)$ value had been in the k_z' range. In this case, the spacing between the bunches would then be equal to the parallel component of a whistler-mode wavelength, $d = \lambda_\parallel$; and the coherent radiation from the bunches in the beam at $f = V_s/\lambda_\parallel$ would constructively interfere. This

process would significantly increase the wave powers above those measured from the SL-2 electron beam to near 10^{-6} W/Hz at $f = V_s/\lambda_\parallel$.

This effect can be artificially induced by pulsing the electron beam near the whistler-mode range of frequencies. Unlike the continuous beam, a beam-plasma instability is now undesirable, since it tends to destroy the highly coherent pulses ejected from the gun. Consequently, to reduce the effects of the instability, the length of the pulses, ℓ, should be $\ell \ll V_b/f_{pe}$, where V_b/f_{pe} represents the characteristic length over which the instability acts and is the wavelength of the instability-related electrostatic wave. Also, the spacing between the pulses, d, should be equal to a parallel component a whistler-mode wavelength, $\lambda_\parallel$. If these two conditions are met, the radiated power at $f = V_b/d$ will be quite intense. As an example, consider a 1 keV - 50 mA electron beam in the same plasma environment as the continuous SL-2 electron beam, however, pulsed such that

$$J_z(z) = \sum_{n=0}^{p} NqV \; \delta(n \; 31.4 \text{ meters})$$

where p is the number of pulses in a 200-meter segment (equal to 6). In this idealized example, the individual pulses have an infinitesimally small length, ℓ, and are spaced 31.4 meters apart from each other. For a 1 keV -50 mA electron beam, $V = 1.89 \times 10^7$ m/sec and $N = 4.9 \times 10^{11}$ electrons. The value of k_z corresponding to the pulse spacing, d, is $k_z = .2$. The Fourier transform of $J_z(z)$ is

$$J_z(k_z) = \sum_{n=0}^{p} \frac{NqV}{\sqrt{2\pi}} \int_{-\infty}^{\infty} \delta \ (n \ 31.4) \ e^{ik_z z} \ dz = \sum_{n=0}^{p} \frac{NqV}{\sqrt{2\pi}} \ e^{in \ 31.4 \ k_z} \ .$$

Note that at $k_z = .2$, $J_z(k_z)$ is a maximum since the exponential term, representing the relative phase difference between the pulses, goes to unity. Consequently,

$$J_z(k_z = .2) = \frac{6NqV}{\sqrt{2\pi}} = 3.56 \ .$$

From the Landau resonance condition, this value of k_z corresponds to a frequency of 600 kHz. The radiated power is then a maximum at this frequency and is calculated to be $\sim 3 \times 10^{-4}$ W/Hz from a 200-meter pulsed beam segment. Note that this power is over 10^5 greater than those measured by the PDP. Consequently, the constructive interference amongst the pulses increases the radiated powers drastically.

CHAPTER VII

CONCLUSIONS

The whistler-mode radiation detected by the PDP during its flyby of a 1 keV — 50 mA electron beam has these characteristics:

A) The radiation is propagating near the resonance as determined by the electric field polarization.

B) About 1.6 mW of the radiation is emitted from the first 200 meters of the beam, corresponding to about 8×10^{-6} W/m of emitted radiation from the beam.

C) The calculated wave powers from the beam are well above those expected from incoherent Cerenkov radiation processes in the beam.

Many mechanisms have been discussed to account for the detected signal; however, the best mechanism is coherent Cerenkov radiation from density perturbations or bunches in the beam. These bunches are created by an electrostatic beam-plasma instability occurring within the beam.

The existence of these bunches is verified in two ways: first, when the PDP was in the beam, radio receivers detected very intense waves near ω_{pe}. These waves are believed to be associated with the instability creating the bunches. Second, a one-dimensional computer simulation of the beam clearly shows the presence of electron bunches in the beam.

The calculated power from the simulated beam indicates that the radiation from electrons in bunches is coherent enough to account for the measured whistler-mode power. Consequently, from this study it is concluded that the whistler-mode radiation from the SL-2 electron beam is generated by coherent Cerenkov radiation from a bunched electron beam.

Figure 1   A frequency vs. time spectogram from the PDP plasma
            wave instrument showing intense emissions during a D.C.
            electron gun firing. The funnel-shaped structure that
            extends from the electron cyclotron frequency, f_c, to
            about 30 kHz is whistler-mode radiation from the beam.

A-G85-807-1

PDP, DAY 213, AUG. 1, 1985
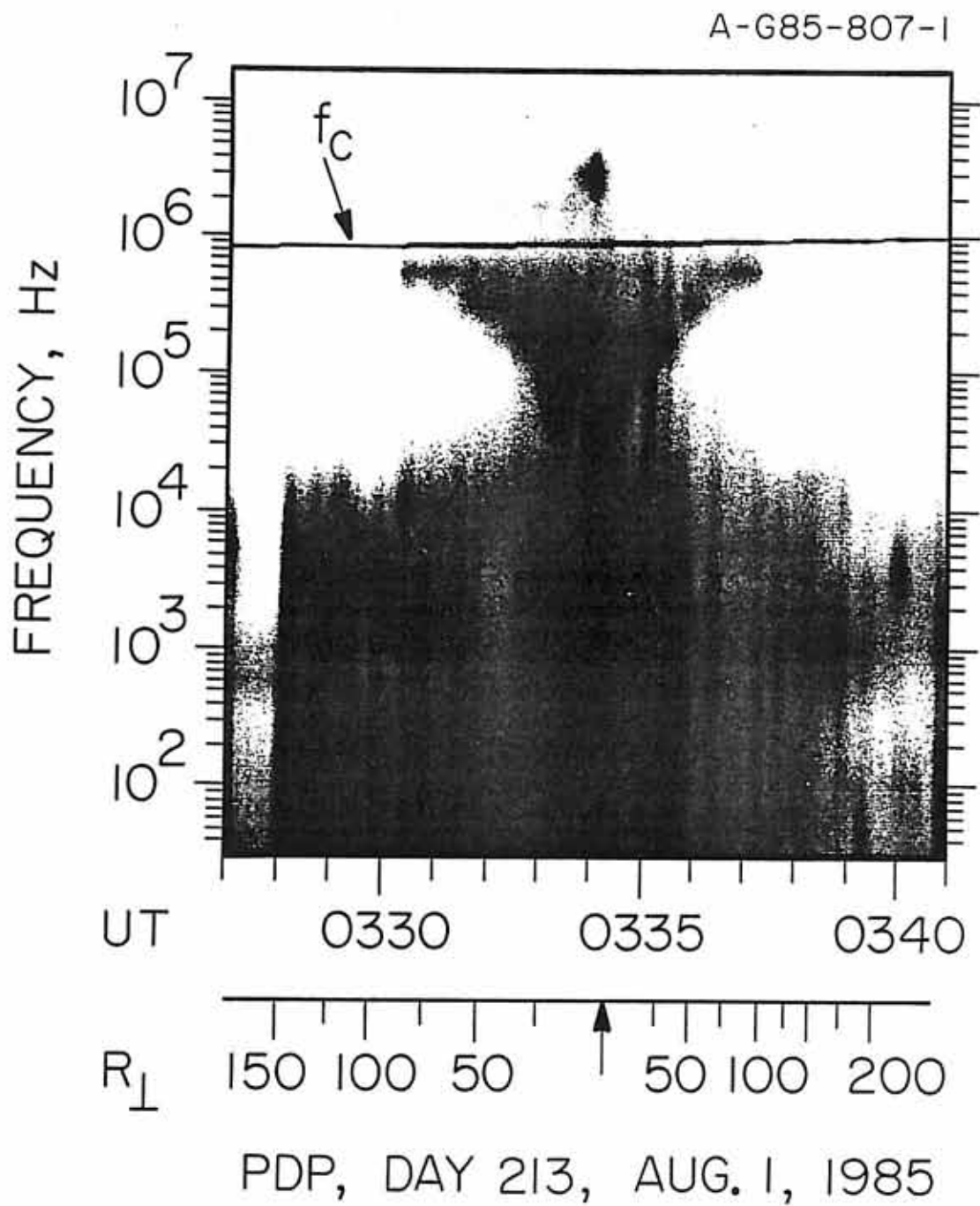
Figure 2   This diagram shows the index of refraction surface for the whistler mode and the associated $\overline{E}$, $\overline{k}$, and $\overline{v}_g$ vectors for propagation near the resonance cone ($\theta \simeq \theta_{Res}$). For propagation near the resonance cone, $\overline{k}$ and $\overline{E}$ are parallel and nearly perpendicular to $\overline{v}_g$. In this limit $\overline{E}$ is linearly polarized and quasi-electrostatic.
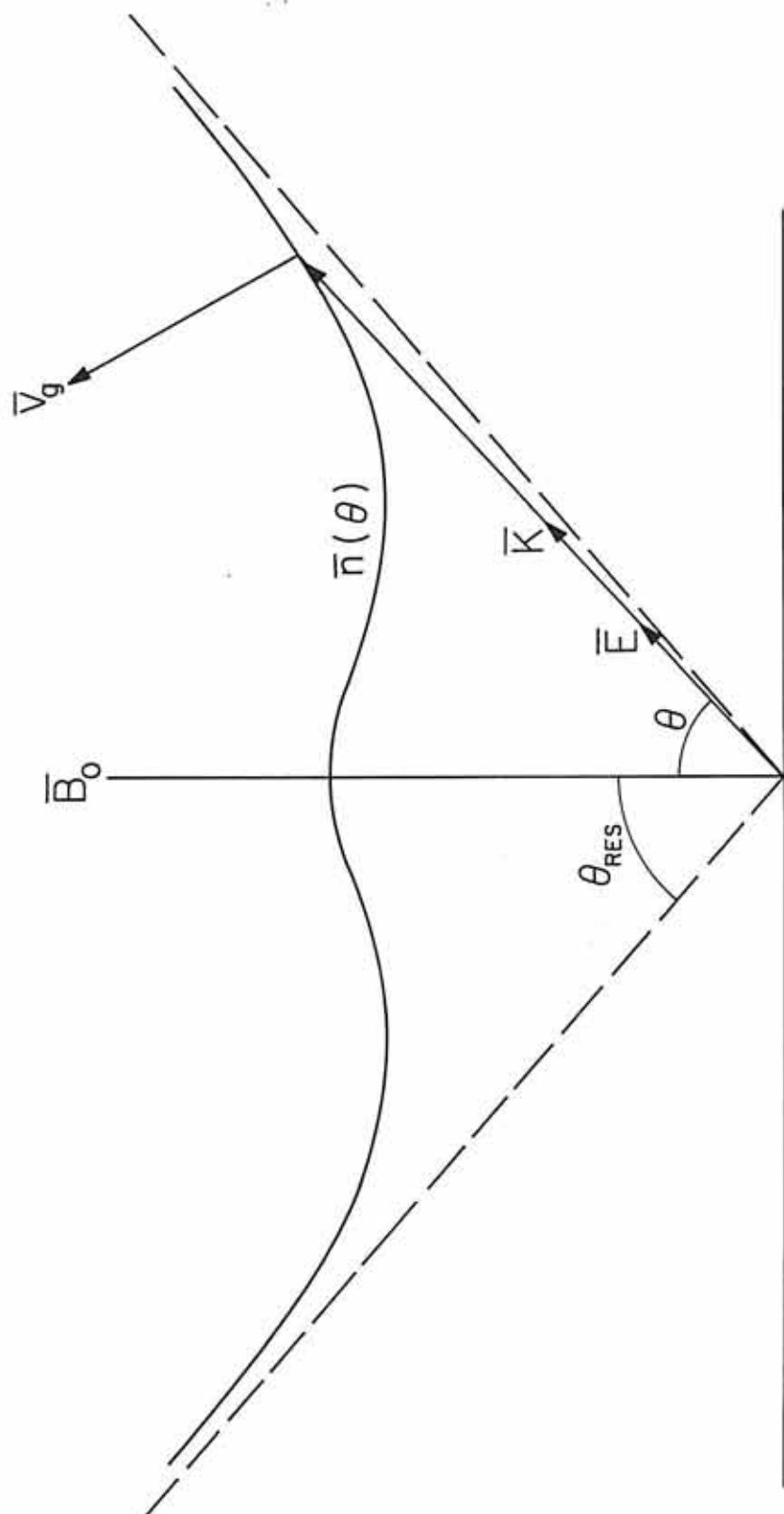
Figure 3   This diagram shows the ray path and $\overline{E}$, $\overline{k}$, and $\overline{v}_g$ vectors used to confirm the electric field polarization. The assumed electric field is projected into the PDP spin plane and the angle relative to the projection of the sun vector is calculated. The projected electric field direction can then be compared to the measured directions calculated from spin modulation maximums in the electric field intensity (see Figure 4).

B-G86-582-I

$\overline{B}_o$

$\overline{V}_{BEAM}$

$\overline{E}$ PROJECTION

ϕ

SUN VECTOR
PROJECTION

PDP SPIN PLANE

$\overline{V}_g$

MODEL
$\overline{E}, \overline{k}$

θ_{RES}

BEAM
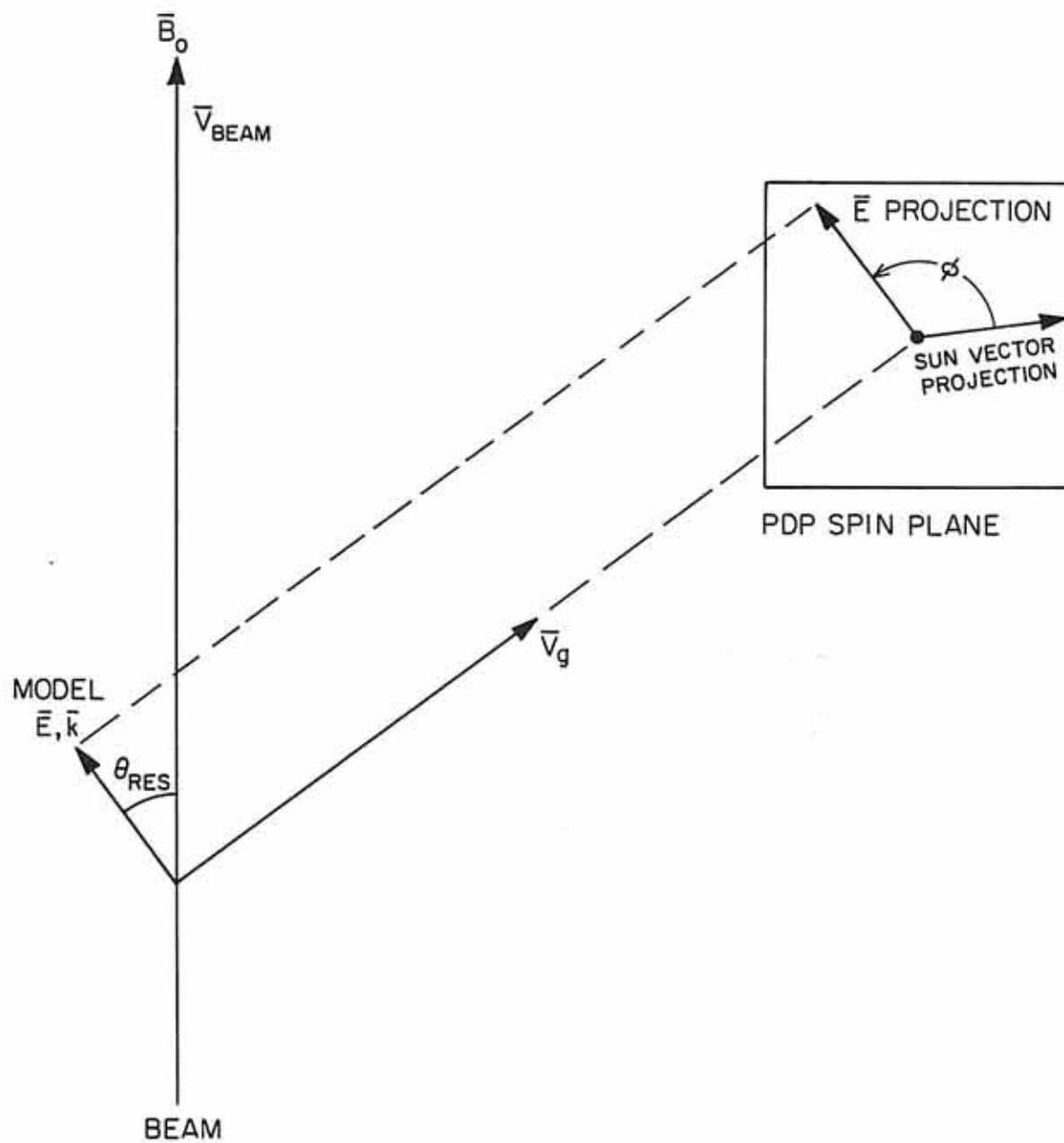
Figure 4(a), (b), (c), and (d) These plots show the relative directions
of the computed and measured electric-field vectors in the
PDP spin plane for the 562 kHz, 311 kHz, 178 kHz, and 100
kHz frequency channels. The dots represent the computed
electric field directions assuming that the wave vector is
near the resonance cone with $\overline{k} \cdot \overline{v}_b > 0$, and the x's repre-
sent measured electric-field directions. The close agree-
ment between the measured and modeled directions indicates
that the whistler-mode radiation is propagating near the
resonance cone in the same direction as the beam.
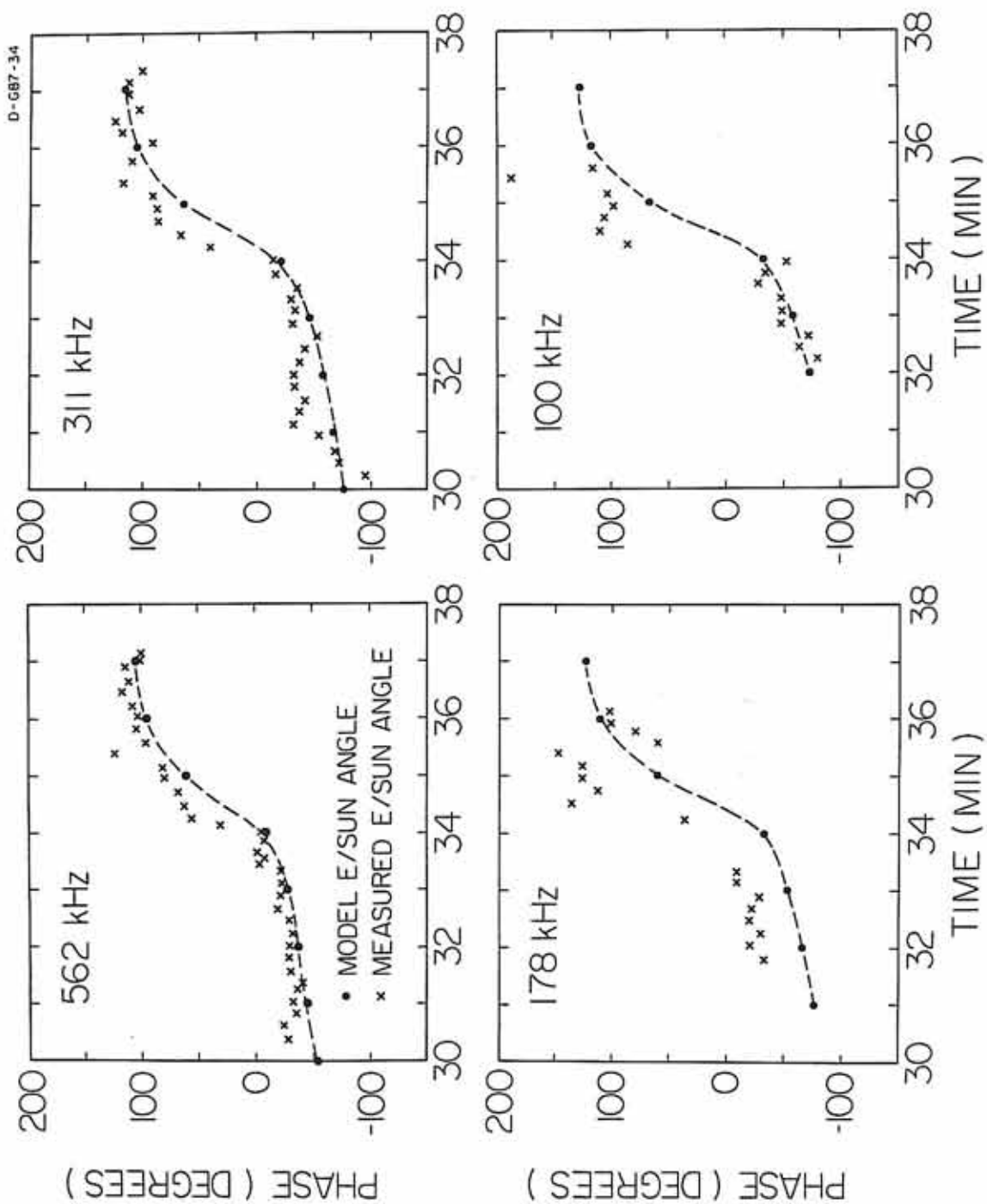
Figure 5   This diagram shows the integration surface used to calculate the power emitted from the beam in the whistler mode. At closest approach, the PDP passed within 3 meters of the beam at a distance of about 200 meters from the shuttle.
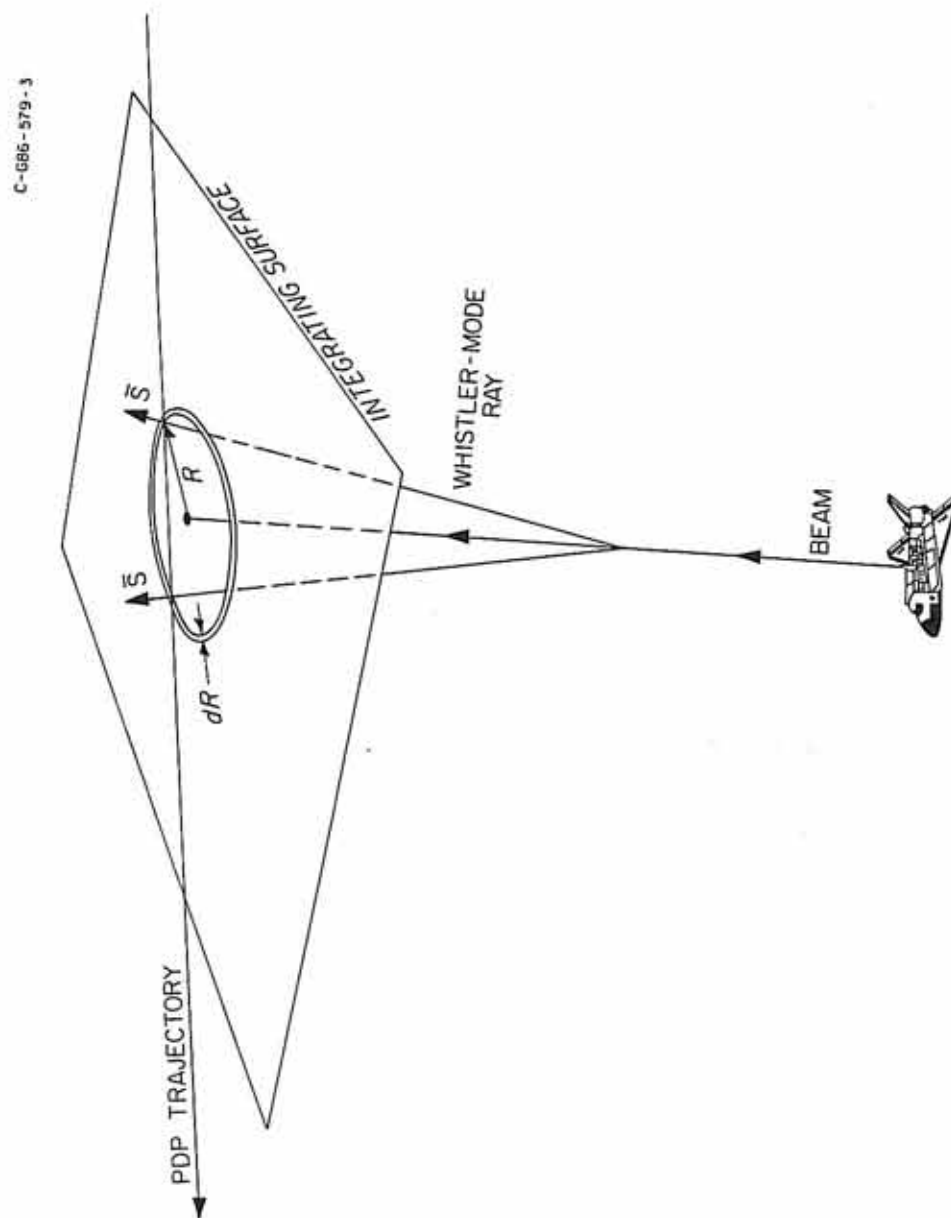
Figure 6   The calculated power spectral density from the beam in the whistler mode is shown as a function of frequency.

MEASURED POWER
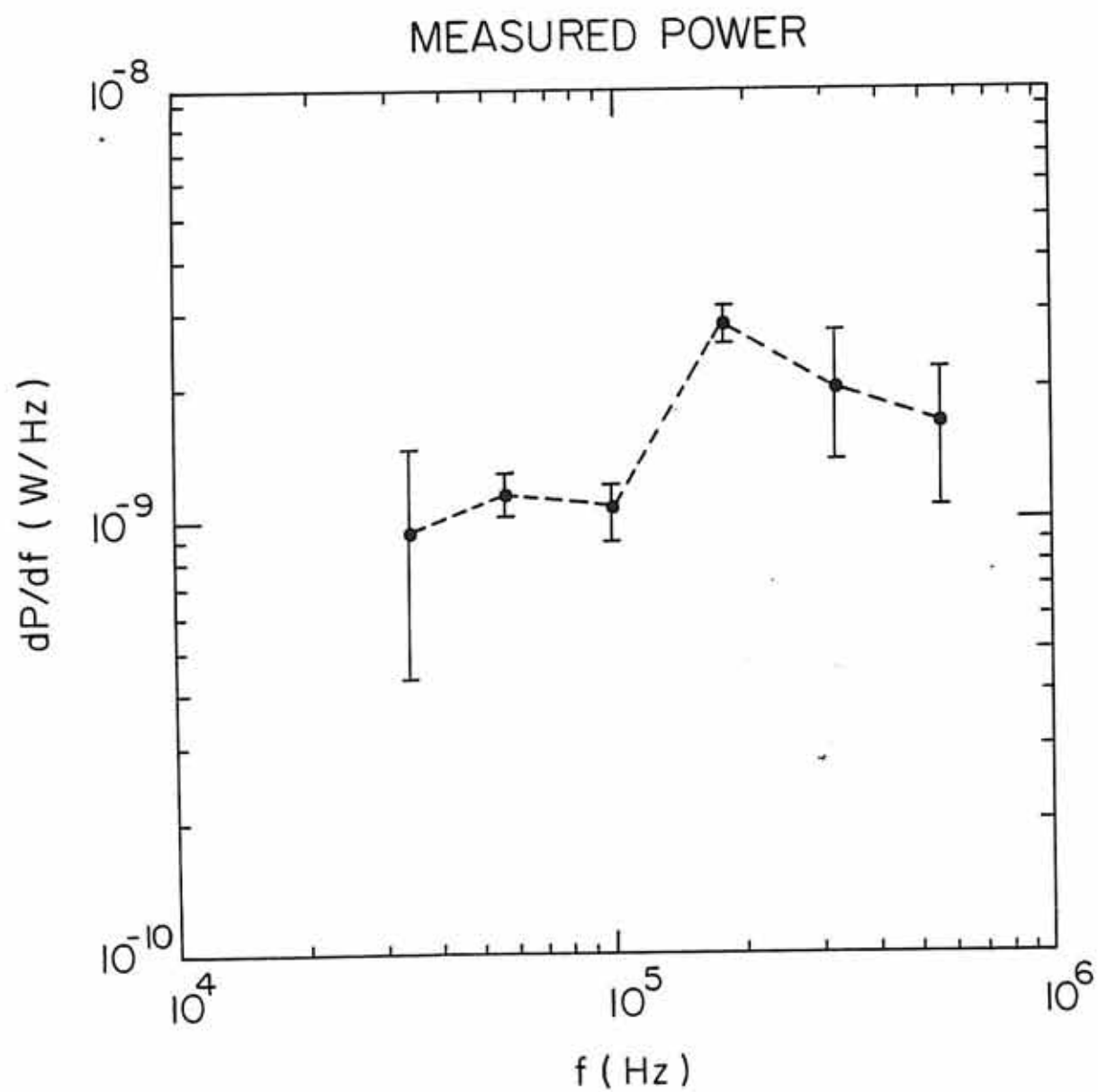
Figure 7(a) and (b)   The linear emissivity, dP/dfdℓ, is shown as a

function of the distance, L, along the beam for the 562

kHz and 311 kHz frequency channels. Note that the

emissivity starts to decrease rapidly beyond about 100

meters.

C-G87-33
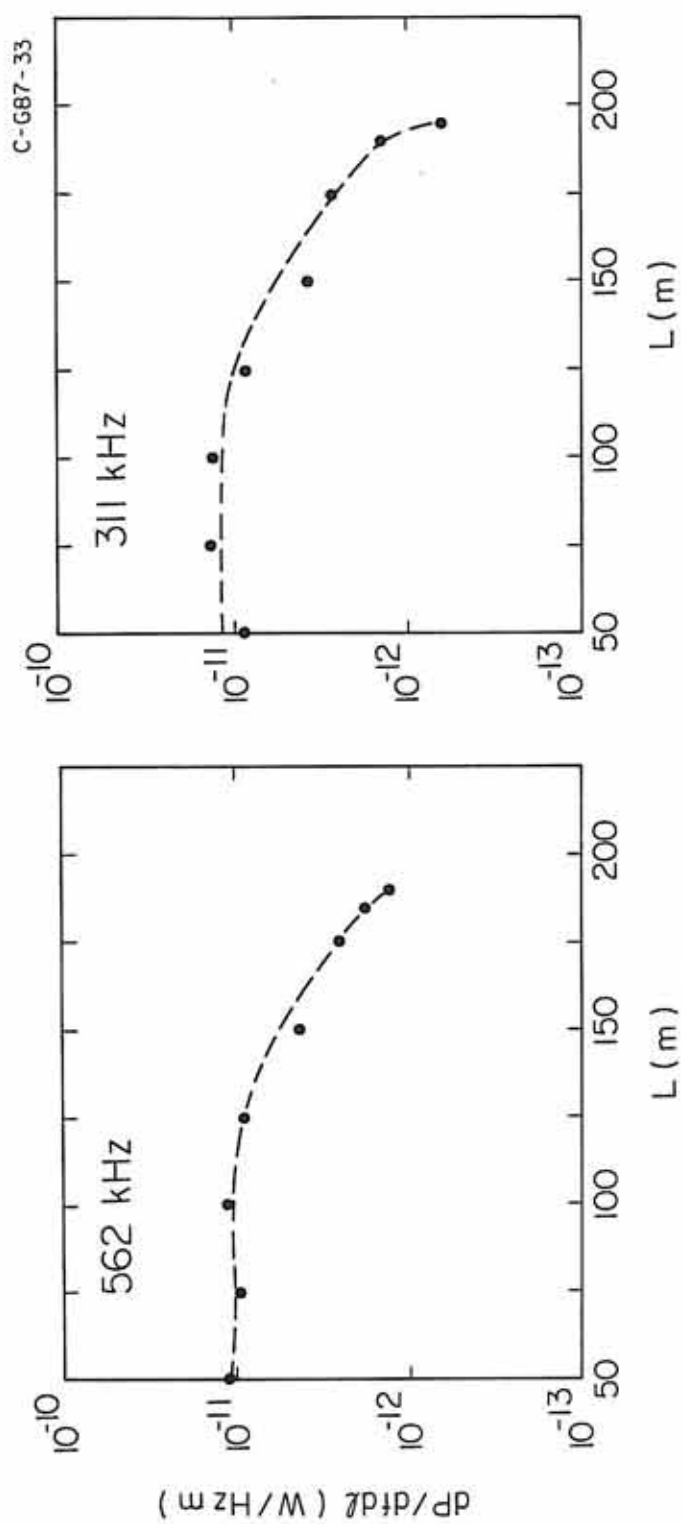
Figure 8   The power spectra from a single electron radiating via the Cerenkov processes is shown in a plasma environment similar to that surrounding the SL-2 beam. These calculations assume the wave/beam interaction is by a Landau resonance process and that the particle pitch angle is 10°. This power calculation is based on formulas derived by Mansfield [1967].

POWER EMITTED BY EACH ELECTRON

C-G86-450-1
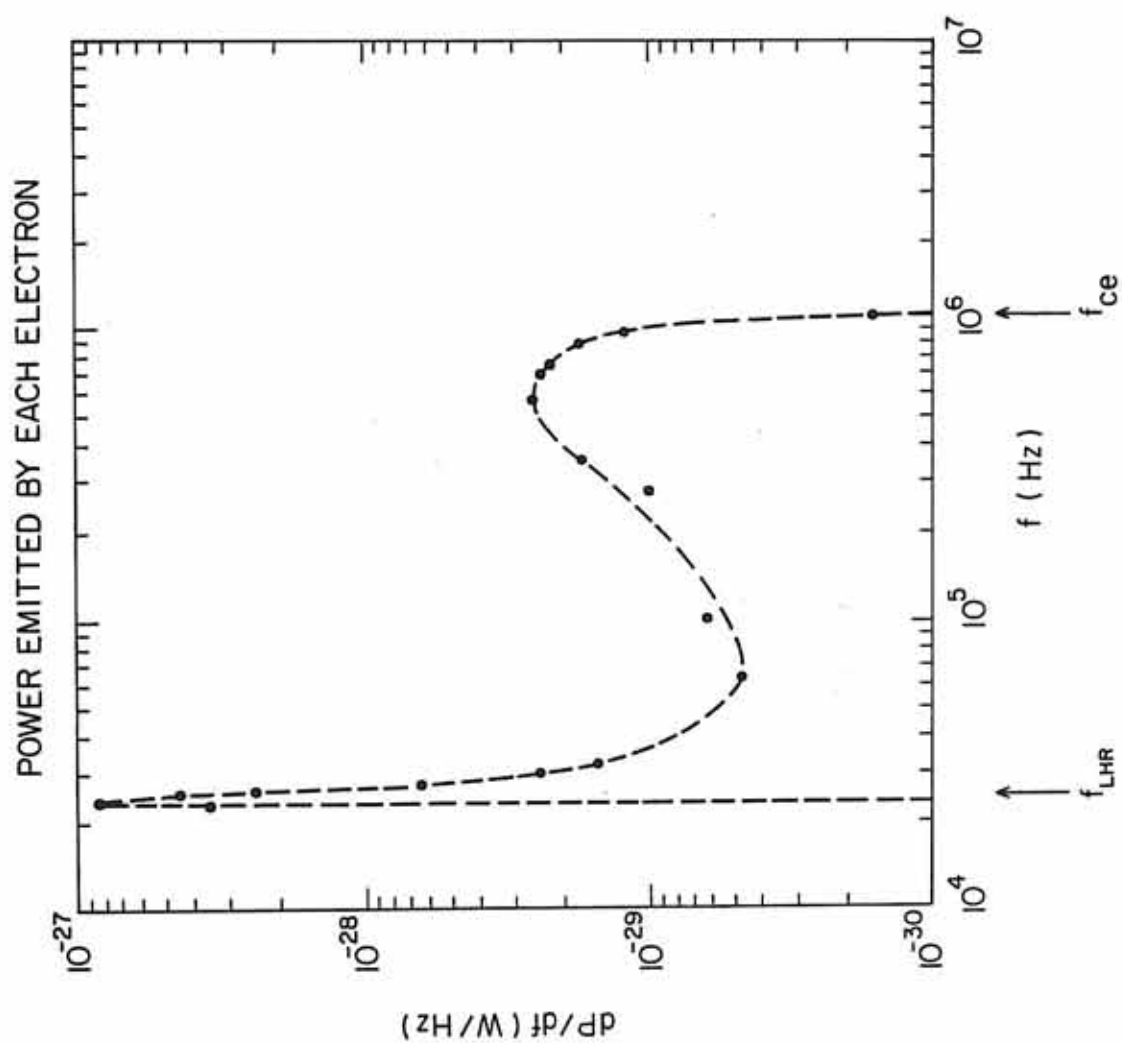
Figure 9   This figure displays the radial expansion of a

field-aligned electron beam after it is initially

ejected from a gun of radius r_0. As the beam

propagates, the radius expands according to

$$r = r_0 + \frac{V_{\perp exp}}{V_b} z.$$

$$\vec{B}_o, \hat{z}$$

$$r = r_o + \frac{V_{\perp exp}}{V_b} Z$$

ELECTRON
BEAM

$$Z = 0$$

$$r_o$$

ELECTRON
GENERATOR
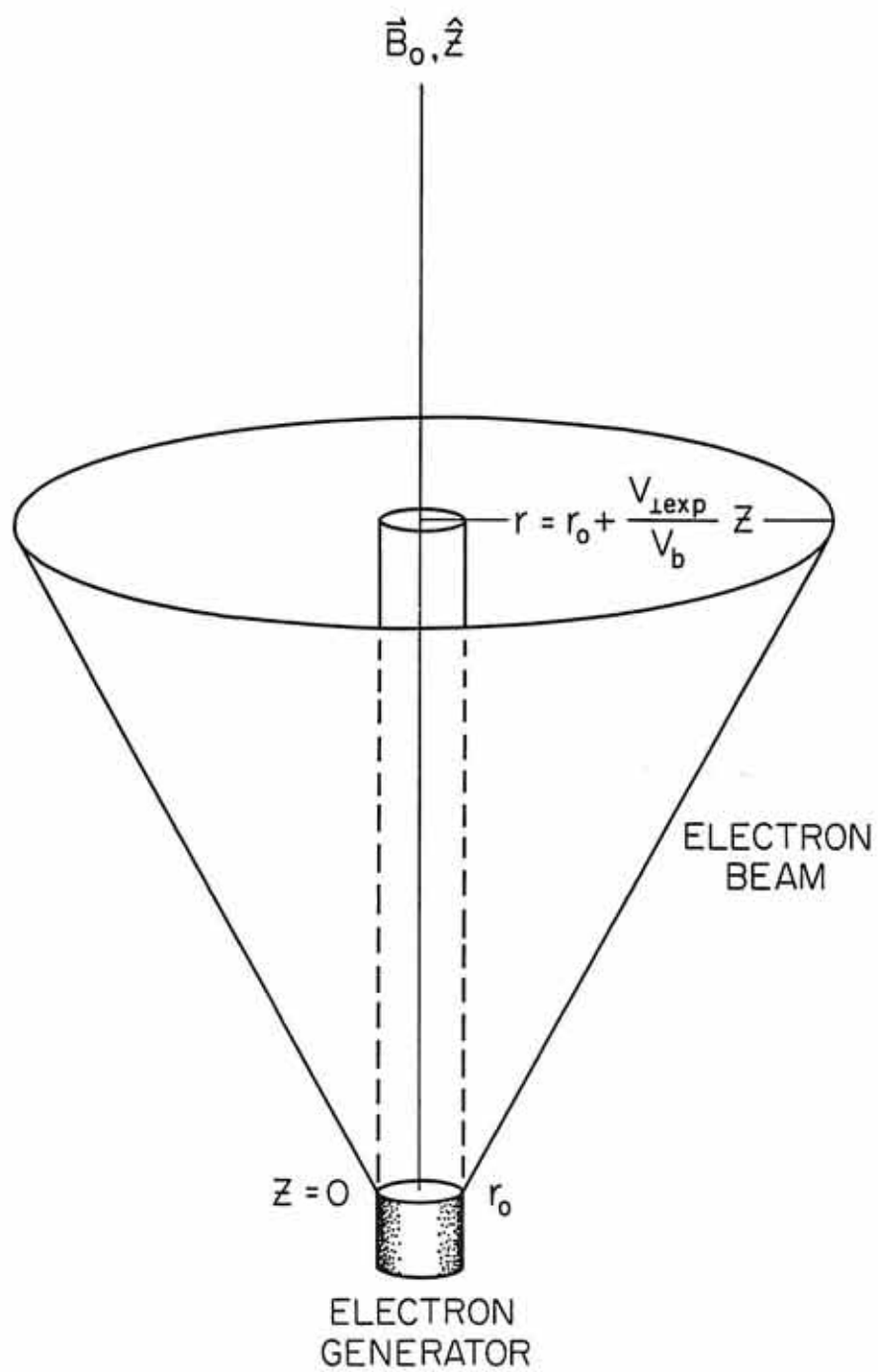
Figure 10   This figure is a V_z versus z phase-space configuration of

electrons from a beam of density $n_b = 1/16\ n_A$ and $V_b = 10$

V_{th} after (a) 32 ω_{pe}^{-1} and (b) 64 ω_{pe}^{-1}. This

configuration is obtained from Pritchett and Winglee's

two-dimensional simulation [1986]. The beam is injected

from a spacecraft located at z = 125.
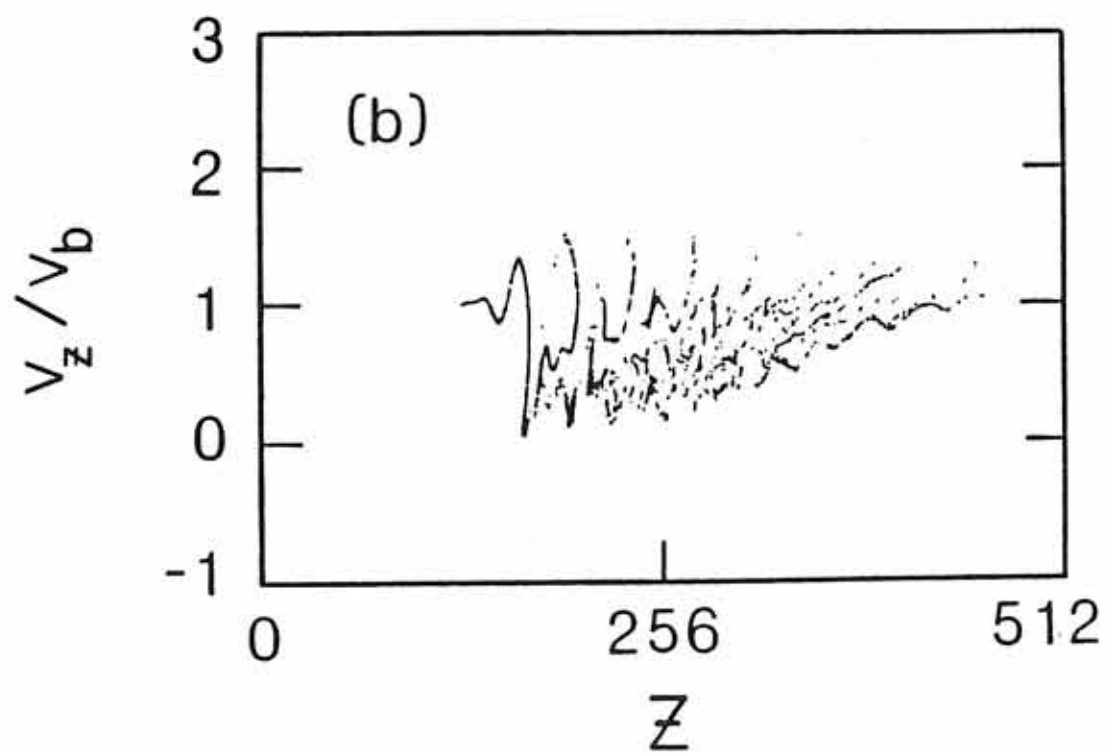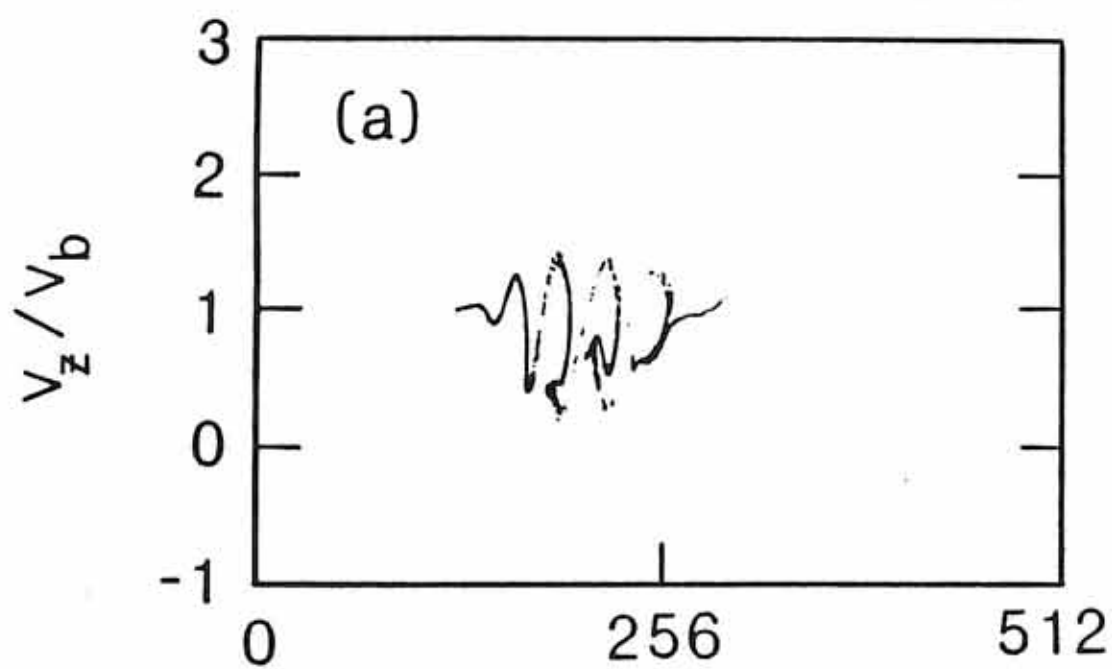
Figure 11   This figure is a V_z versus z phase-space configuration of

an electron beam with similar density and velocity as

that of Figure 10 taken from the one-dimensional

simulation developed in this study.   Note that L = 100.

A- G87 -124

(a)

(b)

Z
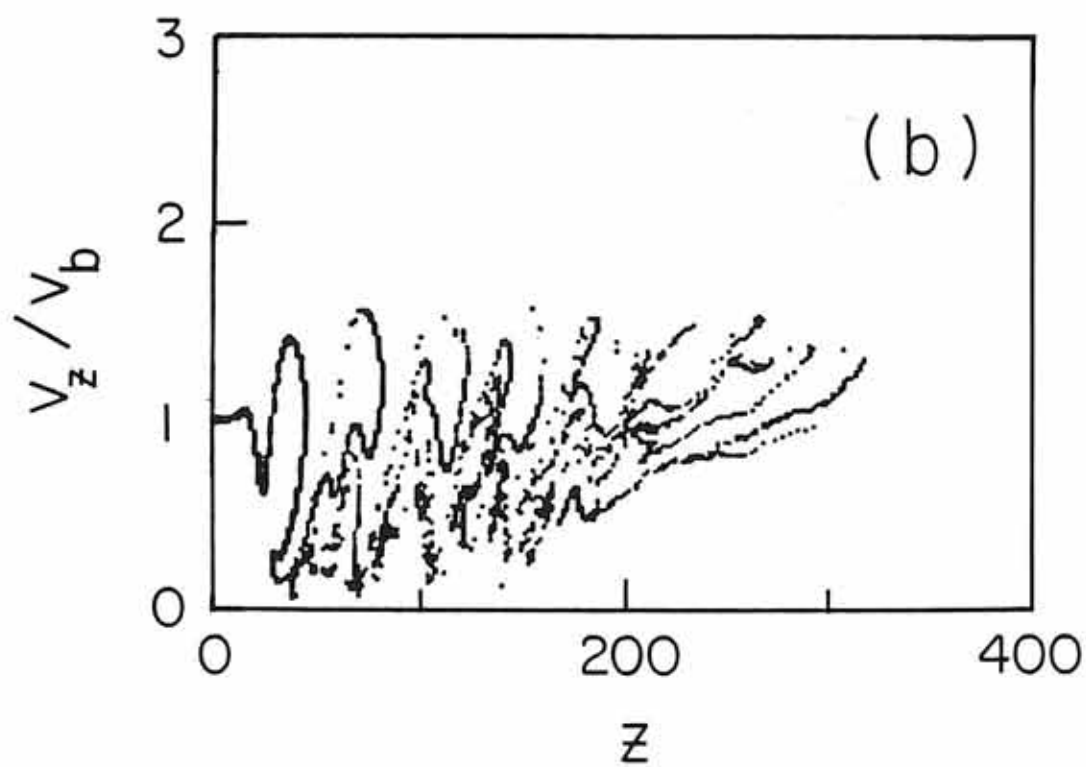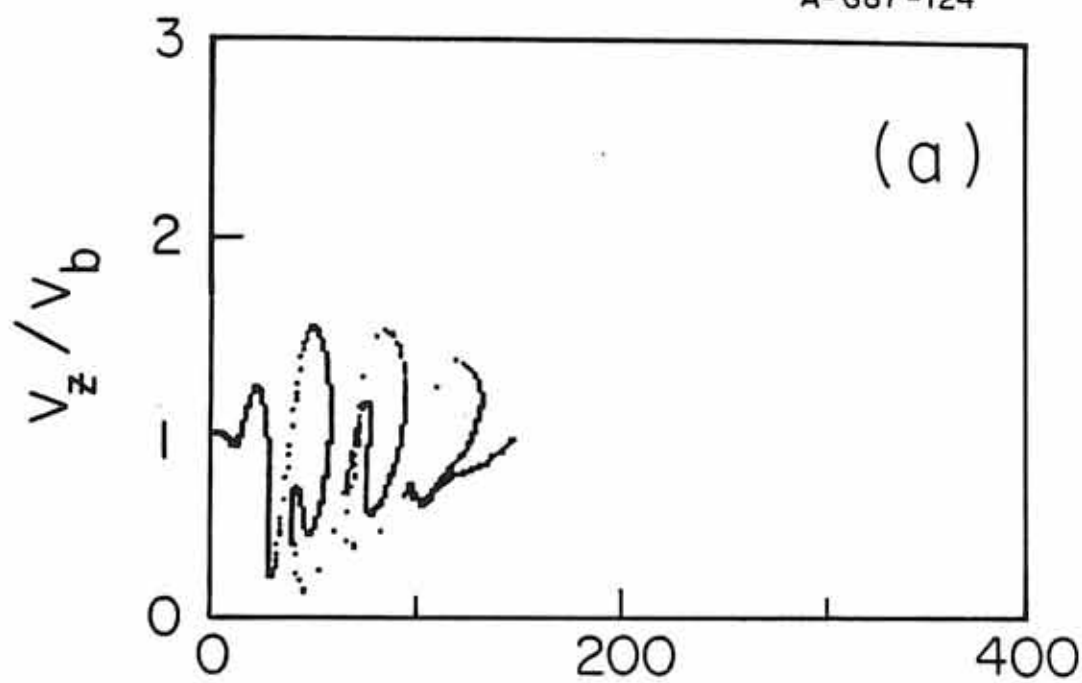
Figure 12 Again, a beam phase-space configuration is shown from the
one-dimensional simulation developed in this study run
with similar parameter as those of Figures 10 and 11, only
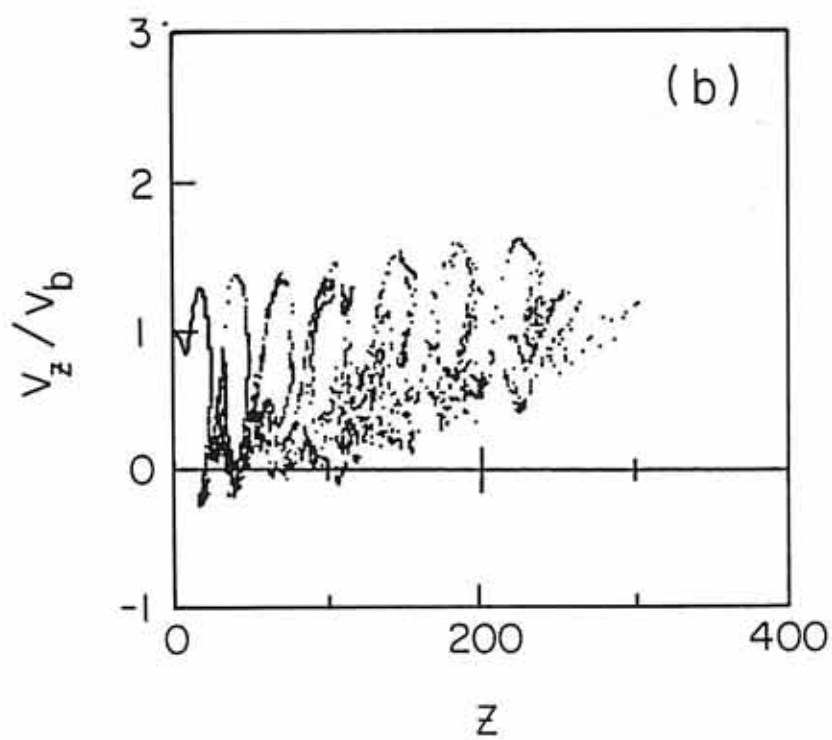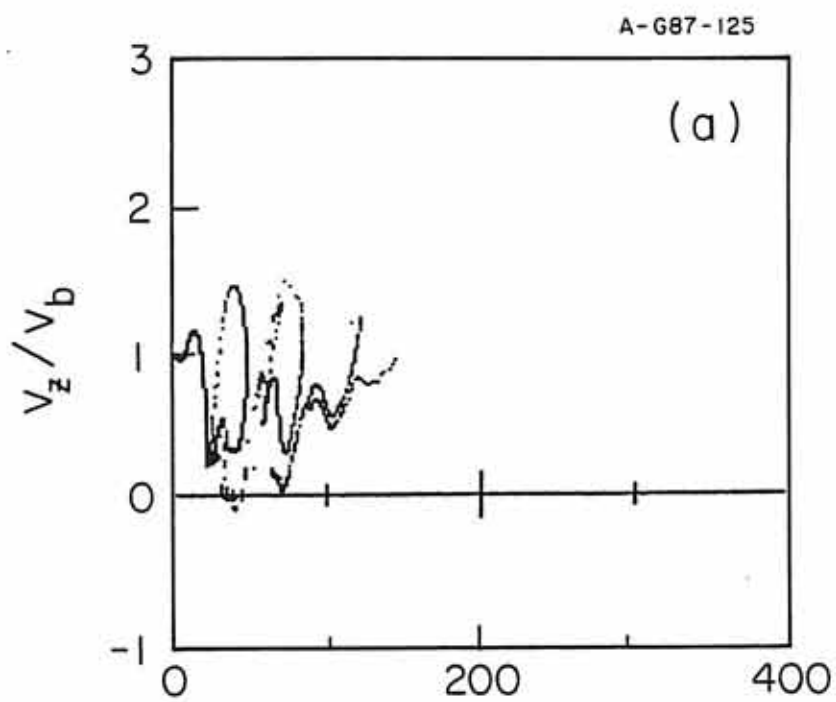now $L = \infty$ (no radial beam expansion).

Figure 13   This V_z versus z beam phase-space configuration is from

the one-dimensional simulation run with $n_b = 8\ n_A$, $V_b = 15$

V_{TH} and $L = 10$ for two different times: (a) $20\ \omega_{pe}^{-1}$
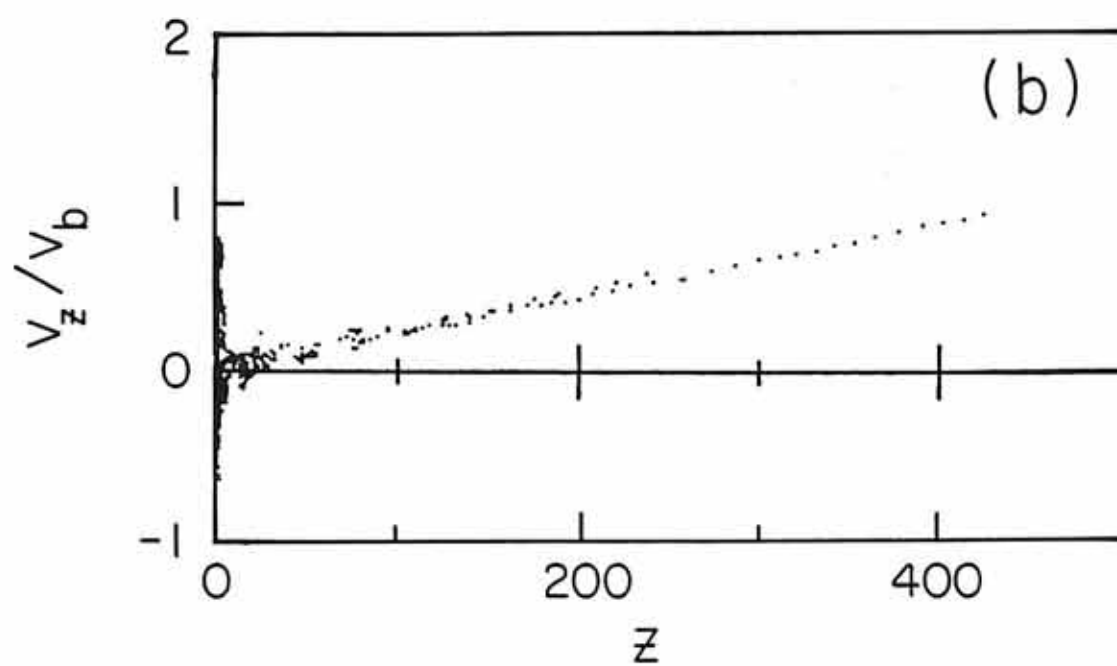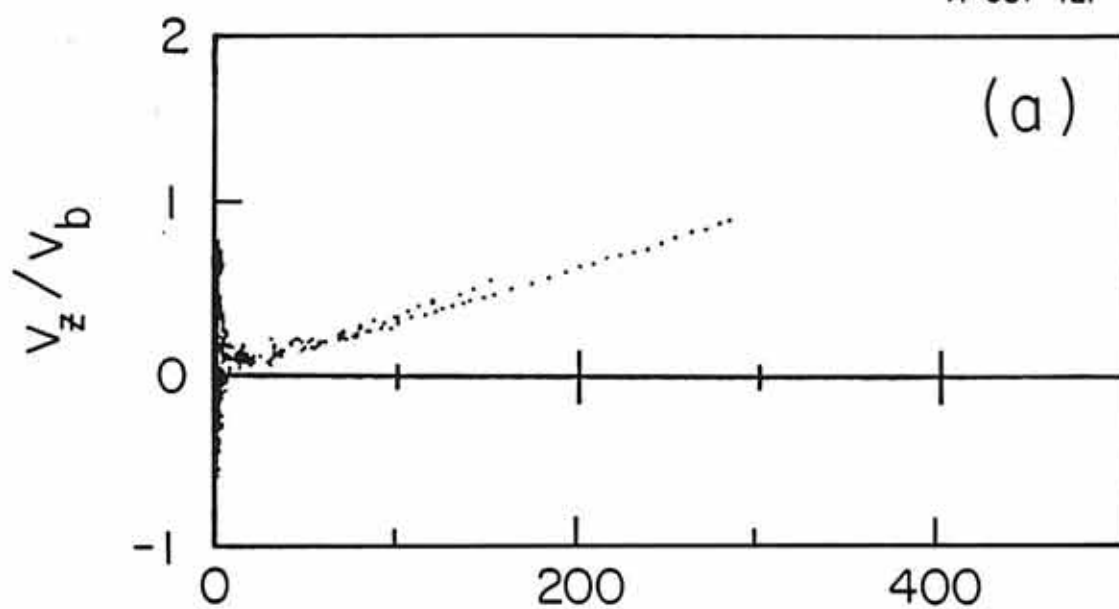
and (b) $30\ \omega_{pe}^{-1}$.

A-G87-121

Figure 14   This figure is a beam phase-space configuration

taken from Winglee and Pritchett [1986] for an overdense

beam (n_b/n_A = 2). Note that the beam structure looks
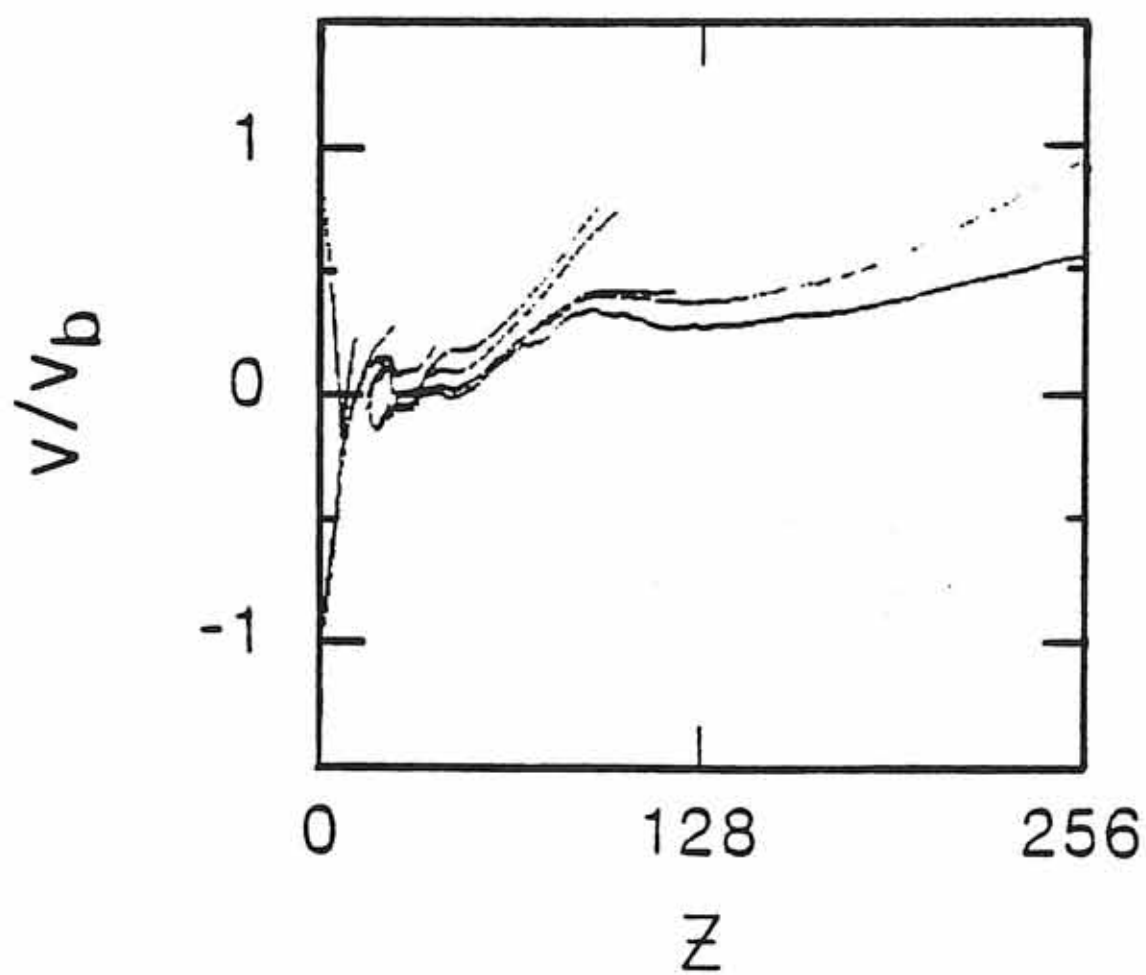
similar to that of Figure 13.

A-G87-150

Figure 15   This figure is a beam phase-space configuration

taken from Pritchett and Winglee [1986] for an overdense

beam (n_b = 8 n_A) at two different times: (a) 16 ω_{pb}^{-1} and
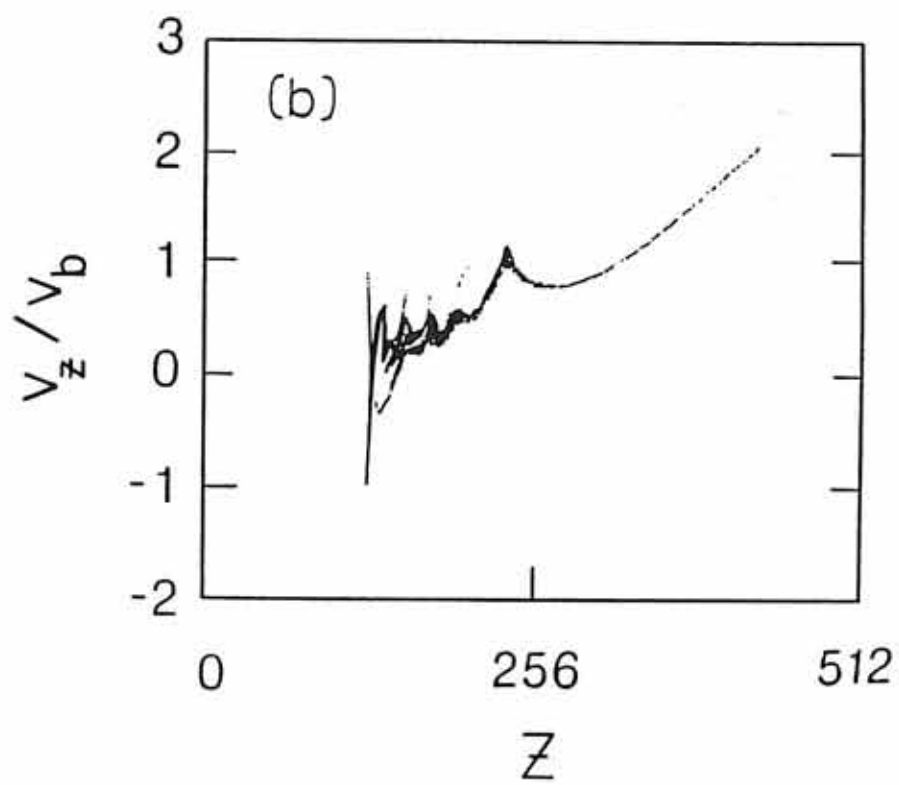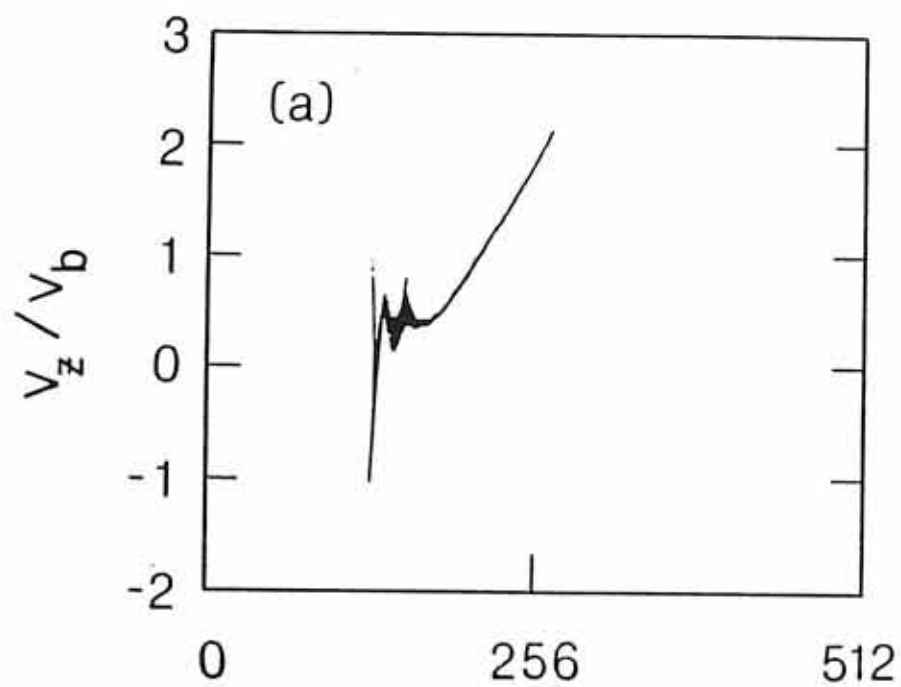
(b) 32 ω_{pb}^{-1}.

A - G87 - 151 - 1

Figure 16   This figure is a V_z versus z phase-space configuration of the modeled SL-2 electron beam obtained from the one-dimensional simulation run with the parameters shown in Table 1, with L = 10.

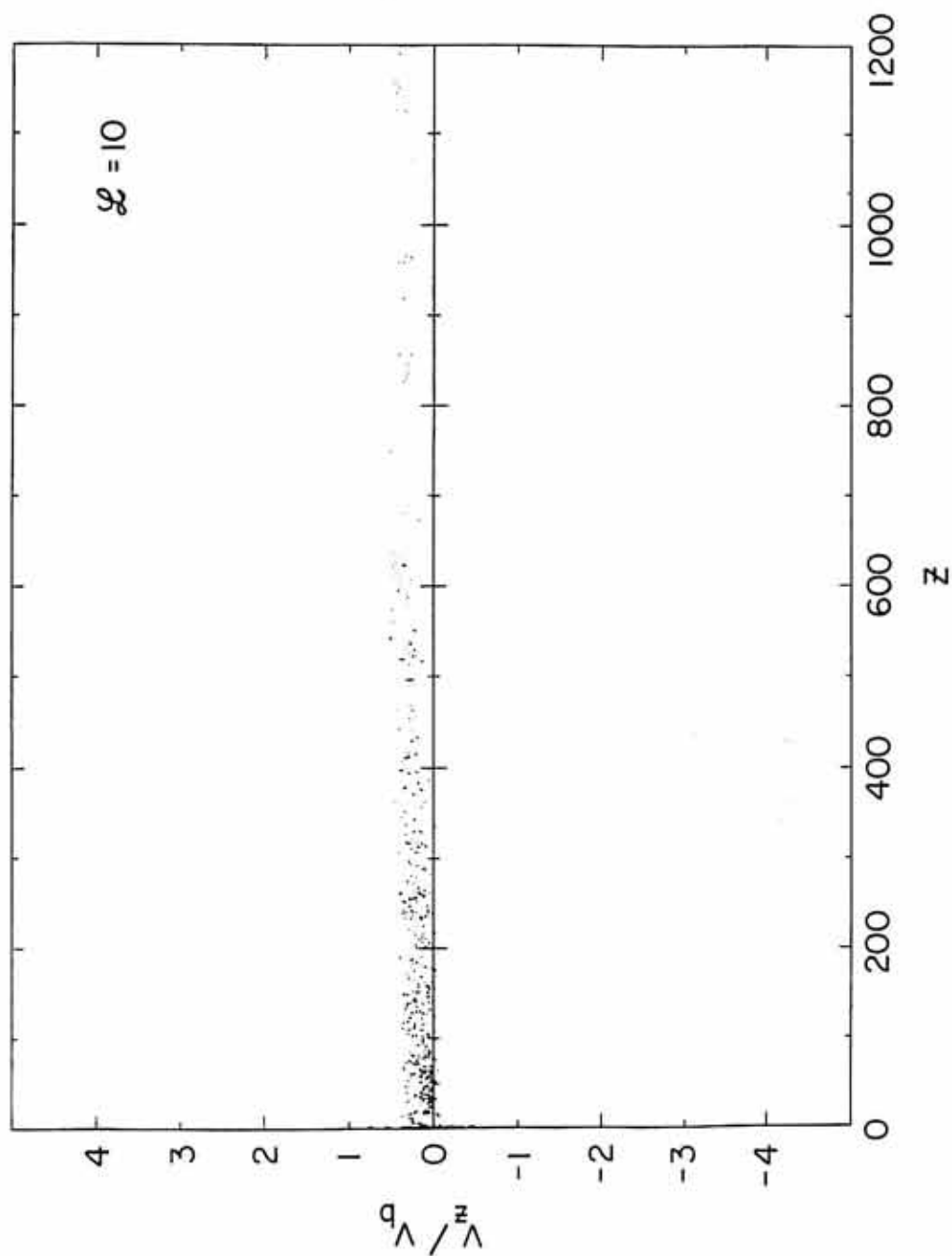BEAM PARTICLES AT $t = 270 \ \omega_{pe}^{-1}$

$\mathscr{L} = 10$

Figure 17   This figure displays E_z versus z from the one-dimensional

simulation run with L = 10. Note that a strong electric

field is located near z = 0.

E - FIELD MAGNITUDE AT $t = 270 \, \omega_{pe}^{-1}$

$\mathcal{L} = 10$

A-G87-137

Figure 18   This figure displays the number of electrons, N, versus z

from the modeled beam run with L = 10.

BEAM ELECTRONS AT t = 270 ω$_{pe}^{-1}$

A-G87-138

$\mathscr{L}$ = 10

Figure 19   This figure is a V_z versus z phase-space configuration of

the modeled SL-2 electron beam obtained from the

one-dimensional simulation run with the parameters shown

in Table 1, with L = 5.

BEAM PARTICLES AT t = 270 ω_{pe}^{-1}

A-G87-133-3

$\mathscr{L} = 5$

V_z / V_b

z

Figure 20   This figure displays E_z versus z from the one-dimensional

simulation run with L = 5.   Note that a strong electric
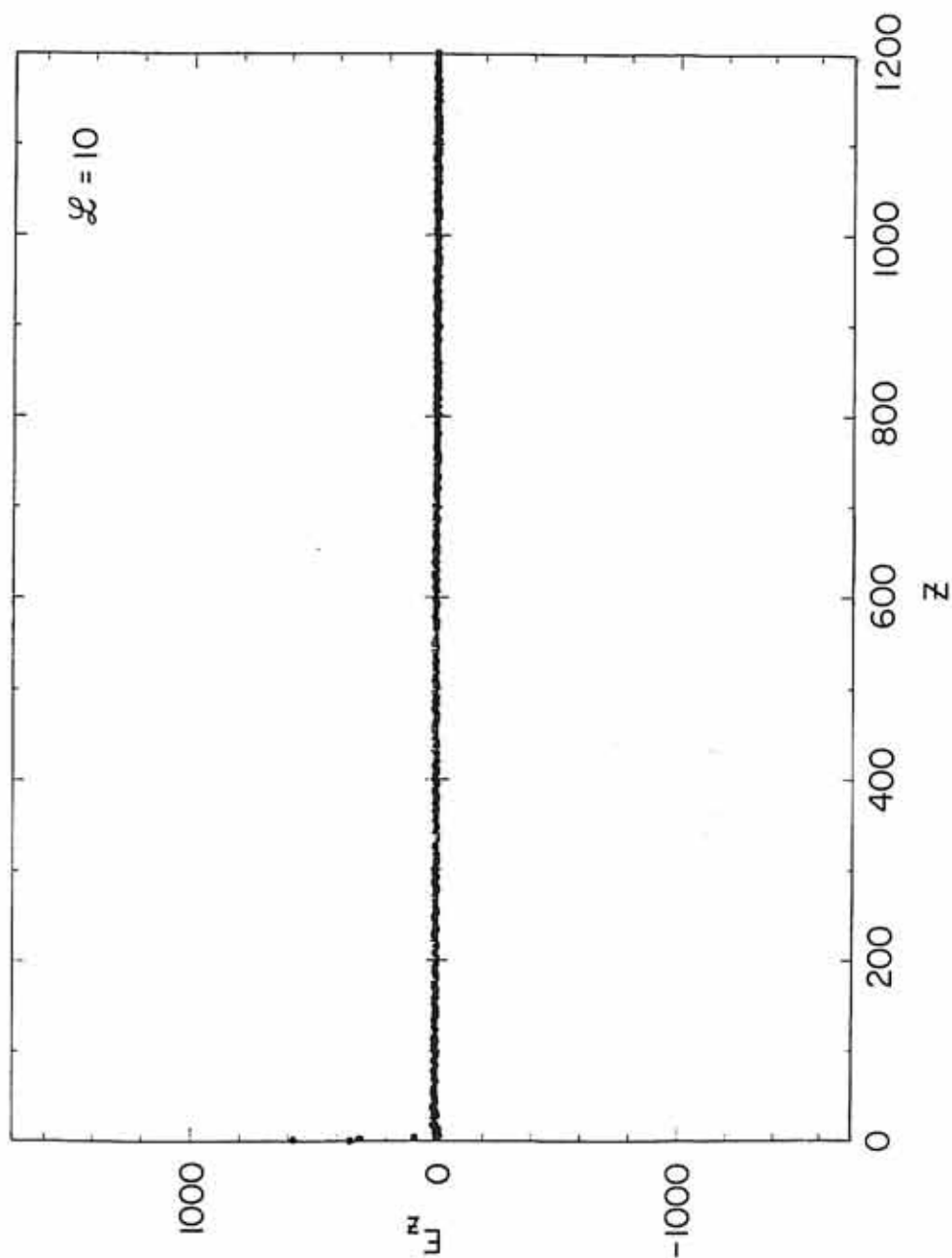
field is located near z = 0.

A-G87-I34-I

E - FIELD MAGNITUDE AT $t = 270 \, \omega_{pe}^{-1}$

$\mathscr{L} = 5$

Figure 21   This figure displays the number of electrons, N, versus z

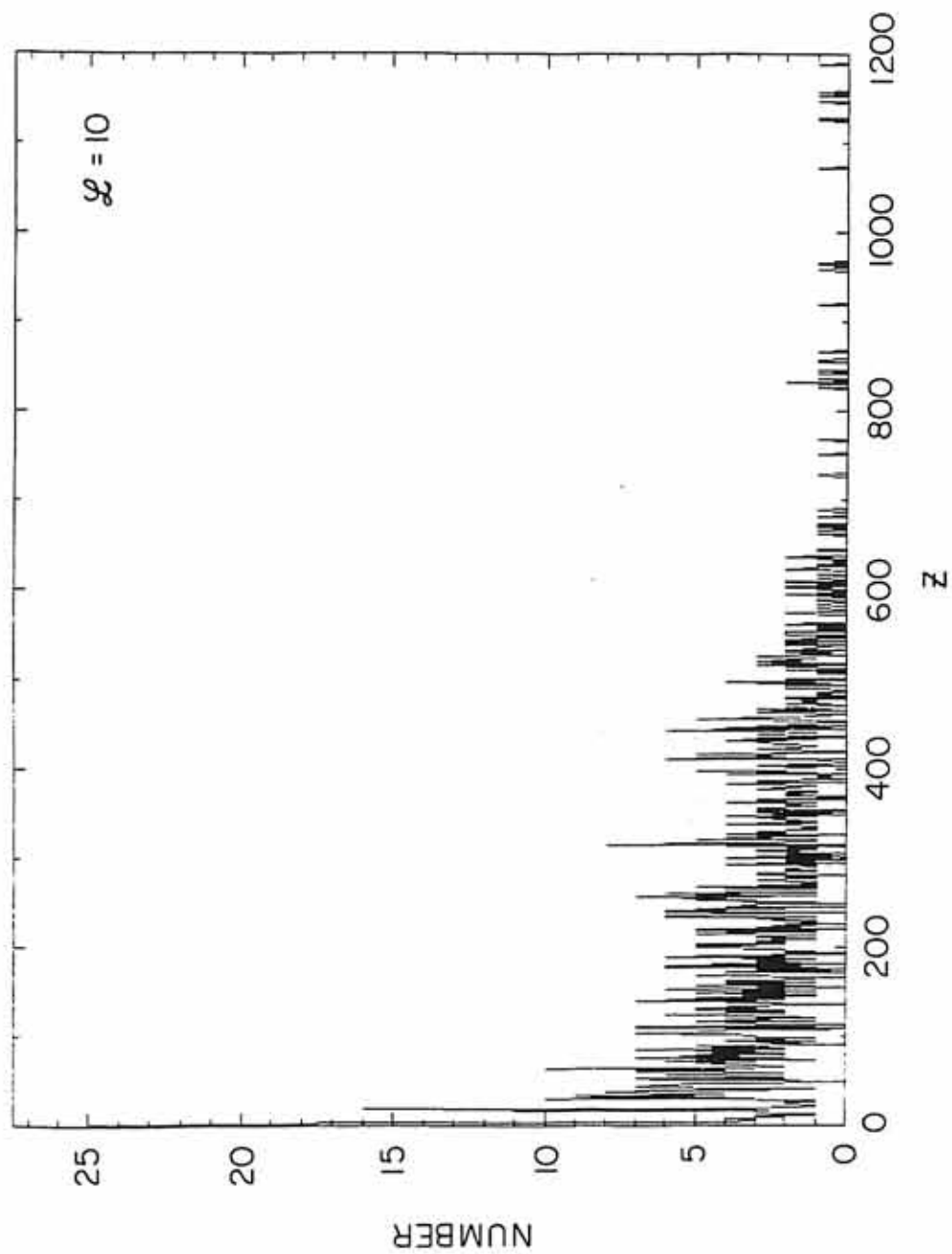from the modeled beam run with L = 5.

BEAM ELECTRONS AT t = 270 ω_{pe}^{-1}

A-G87-135

$\mathscr{L} = 5$
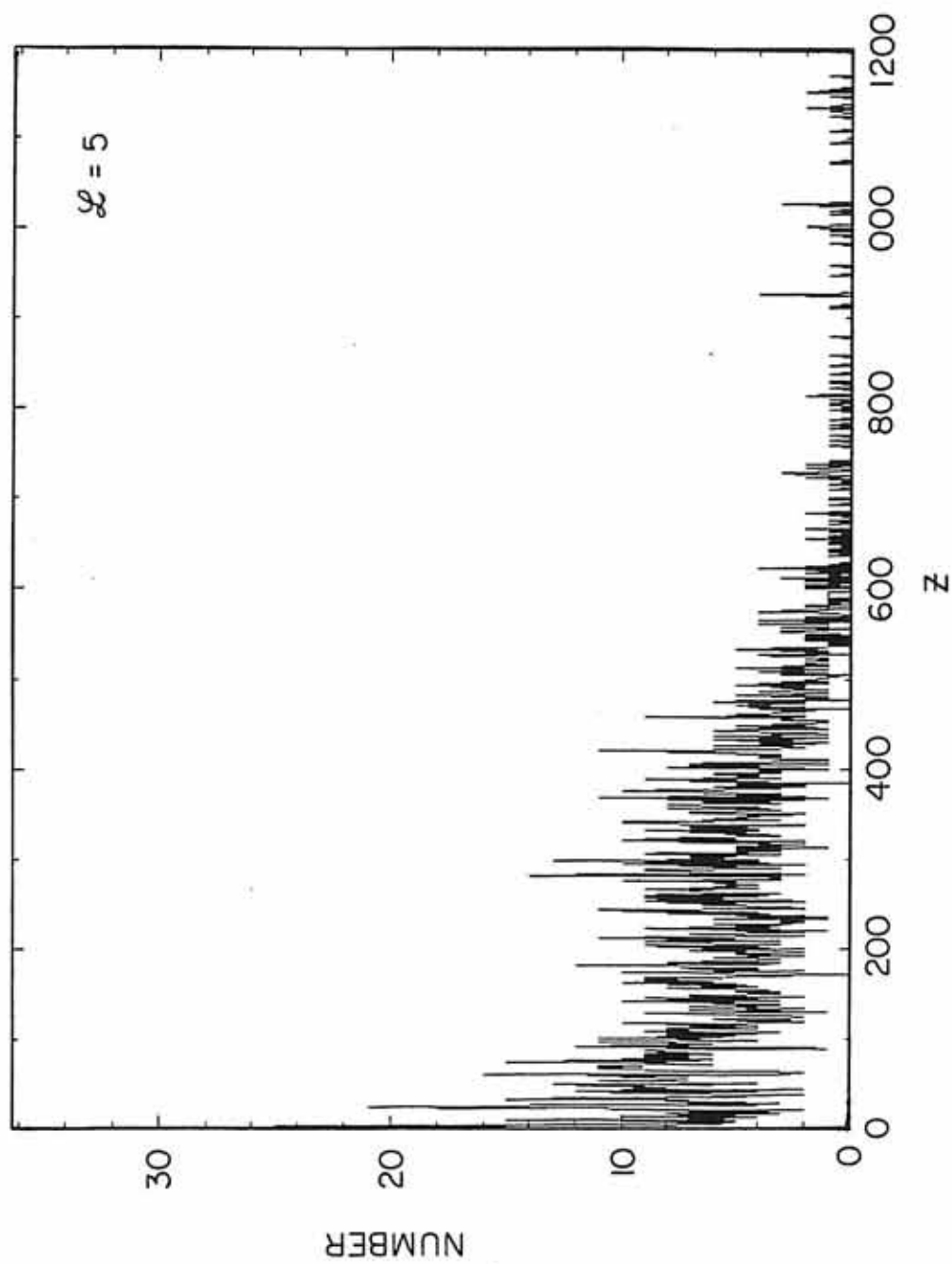
Figure 22   This figure is a V_z versus z phase-space configuration of

the modeled SL-2 electron beam obtained from the

one-dimensional simulation run with the parameters shown

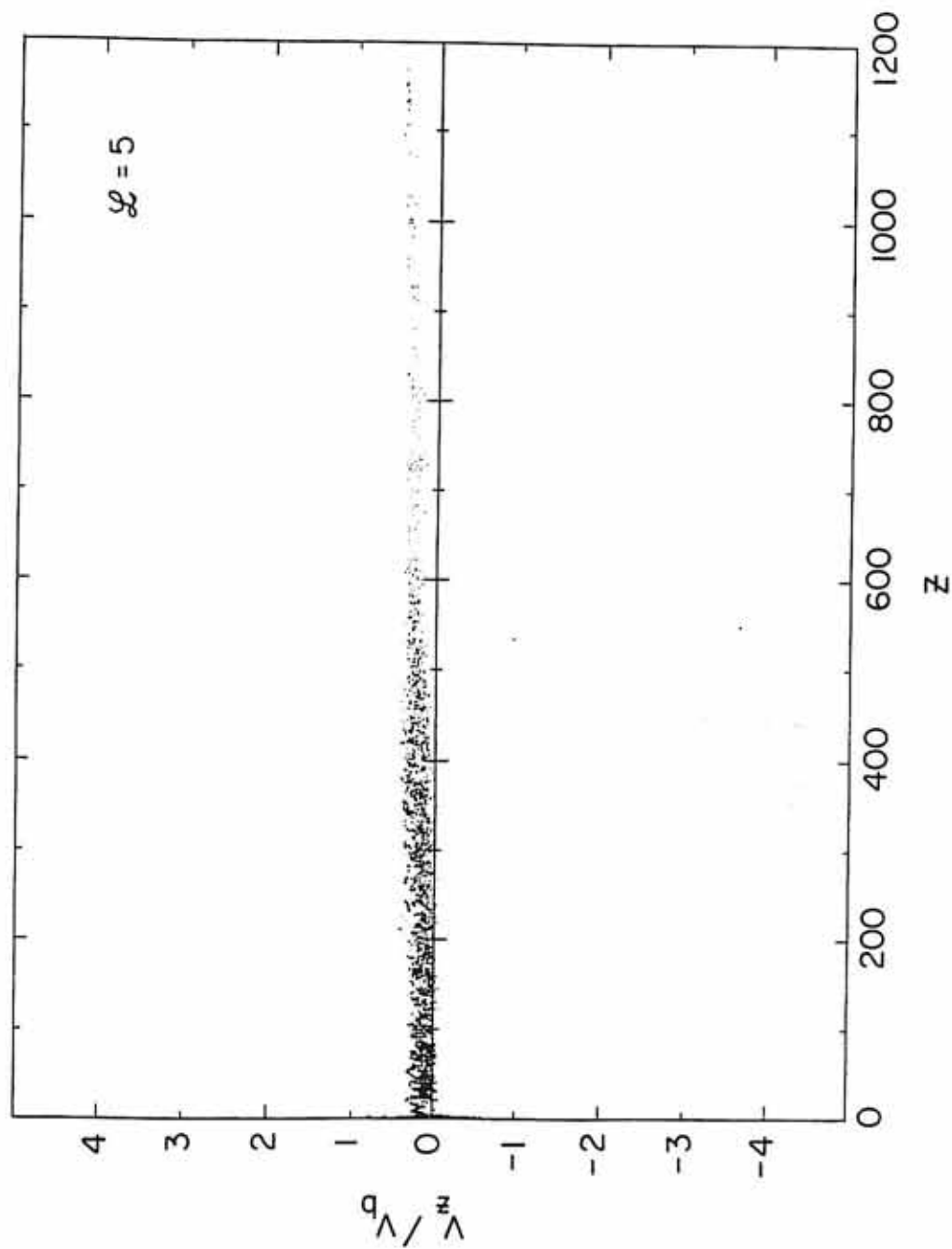in Table 1, with L = 3.

BEAM PARTICLES AT t = 270 ω_{pe}^{-1}

A-G87-130

$\mathscr{L} = 3$

Figure 23   This figure displays E_z versus z from the one-dimensional
simulation run with L = 3.   Note that wave activity is
present in the beam.

E - FIELD MAGNITUDE AT t = 270 ω_{pe}^{-1}

A - G87 - 131

$\mathscr{L} = 3$
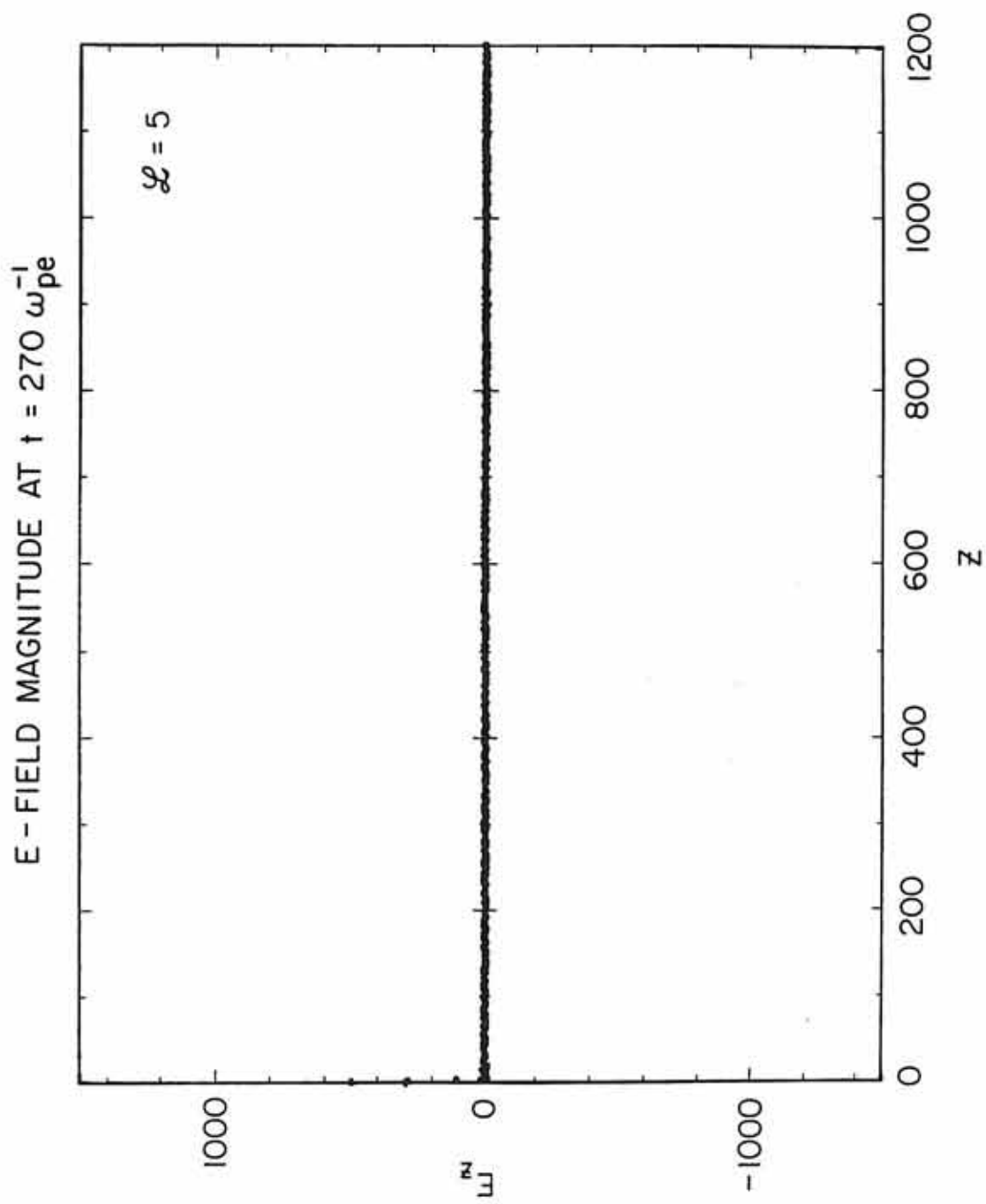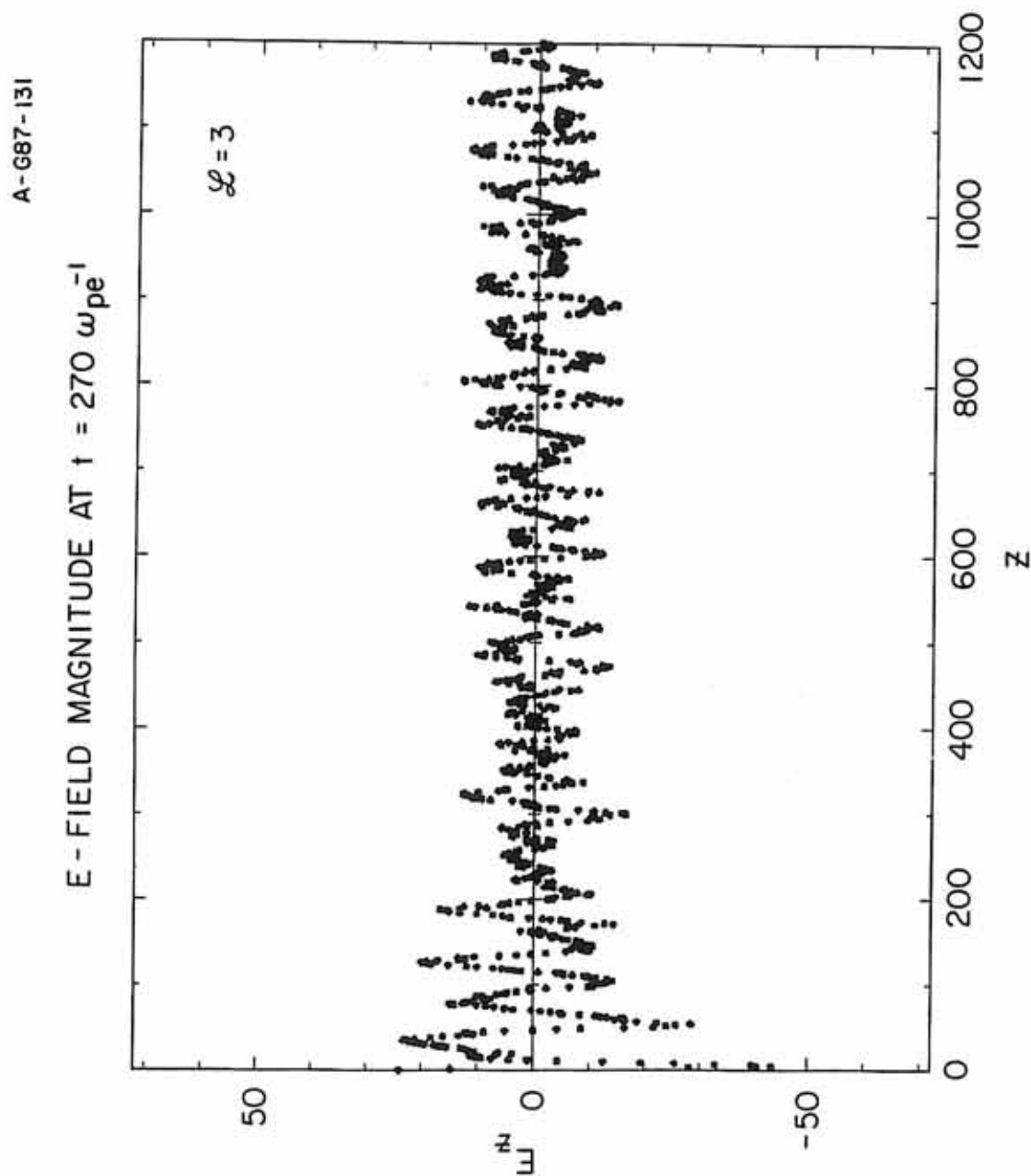
Figure 24   This figure displays the number of electrons, N, versus z

from the modeled beam run with L = 3.

BEAM ELECTRONS AT t = 270 ω_{pe}^{-1}

A-G87-132

$\mathcal{L} = 3$

Figure 25   This figure is a V_z versus z phase-space configuration of

the modeled SL-2 electron beam obtained from the

one-dimensional simulation run with the parameters shown

in Table 1, with L = 2.

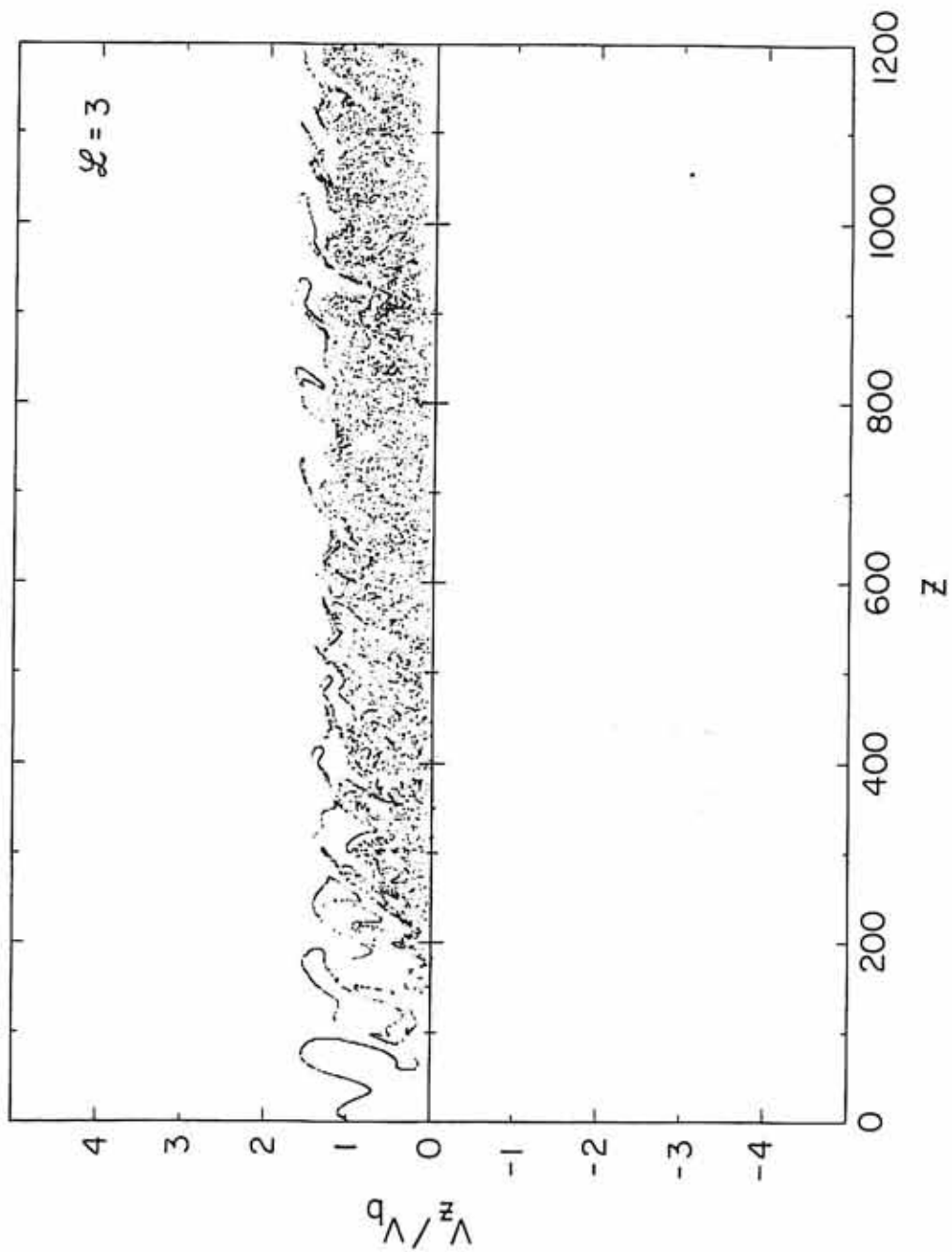BEAM PARTICLES AT t = 270 ω_{pe}^{-1}

$\mathscr{L} = 2$

A-G87-127
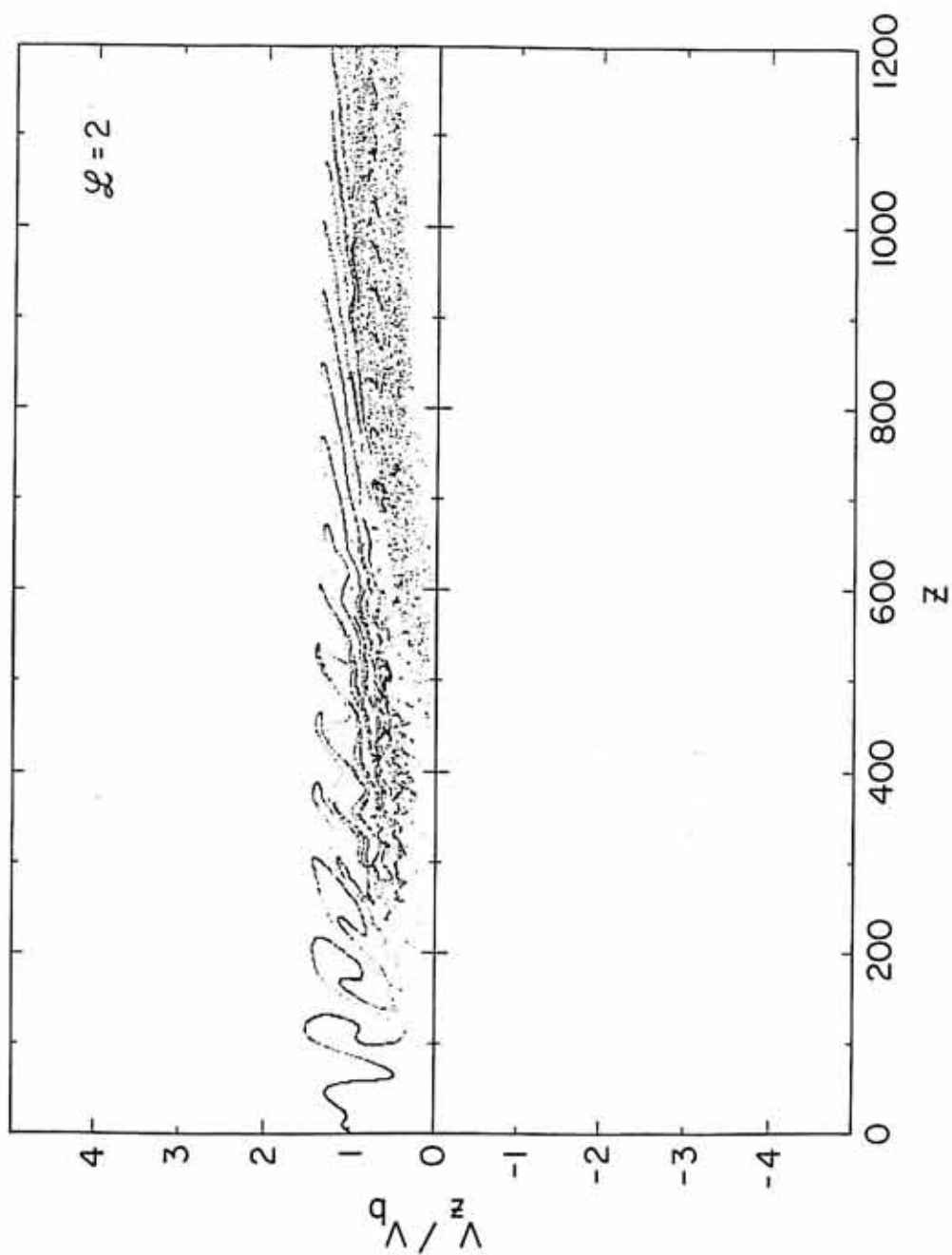
Figure 26   This figure displays E_z versus z from the one-dimensional
            simulation run with L = 2.   Note that wave activity is
            present in the beam.

E - FIELD MAGNITUDE AT $t = 270 \ \omega_{pe}^{-1}$

A-G87-128

$\mathcal{L} = 2$
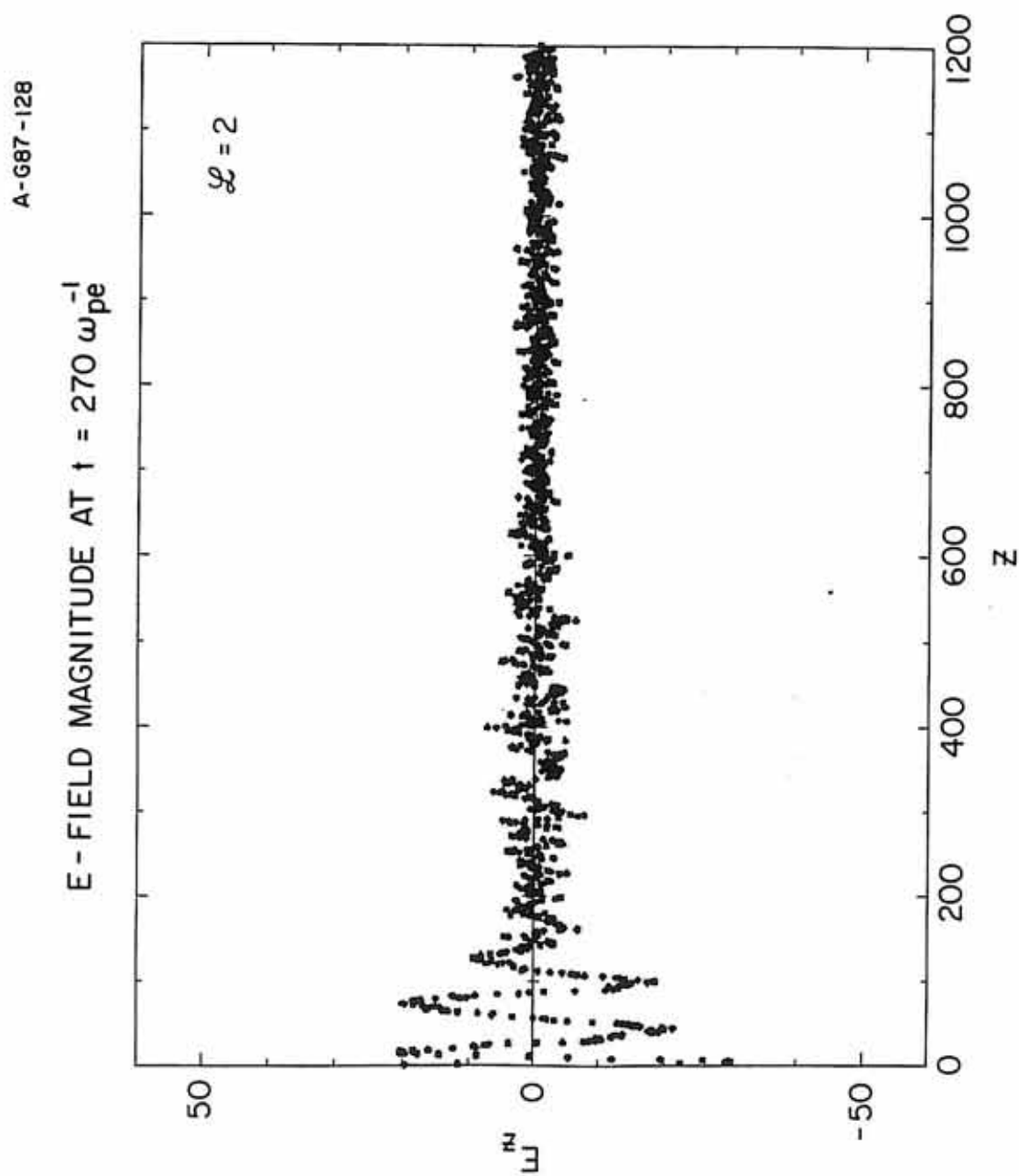
Figure 27   This figure displays the number of electrons, N, versus z

from the modeled beam run with L = 2.

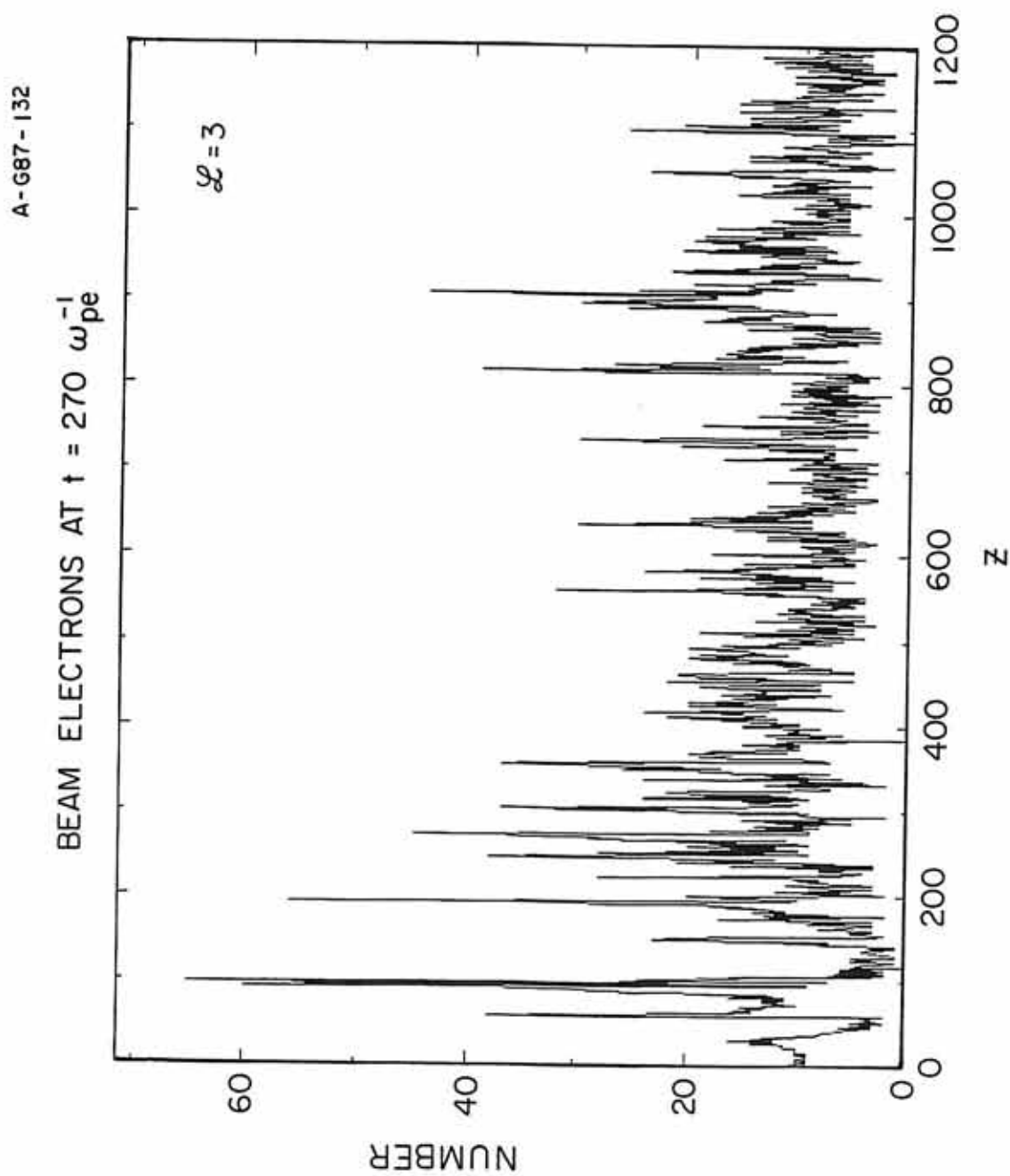BEAM ELECTRONS AT t = 270 ω_{pe}^{-1}

$\mathscr{L} = 2$

A-G87-129
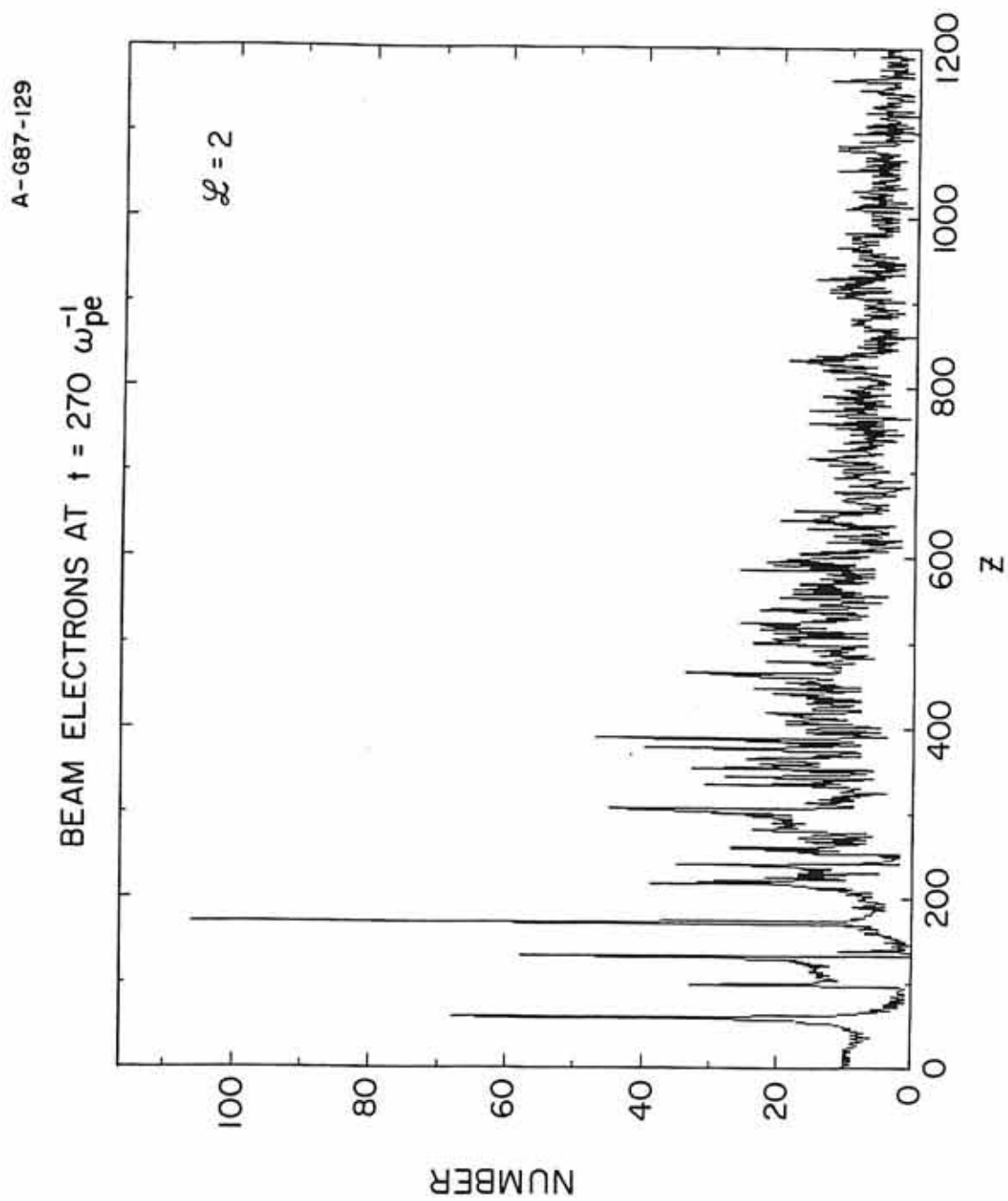
Figure 28   This figure is a V_z versus z phase-space configuration

of the modeled SL-2 electron beam obtained from the

one-dimensional simulation run with L = 3 and a length

of 3600 grids corresponding to 180 meters. Note that

the beam phase-space configuration is similar to that

shown in Figure 22 for a 60-meter beam segment.

BEAM PARTICLES AT $t = 840 \ \omega_{pe}^{-1}$
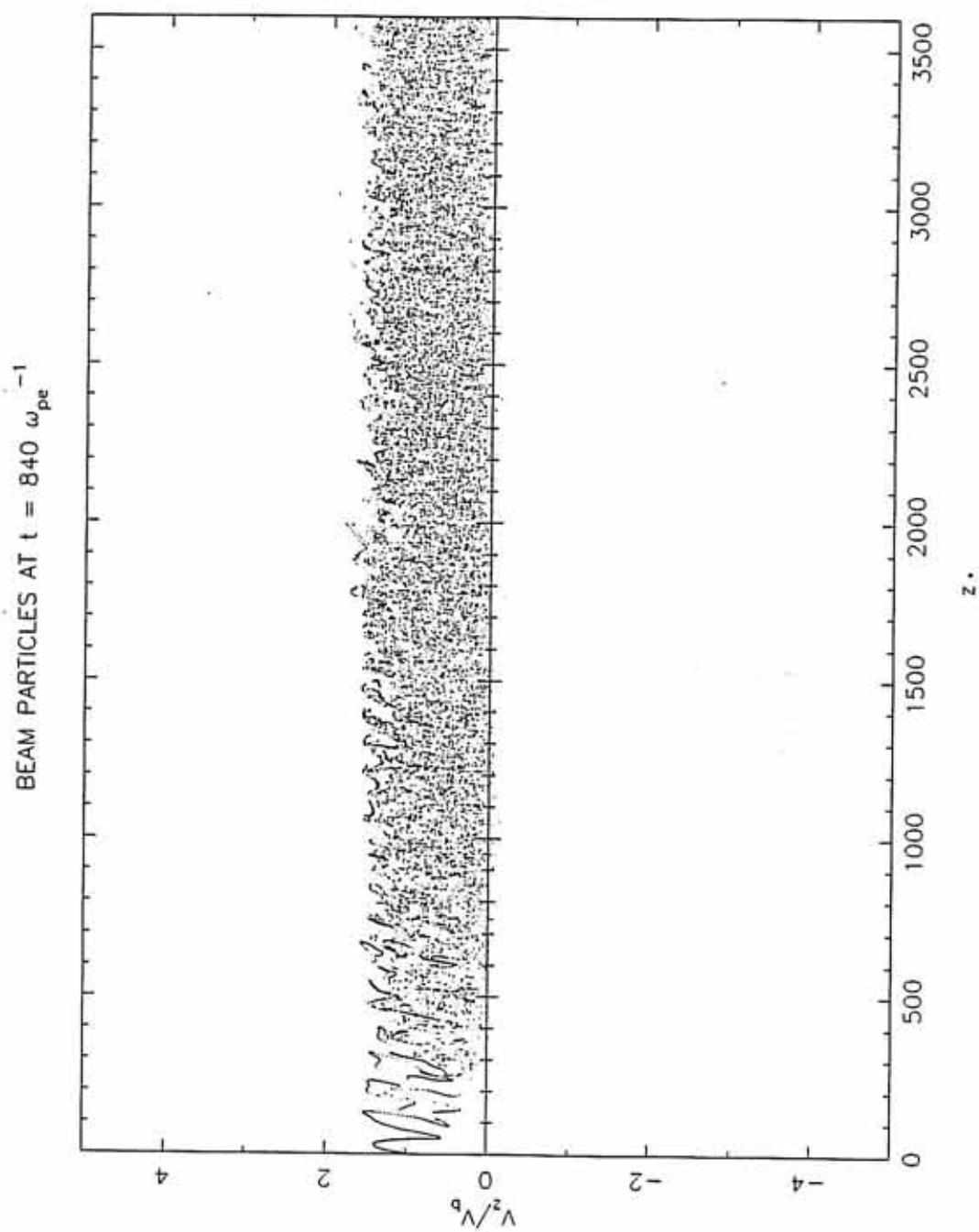
Figure 29   This diagram is a plot of $J_z(k_z,\omega)$ as a function of ω

and k_z for the 175-meter beam segment. The largest

values of $J_z(k_z,\omega)$ are completely dark, while o's and

.'s represent continually lower intensities. Note

that the values of $J_z(k_z,\omega)$ peaks at about $\omega/k_z = 2.8$

$\times\ 10^7$ m/s.
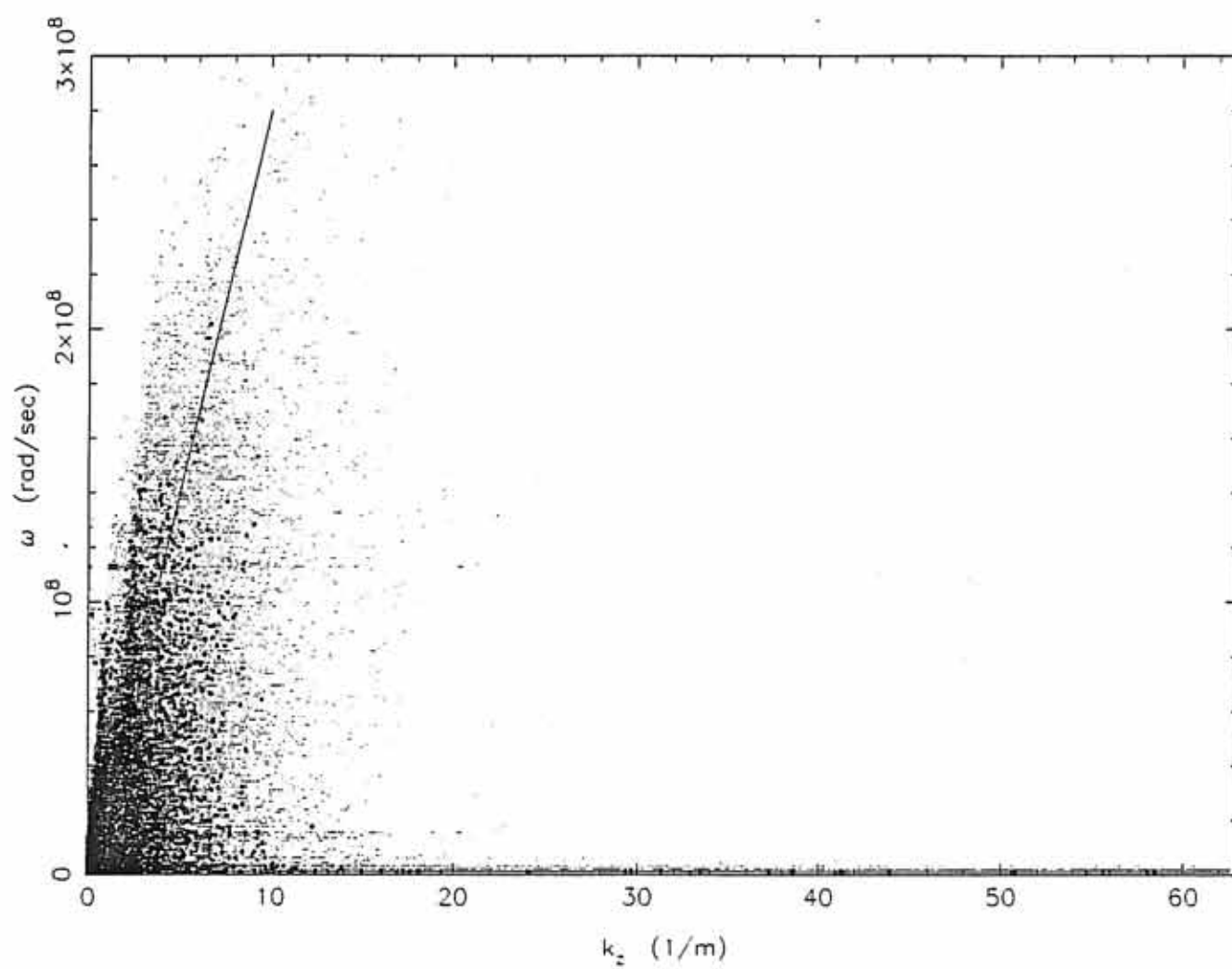
Figure 30   This figure shows the variation of $J_z(k_z)$ for the 175 meter beam segment as a function of k_z. Note for k_z < 22 that $J_z(k_z)$ increases as k_z decreases. This variation in $J_z(k_z)$ results from the density perturbations in the beam created by a beam-plasma instability. Also shown in the figure is the simulation noise level. This noise is obtained since simulation electrons many times the mass and charge of real electrons were used in the computer model. The range of k_z' of the whistler-mode waves is also shown in the figure.
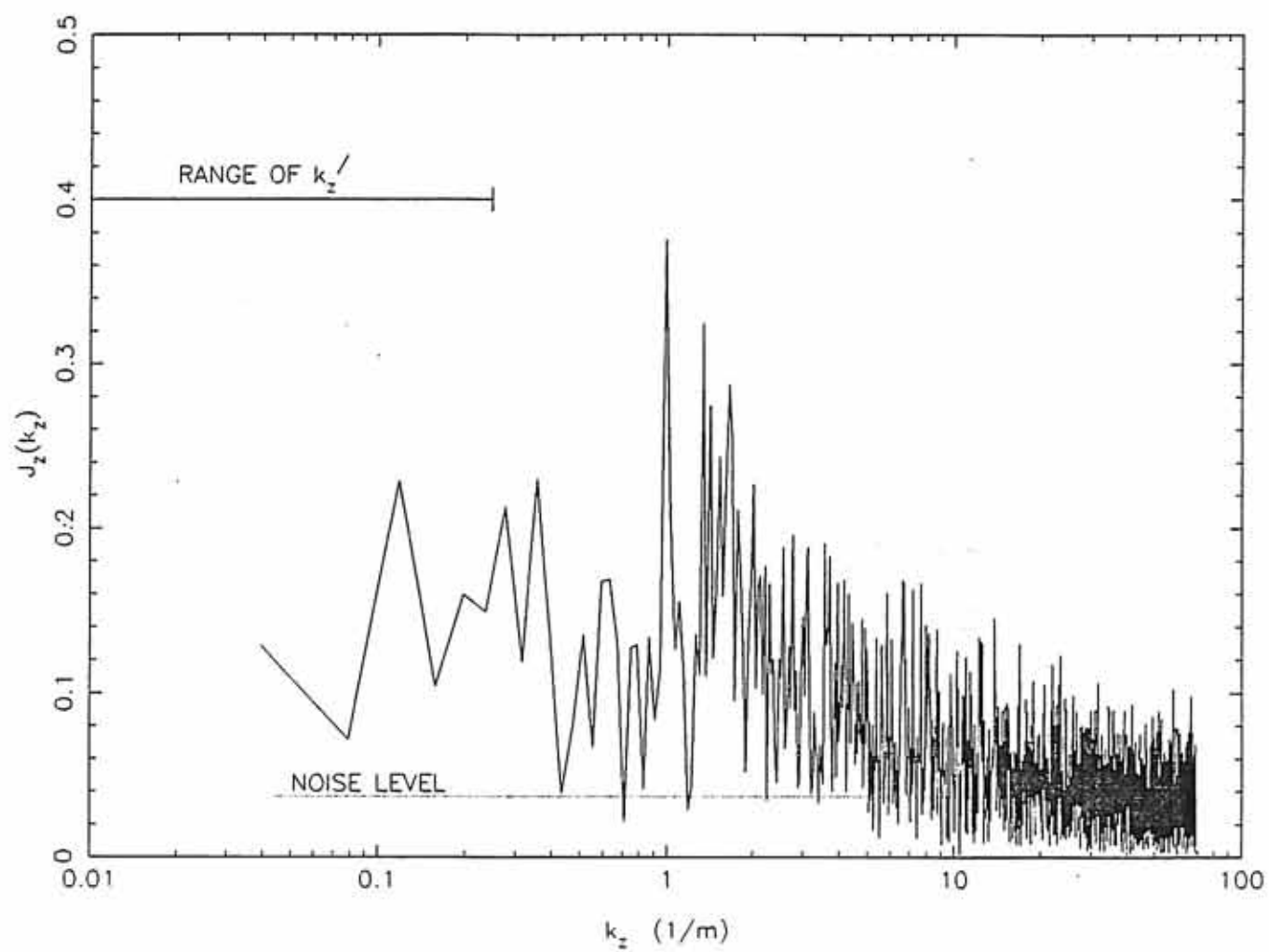
Figure 31   This figure shows the power spectra of the measured

whistler-mode radiation from the first 200 meters of

the SL-2 electron beam along with the calculated

power spectra of the incoherent and coherent Cerenkov

radiation from a 200-meter beam segment.   Note that

the inclusion of coherent radiation effects increases

the calculated powers to those measured from the SL-2

electron beam.   Based on these results, it is

concluded that coherent Cerenkov radiation from a

bunched electron beam generates the detected

whistler-mode radiation.

FREQUENCY (Hz)
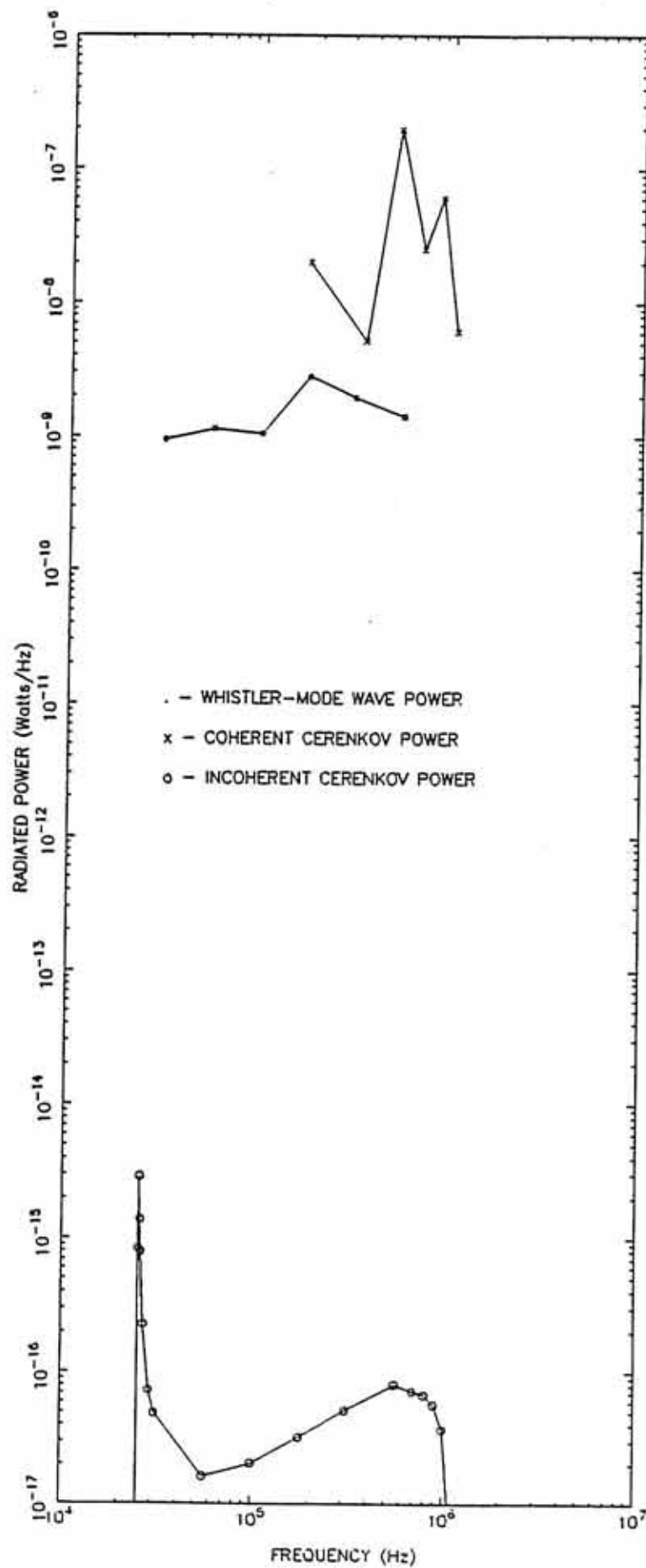
APPENDIX

A general formula for the radiated power from a field-aligned beam of current density $J_z(z)$ has been derived by C. K. Goertz. From this very general formalism, the radiated power from a single particle, N particles and a pulsed beam can be easily obtained.

First, the current density is written as

$$\overline{J}_q(\overline{r},t) = \hat{z} \langle nev \rangle_z \delta(x)\delta(y) = \hat{z} J_z(z,t) \delta(x)\delta(y) \qquad (A-1)$$

where $J_z(z)$ is the field-aligned component of the current density. The Fourier transform of the current can be written as

$$\overline{J}_q(\overline{k},\omega) = \frac{\hat{z}}{(2\pi)^4} \iint J_z(z,t) e^{i(k_z z - \omega t)} dzdt \qquad . \qquad (A-2)$$

In order to calculate the radiated power from a group of charges, a transformation must be made to a frame of reference moving with the charges. In this frame, the current density becomes independent of time:

$$J_z(z,t) = J_z(z') \qquad .$$

And, consequently, the current density appears stationary. The new coordinate z' is defined as $z' = z - V_s t$, where V_s represents the velocity of this moving frame. Expression (A-2) is then

$$\overline{J}_q(\overline{k},\omega) = \frac{\hat{z}}{(2\pi)^4} \int_{-\infty}^{\infty} J_z(z') \, e^{ik_z z'} \, dz' \int_{-\infty}^{\infty} e^{i(k_z V_s - \omega)t} dt \ . \qquad (A-3)$$

The quantity $\int_{-\infty}^{\infty} J_z(z') \, e^{ik_z z'} dz' = \sqrt{2\pi} \, J_z(k_z)$ where $J_z(k_z)$ is the Fourier transform of $J(z')$. Using the definition of the delta function, $\int_{-\infty}^{\infty} e^{i(k_z V_s - \omega)t} dt = 2\pi \, \delta(k_z V_s - \omega)$, and using the fact that $k_z = \frac{n\omega}{c}\cos\theta$, (A-3) now becomes

$$\overline{J}_q(\overline{k},\omega) = \frac{\hat{z}}{(2\pi)^3} \, (\sqrt{2\pi} \, J_z(k_z)) \, \delta(n\omega \cos\theta\beta - \omega) \qquad (A-4)$$

where $\beta = V_s/c$.

Using Equation (4-6), the electric field is written as

$$\overline{E}(\overline{r},t) = \frac{i}{(2\pi)^3 \epsilon_0} \iint (\overset{\leftrightarrow}{T}{}^{-1} \cdot \hat{z}) \, (\sqrt{2\pi} \, J_z(k_z))$$

$$(A-5)$$

$$\delta(n\omega\cos\theta\beta - \omega) e^{i(\omega t - \overline{k}\cdot\overline{r})} d\overline{k} \, \frac{d\omega}{\omega}$$

Knowing the electric field and source current, an expression for the radiated power can be obtained:

$$P(t) = \int E(\underline{r},t) \cdot \underline{I}(\underline{r},t) \, d\underline{r}$$

$$= \frac{i}{(2\pi)^3 \varepsilon_o} \iiint (\hat{z} \cdot \ddot{\bar{T}}^{-1} \cdot \hat{z})(\sqrt{2\pi} \, J_z(k_z)) \tag{A-6}$$

$$\delta(n\omega\cos\theta\,\beta - \omega) \, e^{i(\omega t - k_z z)} J_z(z,t) dz \, d\bar{k} \, \frac{d\omega}{\omega}$$

where the current is again described by (A-1). Moving to the frame $z'' = z - V_s t$, (A-6) can be rewritten as

$$P(t) = \frac{i}{(2\pi)^3 \varepsilon_o} \iiint (\hat{z} \cdot \ddot{\bar{T}}^{-1} \cdot \hat{z})(\sqrt{2\pi} \, J_z(k_z))$$

$$\delta(n\omega\cos\theta\,\beta - \omega) \, e^{i(\omega - n\omega\cos\theta\,\beta)t} \tag{A-7}$$

$$[J_z(z'') \, e^{-ik_z z''} dz''] \, d\bar{k} \, \frac{d\omega}{\omega} \quad .$$

The quantity in brackets is equal to $\sqrt{2\pi} \, J_z*(k_z)$ where $J_z*(k_z)$ is the conjugate Fourier transform of $J(z'')$. The element $d\bar{k}$ is

$$d\bar{k} = n^2 \frac{\omega^3}{c^3} \, dn \, \sin\theta \, d\theta \, d\phi \qquad \text{and}$$

$$k_z = \frac{n\cos\theta\,\omega}{c} = k_z(n,\theta) \quad .$$

Substituting these into (A-7) and integrating over ϕ yields:

$$P(t) = \frac{i}{(2\pi)^2 \epsilon_o} \iint (\hat{z} \cdot \bar{\bar{T}}^{-1} \cdot \hat{z})\, (2\pi) J_z(k_z(n,\theta))$$

$$J_z{}^*(k_z(n,\theta))\, \delta(n\omega \cos\theta\, \beta - \omega) \tag{A-8}$$

$$e^{i(\omega - n\,\omega\,\cos\theta\,\beta)t} n^2 \omega^2 dn\, \sin\theta\, d\theta\, d\omega \quad .$$

Integrating over θ, an integral of the form

$$I = \int f(x)\, \delta(Ax - B)dx = \frac{f(x_o)}{A}$$

must be solved where $A = |n\,\omega\,\beta|$, $B = \omega$ and $x_o = \cos\theta_o = \frac{1}{n\beta}$. The radiated power then becomes

$$P(t) = \frac{-i}{(2\pi)^2 \epsilon_o c^3 \beta} \iint (\hat{z} \cdot \bar{\bar{T}}^{-1} \cdot \hat{z})\, (2\pi) J_z(k_z(n,\theta_o))$$

$$\tag{A-9}$$

$$J_z{}^*(k_z(n,\theta_o))\, |n|\, |\omega|\, dn\, d\omega \quad .$$

An explicit form for $(\hat{z} \cdot \bar{\bar{T}}^{-1} \cdot \hat{z})$ is obtained using Equation (4-34), and upon obtaining the imaginary part to the integral

$$\int_o^\infty \frac{T_{33}(n)\, |n|\, f(n)\, dn}{(n^2 - n_1^2)(n^2 - n_2^2)} = \frac{\pi i}{2(n_2^2 - n_1^2)} \sum_{k=1}^{2} (-1)^k T_{33}(n_k)\, f(n_k)$$

where $f(n)$ is an arbitrary even with no singularities, the radiated power becomes

$$P(t) = \overline{P} = \int_{-\infty}^{\infty} \left(\frac{\omega \, d\omega}{8\pi \, \epsilon_o \epsilon_1 c^2 V_s}\right) \frac{1}{(n_2^2 - n_1^2)} \sum_{k=1}^{2} T_{33}(n_k)$$

$$\times \, [2\pi \, J_z(k_z(n_k,\theta_o)) J_z^*(k_z(n_k,\theta_o))] \quad .$$

(A-10)

Note that the radiated power is proportional to the square of the Fourier transform of the current density. Once the current density and its transform are known, it can be used in Equation (A-10) to easily calculate the radiated power.

As an example, the radiated power from a single field-aligned point charge moving at velocity, V_o, can be calculated. Moving to a frame where the particle is considered stationary, $V_s = V_o$, the current density becomes

$$J_z(z) = q \, V_o \delta(z - z_o),$$

where z_o represents the position of the particle relative to the center of coordinates for the frame moving at V_s. The current density transform becomes

$$J_z(k_z) = \frac{q \, V_o}{\sqrt{2\pi}} \int_{-\infty}^{\infty} \delta(z - z_o) e^{ik_z z} dz = q \, V_o \frac{e^{i \frac{n\omega}{c} \cos\theta \, z_o}}{\sqrt{2\pi}}$$

where $k_z = \frac{n\omega}{c} \cos \theta$. Using Equation (A-4), $\underline{J}_q(\underline{k}, \omega)$ is

$$\overline{J}_q(\overline{k}, \omega) = \hat{z} \frac{q V_o}{(2\pi)^3} e^{i \frac{n\omega}{c} \cos \theta z_o} \delta(n\omega \cos \theta \beta - \omega)$$

and is identical to (4-13). Since $J_z(k_z) J_z*(k_z) = 1/2\pi$, the radiated power is

$$P = \int_{-\infty}^{\infty} \left(\frac{q^2 \omega d\omega}{8\pi\epsilon_o\epsilon_1}\right) \left(\frac{V_o}{c^2}\right) \frac{1}{(n_2^2 - n_1^2)} \sum_{k=1}^{2} T_{33}(n_k)$$

which is identical to (4-22).

The power radiated from N point charges all moving at velocity V_o, but located at arbitrary positions along a field line can also be calculated. Again, $V_s = V_o$, however, the current density is now

$$J_z(z) = q V_o \sum_{i=1}^{N} \delta(z - z_i) \qquad ,$$

where z_i is the particle position relative to the center of coordinates of the frame moving with V_s. The transform becomes

$$J_z(k_z) = \sum_{i=1}^{N} \frac{q V_o}{\sqrt{2\pi}} \int_{-\infty}^{\infty} \delta(z - z_i) e^{ik_z z} dz$$

$$= \frac{q \, V_o}{\sqrt{2\pi}} \sum_{i=1}^{N} e^{ik_z z_i} = \frac{q \, V_o}{\sqrt{2\pi}} \sum_{i=1}^{N} e^{i \frac{n \, \omega}{c} \cos \theta \, z_i}$$

and

$$J_z{}^*(k_z) = \frac{q \, V_o}{\sqrt{2\pi}} \sum_{j=1}^{N} \frac{e^{-i \frac{n \, \omega}{c} \cos \theta \, z_j}}{\sqrt{2\pi}} \quad .$$

The quantity

$$J_z(k_z) \, J_z{}^*(k_z) = \frac{q \, V_o}{2\pi} \sum_{i=1}^{N} \sum_{j=1}^{N} e^{i \frac{n \, \omega}{c} \cos \theta (z_i - z_j)} \quad .$$

Inserting this into Equation (A-10) yields a result identical to that of (4-37) for $\beta_i = \beta_j$ ($V_{io} = V_{jo}$).

A surprising result is obtained for the radiated power if the beam density is completely uniform. In this case, the particles are moving at velocity, V_o; thus, $V_s = V_o$. The current density is

$$J_z(z) = q \, V_o \frac{N}{L} = q \, V_o \lambda_o \quad .$$

The transform is then

$$J_z(k_z) = q \, V_o \lambda_o \int_{-\infty}^{\infty} e^{ik_z z} \, dz = q \, V_o \lambda_o \delta(k_z) = q \, V_o \lambda_o \delta(\frac{n \, \omega}{c} \cos \theta)$$

and $J_z{}^*(k_z) = q\ V_o\lambda_o\delta(\frac{n}{c}\frac{\omega}{}$ cos $\theta)$. After substituting these into (A-10), it is found that radiation only at $\omega = 0$ is possible and consequently the radiated power is zero. Therefore, an unperturbed, uniform beam moving at velocity V_0 along a magnetic field will not radiate.

Finally, the power from a pulsed electron beam is considered. Using Equations (74), (76), (77) and (78) from Harker and Banks [1983], the Fourier transform of the field-aligned current is

$$\overline{J}(\overline{k},\omega) = \frac{q\ V_o\hat{z}}{(2\pi)^3}\ \delta(k_z V_o - \omega)\ N\ell\ \text{sinc}\ (\frac{k_z\ell}{2\pi})\ \sum_{m=-\infty}^{\infty}e^{imk_zd}$$

where ℓ is the pulse length and d is the distance between pulses. Comparing this with Equation (A-4), $J_z(k_z)$ is obtained:

$$J_z(k_z) = q\ V_o\ \frac{N\ \ell}{\sqrt{2\pi}}\ \text{sinc}(\frac{k_z\ell}{2\pi})\ \sum_{m=-\infty}^{\infty}e^{-imk_zd}$$

and $J_z{}^*(k_z)$ is

$$J_z{}^*(k_z) = q\ V_o\ \frac{N\ \ell}{\sqrt{2\pi}}\ \text{sinc}(\frac{k_z\ell}{2\pi})\ \sum_{m=-\infty}^{\infty}e^{imk_zd}\quad.$$

The quantity

$$J_z(k_z) \, J_z^*(k_z) = q^2 \, V_o^2 \, \frac{N^2 \ell^2}{2\pi} \, \text{sinc}^2(\frac{k\ell}{2\pi}) \, \left| \sum_{m=1}^{p} e^{-imk_z d} \right|^2$$

where p is the number of pulses. Since

$$\left| \sum_{m=1}^{p} e^{-imk_z d} \right|^2 = \frac{\sin^2(pdk_z/2)}{\sin^2(dk_z/2)} \quad ,$$

$J_z(k_z) \, J_z^*(k_z)$ is

$$J_z(k_z) \, J_z^*(k_z) = \left[q \, V_o \, \frac{N \ell}{\sqrt{2\pi}} \, \text{sinc} \, (\frac{k_z \ell}{2\pi}) \, \frac{\sin(pdk_z/2)}{\sin(dk_z/2)} \right]^2 \quad .$$

Inserting this into (A-10) yields an expression for the radiated power similar to Equation (91) of Harker and Banks.

REFERENCES

Banks, P. M., R. I. Bush, W. J. Raitt, Observations of electron beam structure on STS-3 and Spacelab 2 (abstract), EOS Trans. AGU, 66, 1053, 1985.

Beghin, C., J. P. Lebreton, B. N. Maehlum, J. Troim, P. Ingsoy, J. L. Michau, Phenomena induced by charged particle beams, Science, 225, 188-191, 1984.

Bell, T. F., Artificial production of VLF hiss, J. Geophys. Res., 73, 4409-4415, 1968.

Bernstein, W., H. Leinbach, P. J. Kellogg, S. J. Monson, and T. Hallinan, Further laboratory measurements of the beam plasma discharge, J. Geophys. Res., 84, 7271-7277, 1979.

Bush, R. I., T. Neubert, P. M. Banks, W. J. Raitt, D. A. Gurnett, Observations of enhanced plasma wave production during pulsed beam emissions (abstract), EOS Trans. AGU, 67, 1176, 1986.

Cartwright, D. G., and P. J. Kellogg, Observations of radiation from an electron beam artificially injected into the ionosphere, J. Geophys. Res., 79, 1439, 1974.

Dechambre, M., G. A. Gusev, Yu. V. Kushnerevsky, J. Lavergnat, R. Pellat, S. A. Pulinets, V. V. Selegei, I. A. Zhulin, High-frequency waves during the ARAKS experiments, Ann. Geophys., 36, 333-340, 1980a.

Dechambre, M., Yu. V. Kushnerevsky, J. Lavergnat, R. Pellat, S. A. Pulinets, and V. V. Seleger, Waves observed by the ARAKS experiment: The whistler mode, Ann. Geophys., 36, 351-359, 1980b.

Grandal, B. (ed.) Artificial Particle Beams in Space Plasma Studies, Plenum, New York, 1982.

Gurnett, D. A., A satellite study of VLF hiss, J. Geophys. Res., 71, 5599, 1966.

Gurnett, D. A., Electromagnetic plasma wave emissions from the auroral field lines, J. Geomag. Geoelectr., 30, 257-272, 1978.

Gurnett, D. A., and L. A. Frank, VLF hiss and related plasma observations in the polar Magnetosphere, J. Geophys. Res., 77, 172, 1972.

Gurnett, D. A., W. S. Kurth, J. T. Steinberg, P. M. Banks, R. I. Bush, and W. J. Raitt, Whistler-mode radiation from the Spacelab-2 electron beam, Geophys. Res. Lett., 13, 225-228, 1986.

Gurnett, D. A., S. D. Shawhan, and R. R. Shaw, Auroral hiss, Z-mode radiation, and auroral kilometric radiation in the polar magneto-sphere: DE-1 observations, J. Geophys. Res., 88, 329-340, 1983.

Harker, K. J. and P. M. Banks, Radiation from pulsed electron beams in space plasmas, Radio Sci., 19, 454-470, 1983.

Hartz, T. R., Radio Noise Levels Within and Above the Ionosphere, Proc. ISEE, 57, 1042, 1969.

Hess, W. N., M. G. Trichel, T. N. Davis, W. C. Beggs, G. E. Kraft, E. Stassinopoulos, and E. J. R. Maier, Artificial auroral experiment: Experiment and principal results, J. Geophys. Res., 76, 6067, 1971.

Inan, U. S., M. Pon, P. M. Banks, P. R. Williamson, W. J. Raitt, and S. D. Shawhan, Modulated beam injection from the space shuttle during magnetic conjunction of STS-3 with the DE-1 satellite, Radio Science, 19, 487, 1984.

James, H. G., VLF observations of auroral beams as sources of a class of emissions, Nature, 224, 351, 1969.

Jones, T. W., and P. J. Kellogg, Plasma waves artificially induced in the ionosphere, J. Geophys. Res., 75, 2166, 1973.

Jorgensen, T. S., Interpretation of auroral hiss measured on OGO-2 and at Byrd Station in terms of incoherent Cerenkov radiation, J. Geophys. Res., 73, 1055, 1968.

Katz, I., G. A. Jongeward, D. E. Parks, D. L. Reasoner, and C. K. Purvis, Energy broadening due to space-charge oscillations in high current electron beams, Geophys. Res. Lett., 13, 64-67, 1986.

Kellogg, P. J., D. G. Cartwright, R. A. Hendrickson, S. J. Monson, and J. R. Winckler, The University of Minnesota electron Echo experiment, Space Res., XVI, 589-599, 1976.

Kellogg, P. J., S. J. Monson, W. Bernstein, and B. A. Whalen, Observations of waves generated by electron beams in the ionosphere, J. Geophys. Res., 91, 12065-12078, 1986.

Laaspere, T., and R. A. Hoffman, New results on the correlation between low-energy electrons and auroral hiss, J. Geophys. Res., 81, 524, 1976.

Lavergnat, J., M. Dechambre, R. Pellat, Yu. V. Kushnerevsky, S. A. Pulinets, Waves observed by the ARAKS experiments: Generalities, Ann. Geophys., 36, 323-332, 1980.

Liemohn, H. B., Radiation from electrons in a magnetoplasma, Radio Sci., 690, 741, 1965.

Lin, C. S., J. L. Burch, S. D. Shawhan, and D. A. Gurnett, Correlation of auroral hiss and upward electron beams near the polar cusp, J. Geophys. Res., 89, 925, 1984.

Maggs, J. E., Coherent generation of VLF hiss, J. Geophys. Res., 81, 1707-1724, 1976.

Mansfield, V. N., Radiation from a charged particle spiraling in a cold magnetoplasma, Astrophy. J., 147, 672, 1967.

Monson, S. J., P. J. Kellogg, and D. G. Cartwright, Whistler-mode plasma waves observed on electron Echo II, J. Geophys. Res., 81, 2193, 1987.

Mosier, S. R., and D. A. Gurnett, VLF measurements of the Poynting flux along the geomagnetic field with Injun 5 satellite, J. Geophys. Res., 74, 5675-5687, 1969.

Mosier, S. R., and D. A. Gurnett, Theory of the Injun 5 very-low-frequency Poynting flux measurements, J. Geophys. Res., 76, 972-977, 1971.

Neubert, T., W. W. L. Taylor, L. R. O. Storey, N. Kawashima, W. T. Roberts, D. L. Reasoner, P. M. Banks, D. A. Gurnett, R. L. Williams, and J. L. Burch, Waves generated during electron beam emissions from the space shuttle, J. Geophys. Res., 91, 11321-11330, 1986.

Pritchett, P. L., and R. M. Winglee, The plasma environment during particle beam injection into space plasmas, 1. Electron Beams, J. Geophys. Res., submitted.

Reeves, G. D., P. M. Banks, R. I. Bush, K. J. Harker, An analysis of the harmonic structure of VLF radiation generated by a square wave modulated electron beam in space (abstract), EOS Trans. AGU, 67, 1176, 1986.

Shawhan, S. D., Description of the Plasma Diagnostics Package (PDP) for the OSS-1 shuttle mission and JSC chamber test in conjunction with the Fast Pulsed Electron Gun (FPEG), Artificial Particle Beams in Space Plasma Studies, ed. by B. Grandel, Plenum, NY, pp. 419-430, 1982.

Shawhan, S. D., G. B. Murphy, P. M. Banks, P. R. Williamson, and W. J. Raitt, Wave emissions from D. C. and modulated electron beams on STS-3, Radio Science, 19, No. 2, 471-486, 1984.

Smith, R. L., VLF observations of auroral beams as sources of a class of emissions, Nature, 224, 351, 1969.

Stix, T. H., The Theory of Plasma Waves, McGraw-Hill, New York, 1962.

Taylor, W. W. L., and S. D. Shawhan, A test of incoherent Cerenkov radiation for VLF hiss and other magnetospheric emissions, J. Geophys. Res., 79, 105-117, 1974.

Wilhelm, K., W. Bernstein, B. A. Whalen, Study of electric fields parallel to magnetic lines of force using artificially injected energetic electrons, Geophys. Res. Lett., 7, 117, 1980.

Williamson, P. R., J. G. Hawkins, R. I. Bush, P. M. Banks, W. J. Raitt, Vehicle charging measured during electron beam emission on Spacelab-2 (abstract), EOS Trans. AGU, 66, 1051, 1985.

Winglee, R. M., and P. L. Pritchett, Space-charge effects during the injection of dense electron beams into space plasmas, J. Geophys. Res., submitted.

Winkler, J. R., The application of artificial electron beams to magnetospheric research, Rev. Geophys. Res. and Space Phys., 18, No. 3, 659-682, 1980.

Winkler, J. R., K. N. Erickson, P. R. Malcolm, A new experiment to investigate the conjugate echoes and plasma physics phenomena produced by an electron beam injected in the ionosphere--Echo 7 (abstract), EOS Trans. AGU, 67, 1180, 1986.